

1626
SANDIA REPORT

SAND86-0177 • UC-70

Unlimited Release

Printed April 1987

SCP
5-1765

Nevada Nuclear Waste Storage Investigations Project

Rock Joint Compliance Studies

William A. Olsson

Prepared by
Sandia National Laboratories
Albuquerque, New Mexico 87185 and Livermore, California 94550
for the United States Department of Energy
under Contract DE-AC04-76DP00789

"Prepared by Nevada Nuclear Waste Storage Investigations (NNWSI) Project participants as part of the Civilian Radioactive Waste Management Program (CRWM). The NNWSI Project is managed by the Waste Management Project Office (WMPO) of the U. S. Department of Energy, Nevada Operations Office (DOE/NV). NNWSI Project work is sponsored by the Office of Geologic Repositories (OGR) of the DOE Office of Civilian Radioactive Waste Management (OCRWM)."

Issued by Sandia National Laboratories, operated for the United States Department of Energy by Sandia Corporation.

NOTICE: This report was prepared as an account of work sponsored by an agency of the United States Government. Neither the United States Government nor any agency thereof, nor any of their employees, nor any of their contractors, subcontractors, or their employees, makes any warranty, express or implied, or assumes any legal liability or responsibility for the accuracy, completeness, or usefulness of any information, apparatus, product, or process disclosed, or represents that its use would not infringe privately owned rights. Reference herein to any specific commercial product, process, or service by trade name, trademark, manufacturer, or otherwise, does not necessarily constitute or imply its endorsement, recommendation, or favoring by the United States Government, any agency thereof or any of their contractors or subcontractors. The views and opinions expressed herein do not necessarily state or reflect those of the United States Government, any agency thereof or any of their contractors or subcontractors.

Printed in the United States of America
Available from
National Technical Information Service
U.S. Department of Commerce
5285 Port Royal Road
Springfield, VA 22161

NTIS price codes
Printed copy: A06
Microfiche copy: A01

SAND86-0177
Unlimited Release
Printed 1987

ROCK JOINT COMPLIANCE STUDIES*

William A. Olsson

*Geomechanics Division
Sandia National Laboratories
Albuquerque, New Mexico 87185*

ABSTRACT

This report has three objectives: (1) to summarize the developmental investigations of the rotary shear test for use in rock joint compliance studies, including a description of the rotary shear machine and sample preparation techniques, (2) to set out and discuss the required constitutive data, showing how to interpret and analyze the shear compliance data from this type of test, and (3) to give some examples and preliminary data for Topopah Spring tuff. The report contains some expository material for the benefit of nonspecialists not familiar with the broad scope of friction problems. Additionally, new unpublished results are included on the effects of nonuniform slip, normal stress history, and velocity of sliding for Topopah Spring tuff.

*This work performed at Sandia National Laboratories supported by the U.S. Department of Energy under contract number DE-AC04-76DP00789.

Contents

1	INTRODUCTION	5
1.1	Background	5
1.2	The Required Constitutive Data	7
1.2.1	Displacement Decomposition	8
1.2.2	Preslip Response	9
1.2.3	Slip Condition	10
1.2.4	Time-Dependent Response	11
1.3	Summary of the Constitutive Parameters	14
2	APPARATUS AND PROCEDURES	17
2.1	Rotary Shear Machine	17
2.1.1	Configuration and Capacities	17
2.1.2	Variables Recorded	17
2.2	Sample Preparation	18
2.2.1	Shear Compliance	18
2.2.2	Normal Stiffness	18
2.3	Test Procedures	19
2.3.1	Shear Compliance	19
2.3.2	Normal Stiffness	20

3	EXPERIMENTS AND DATA REDUCTION	23
3.1	Displacement Measurement	23
3.2	Stresses on the Interface in Rotary Shear	23
3.2.1	Preslip Shear Stress Profile	23
3.2.2	Fully Sliding Shear Stress Profile	24
3.2.3	Shear Stress Profile During Partial Slip	25
3.3	Comparison of an Experiment with the Theory	25
3.4	Shear Compliance of Smooth Surfaces	26
3.4.1	Evolution of Shear Strength During Steady Sliding	26
3.4.2	Strength Increases during Stationary Contact	26
3.4.3	Effects of Sliding Velocity History	27
3.4.4	Effects of Normal Stress History	28
3.4.5	Slip Condition	35
3.5	Shear Compliance of Rough Surfaces	37
3.5.1	Dilatancy	37
3.6	Normal Stiffness	38
3.6.1	Experimental Observations	38
4	CONCLUSIONS	39
4.1	Outlook	40
	REFERENCES	42
A	Theoretical Model	47
A.1	<i>Torque-Stress Relations</i>	47
A.2	<i>Torque-Slip Relations</i>	48

<i>A.3 Model Response</i>	51
<i>A.4 Returning the Interface to Uniformly Zero Shear Stress</i>	53
<i>A.5 The Shear Stress in the Slip Plane During Slip Establishment</i>	53
B FIGURES	55
C Sample Key	91
D Data Status	93

Chapter 1

INTRODUCTION

1.1 Background

Capabilities for the prediction of the response of rock masses to thermo-mechanical loadings are being developed under the Nevada Nuclear Waste Storage Investigations (NNWSI) Project with application to the design of an underground nuclear waste repository at Yucca Mountain on the Nevada Test Site. An important ingredient in the computer codes being used is the constitutive description of the mechanical discontinuities (mostly joints but also bedding planes and faults). This report summarizes the application of the rotary shear test to the determination of the necessary constitutive parameters for rock joints. First, some background and motivation for using the rotary shear apparatus is given. Then, in the following section, the type of constitutive functions that are required are exhibited. In the section on test procedures, the experimental methods for obtaining the specified functions are discussed. Finally, examples of each type of test are described. Reports detailing the complete data base will be issued presently.

The rotary shear apparatus being used in this work is but one type of machine that is useful in friction studies. In more common use are the triaxial compression and the direct shear machines. Each of the three has certain special capabilities and deficiencies. The triaxial test (Fig. 1a) has the capability of applying high normal stress across a test fracture because of the increased rock strength due to the confining pressure. However, the NNWSI project is not in need of high pressure data, so this capability is unnecessary. On the negative side, there are severe constraints on the amount of slip that can be attained in triaxial compression, and, in fact, any slip at all causes unknown changes in the normal stress distribution and magnitude across the fracture surface. The limitation on the amount of slip to be expected in triaxial

testing can be partially overcome by a type of incremental loading [Olsson, 1974], but loading history effects must then be neglected. Additionally, the shear and normal stresses are coupled in the standard constant confining pressure test so that the normal stress varies linearly with differential stress. Thus, precise reduction of data is difficult, and any effects of normal stress history [Olsson, 1984c] are obscured. Perhaps more important is the effect of stress path on frictional slip predicted by Olsson [1984b]. In that work, the shapes of the stress-slip curves from constant normal stress testing are compared to those from constant confining pressure testing, and significant, systematic differences are found.

Direct shear machines (Fig. 1b,c) have the advantage of being able to accommodate relatively large samples. Disadvantages, however, are that because of induced turning moments, it is difficult to maintain a uniform normal stress, and the surface area of contact is characterized by continuous injection of new surface or a changing contact area.

The rotary shear test (Fig. 1d) is effected by forcing the ends of two short, right-circular cylinders (shaped like washers or tubes) together and then twisting them to establish rotationally symmetric, frictional sliding about their common axis. Applications of the data obtained from such a test encompass such diverse subjects as the slippage on microcracks in intact rock and on faults bounding the earth's crustal plates. The geometry of initial deformation is anti-plane strain, but symmetry arguments can be used to apply many of the results to plane strain problems, as well. Moreover, for thin-walled samples, large slip deformations are essentially plane strain. A wide range of deformation geometries is thus accessible. Advantages of the rotary shear machine are that (1) the normal and shear stresses are completely decoupled for all amounts of slip, (2) sample size can be relatively large, (3) the area of sliding interface remains constant so that arbitrarily large displacements can be achieved, (4) shear and normal stress and displacement can be independently controlled, and (5) the normal stress is uniform. Thus, as a test configuration for the determination of constitutive functions uncomplicated by uncontrolled input variables, the rotary shear test is unsurpassed.

The rotary shear configuration is not free from some shortcomings either, however. In the absence of a confining pressure vessel, the test is limited to low normal stress compared to the triaxial machine, but as noted above, for our purposes, this is not important. Also, there is a gradient in the shear stress acting on the sliding surface, which can be considered an advantage provided that the mechanics of slip in this configuration are properly understood [Olsson, 1986]. The shear stress gradient is an advantage to the extent that fundamental questions concerning such topics as the propagation of a slip zone in a well-known, uniform stress gradient, and superposition of slip zones of differing senses and dimensions can, under certain conditions, be addressed in rotary shear. Because nonuniform stress is the rule rather than the exception near any un-

derground opening, this idea may become more important as analyses become more complete. Exemplifying engineering occurrences of stress gradients, one may consider slip zones nucleated in nonuniform stress fields caused by the mining of underground openings in jointed rock masses and the drilling of boreholes. Moreover, interaction of slip zones and repeated or reversed loading may take place during various construction phases of underground structures. The rotary shear configuration allows study of both the simplest type of nonuniform stress and the interaction of slip zones; therefore, this test can provide important insights into these problems.

The analytical work described in the appendix is critical to the development of this test technique and has proven useful both in interpreting the experimental data and in suggesting new loading sequences. Some earlier work in rotary shear has been done on thick-walled cylinders sheared to large displacements [Kutter, 1974; Christensen *et al.*, 1974] in connection with surface property measurement. But the details of the mechanics of rotary shear were only partly understood.

The rotary shear problem resembles classical elastic-plastic torsion [Prager and Hodge, 1951] in the sense that inelastic deformation progresses from the outside of the cylinder inward during increasing twist. During elastic-plastic torsion of a circular bar, plane sections perpendicular to the axis of twist remain plane and initial radii remain straight. This geometry results in a tangential shear strain in the plane perpendicular to the axis of twist that is directly proportional to the twist and to the radius. Moreover, in this problem the twist-angle per unit length is a constant for small deformations. These facts allow the direct computation of the shear stress and the depth of the plastic zone [e.g., Smith and Sidebottom, 1969; Prager and Hodge, 1951]. Perpendicular cross sections in rotary shear, while they remain planar, distort in the plane so that radii do not remain straight. This is because the twist-angle per unit length experiences a jump when crossing the slipping interface. Thus, the rotary shear problem is more complex because the shear strain is not known *a priori*; it must be calculated as part of the solution.

1.2 The Required Constitutive Data

The type of data needed is now outlined by referring to a two-dimensional joint constitutive model similar to one described by Goodman and Dubois [1972]. Thomas [1982] used such a law in previous NNWSI-related work. Chen [1986] reports on an extension of Thomas' study. A recent discussion [Plesha, 1985] relates frictional constitutive laws to nonassociated plasticity.

1.2.1 Displacement Decomposition

Any joint constitutive model must relate applied stress to joint displacement. Because there seems to be some confusion, or at least lack of precision, in the description of displacements in the literature, we begin by defining the total deformation of a block of rock containing a single joint (Fig. 2). The upper and lower boundaries of the block are arbitrary reference surfaces drawn parallel to the joint. The fiducial line will allow definition of the various shear displacements; the normal displacements are obtained by replacing the subscript t with n . Define orthogonal coordinates t and n to be tangent and normal to the joint, respectively. Then, the stresses are denoted σ_i , and the displacements are denoted u_i , where $i = t$ or n . It is assumed that the total displacement u_i^t can be additively decomposed and written in incremental form as

$$du_i^t = d\bar{u}_i^j + d\tilde{u}_i^j + d\bar{u}_i^r + d\tilde{u}_i^r, \quad (1.1)$$

where total deformation comprises that due to the joint, u_i^j , and that due to the intact rock, u_i^r . Each of these components is further decomposed into a recoverable elastic part, distinguished by the overbar; and a nonrecoverable plastic part, distinguished by the tilde.

The physical origin of these various displacements is clear except, possibly, for \bar{u}_i^j . As suggested by Figure 2, there may exist a zone near the joint that has a lower effective modulus. It may be that this zone is the wake of the process zone that existed transiently during propagation of the joint. Another possibility is apparent if the joint is thought of as a sheet of penny-shaped cracks, or a sheet of essentially point contacts separated by open spaces. In this latter model, the joint represents a tabular zone of vanishing thickness with a reduced shear modulus. The main problem with this model is that the shear stress at the edges of regions of contact is, theoretically, infinitely high. Analyses [e.g., *Mindlin and Deresiewicz, 1953*] show that these high shear stresses are always relieved by slip. Thus, this is a plastic displacement rather than an elastic one and should manifest itself as a nonrecoverable contribution to the joint displacement.

Counting the total displacements, there are potentially 10 different displacement components to be dealt with in this very general measure of the displacement field that account for all physically reasonable processes to at least first order. The first simplification, which is borne out by testing and will be addressed in a later section, is the assumption of no plastic deformation of the rock blocks, $\tilde{u}_i^r = 0$, because of the low prevailing shear stresses. Moreover, it is shown later that experiments on smooth surfaces of granite and on both smooth and rough surfaces of tuff suggest that \bar{u}_i^j is small in comparison to \tilde{u}_i^j .

1.2.2 Preslip Response

The prototype for a perfectly plastic material is a rigid block sliding on a plane frictional surface, and therefore it is natural to adopt the viewpoint of plasticity theory when developing constitutive theory for rock joints. This requires an elastic preslip description, a slip function, and a flow rule. The elastic preslip behavior is usually assumed to be separable from the elastic rock behavior. The slip function defines the limit of elastic behavior in terms of the state of stress, and the flow rule relates slip rates to stress in the sliding regime. The usual approach is to assume that there is a preslip response that is described by

$$\sigma_k = K_{kl} \bar{u}_l^j \quad (k \text{ or } l = t \text{ or } n) \quad (1.2)$$

where σ_t is the shear stress, σ_n the normal stress, \bar{u}_t^j the elastic component of the shear displacement, \bar{u}_n^j the elastic component of the normal displacement, and the K_{kl} are the joint stiffnesses. Though little is known at present, the stiffnesses are probably influenced by variables such as stress history, temperature, water content, and others. Therefore, this law must be considered only a crude approximation to reality. This report deals mainly with the determination of K_{tt} and, secondarily, with K_{nn} since these are the functions that are most accessible and seem most critical. The coupled shear-normal stiffness, K_{nt} , is related to the dilatancy rate, which is measured as described below. Little importance has been attached to K_{tn} because on physical grounds it is probably small.

The literature on the experimental determination of K_{nn} and K_{tt} is somewhat inconsistent. Most treatments define normal stiffness, K_{nn} , concisely to be the difference in response of a sample with and without a joint [cf., *Goodman et al.*, 1968; *Rosso*, 1976; *Bandis et al.*, 1983; *Sun et al.*, 1985]. This method automatically removes all response of the surrounding solid rock, and also any machine deflections included within the gauge length. However, these same workers take the shear stiffness to be the ratio of the peak shear stress to the overall shear displacement at that stress. This is not consistent with the definition of normal stiffness. The curves often shown of shear stress plotted against shear displacement always use total displacement, i.e., u_t^j . No attempt seems to have been made to subtract out the elastic deflection of the intact rock and the machine, almost always a direct shear box apparatus. *Rosso* [1976] recognized that data from a shear box device gave K_{tt} that was a function of the gauge length; clearly, not a desirable result. A possible reason for this dichotomy is that for practical reasons it would be difficult to obtain the intact sample response from a direct shear machine of the box type. Based on data discussed below, it might be permissible to assume that the initial linear portion of the σ_t versus u_t^j curve was due only to elastic deformation of the intact rock and the machine. If this were true, it would be a simple matter to compute the consistent K_{tt} .

Differentiation of equation (1.2) gives the strict definition of the stiffnesses. The two most important of these are the shear stiffness,

$$K_{tt} = \left(\frac{\partial \sigma_t}{\partial \bar{u}_t} \right)_{u_n}$$

and the normal stiffness,

$$K_{nn} = \left(\frac{\partial \sigma_n}{\partial \bar{u}_n} \right)_{u_t}$$

The subscripts emphasize that the indicated variable is supposed to be held constant. *Goodman and Dubois* [1972] pointed out that most laboratory and field tests are not actually carried out in accordance with these definitions. That is, the shear response is most often determined at constant normal stress, σ_n , rather than constant normal displacement, u_n . The same is true for the usual determination of the normal stiffness at a putative constant shear displacement. However, in the latter measurement, since for most surfaces there is little tendency to slip when the normal stress is changed at zero shear stress, the shear displacement is constant and equal to zero. In the shear response test currently run we measure the compliance, that is,

$$C_{tt} = \left(\frac{\partial \bar{u}_t}{\partial \sigma_t} \right)_{\sigma_n}$$

where C_{tt} is the shear compliance. This point has received recent attention [*Sun et al.*, 1985]. Although the rotary shear apparatus is capable of running either fixed normal stress or fixed normal displacement, to date only fixed normal stress has been used; further testing at fixed normal displacement will be reported later.

1.2.3 Slip Condition

The boundary in stress-space that defines the limit of elastic response described by (1.2) is the slip condition and for two dimensions it is written

$$f(\sigma_i, \mathcal{H}) = 0. \quad (1.3)$$

This form of the slip condition includes a hardening (or softening) function, \mathcal{H} , which may be due to geometric effects of a wavy surface or to material evolution of surface properties. *Plesha* [1985] derived a specific form of \mathcal{H} that is a function of slip and plastic work, and describes realistic stress-displacement behavior. Experimental evaluation of a generalization of \mathcal{H} for rock masses where hardening is due to joint block lock-up is discussed in *Olsson* [1982b,c]. The simplest specialization of (1.3) is nonhardening, Coulomb friction so that the slip condition reduces to the familiar form

$$|\sigma_t| - \mu \sigma_n = 0, \quad (1.4)$$

where μ is the coefficient of sliding friction. When equality holds, unlimited slip may occur. As with the so-called stiffnesses, μ can also be a function of the several field and environmental variables. Once slip ensues, the relationship between stress and displacement can be obtained by integration of the plasticity flow rules [Michałowski and Mróz, 1978; Plesha, 1985].

During sliding, displacement normal to the joint is sometimes observed, especially on rougher surfaces, and is called dilatancy. Dilatancy is predicted, but excessively, by the classical, associated plasticity. In nonassociated theory, dilatancy is a variable subject to measurement. This is an important property because the permeability of a fracture increases with the cube of the aperture. If constant normal stress boundary conditions are maintained during sliding, the rate of change in aperture due to shear displacement is called the dilatancy rate, β , defined as

$$\beta = \left(\frac{\partial u_n^j}{\partial u_i^s} \right)_\sigma \quad (1.5)$$

Depending on initial conditions of the joint, u_n can be either an even or odd function of u_i . Furthermore, $\beta(0)$ can be positive or negative. This parameter is obviously closely related to original joint roughness and degree of interlocking. It shows clearly the importance of joint slip to changes in permeability for rough joints. One sample with significant roughness has been tested in shear, and the dilation data for that are discussed in 3.6.1.

1.2.4 Time-Dependent Response

Further complicating the matter, and not explicit in (1.3) or (1.4), is the fact that the friction stress in rock is known to depend on sliding rate [e.g., Dieterich, 1979]. Teufel [1981] showed that the well-established rate dependence found in silicate rocks such as granite extends to welded tuff, also, of course, a silicate rock. Moreover, our own tests, discussed below, show that frictional slip in the Topopah Spring tuff is also influenced by the sliding rate. More precisely, the friction stress depends on the history of the velocity with stronger dependence on the velocities in the recent past than those in the distant past [Dieterich, 1972, 1978, 1979, 1981; Ruina, 1983].

Another potentially important variable suggested by Rice and Ruina [1983] and included explicitly in a constitutive equation by Olsson [1984c] is the analogous hereditary effect of changes in normal stress. The principal question is whether there is a direct relation between shear and normal stress or is the shear stress dependent in some way on the history of the normal stress. Stated another way, does the current shear stress depend on how changes were made in normal stress or just on the current value?

Brief discussions of the experimental verification of the existence of this effect were first given by *Hobbs and Brady* [1985] and *Olsson* [1985]. A more extensive report can be found in *Olsson* [1987]. A one-dimensional constitutive model taking into account both the velocity history and normal stress history effects is [*Olsson*, 1984c]

$$\begin{aligned} \tau(t) - \tau_0 = & \mu_\sigma(0)V_d(t) - \int_{-\infty}^t \dot{\mu}_\sigma(t-t')V_d(t') dt' + \\ & \mu_V(0)\sigma_d(t) - \int_{-\infty}^t \dot{\mu}_V(t-t')\sigma_d(t') dt', \end{aligned} \quad (1.6)$$

where, for clarity, shear stress is now denoted τ and normal stress is σ . The current time is denoted t and past time is $-\infty < t' \leq t$. Here τ_0 is a steady reference shear stress equilibrated at the reference velocity V_0 and normal stress σ_0 . The *generalized coefficients of friction*, μ_σ and μ_V , are to be determined experimentally. The first line on the right representing the transient response to changes in velocity, $V_d = V(t) - V_0$, is composed of two parts: the instantaneous term at $t = 0$, and the time-dependent change given by the integral. The second line on the right gives the analogous response to a change in normal stress during steady sliding. The meaning of the terms in (1.6) at constant normal stress are shown in Figure 3. An analogous picture can be drawn for the remaining terms when the velocity is held constant and the normal stress is varied except that the sign of $\dot{\mu}_V$ appears to be opposite to that of $\dot{\mu}_\sigma$. (Compare the transients in Figs. 3 and 8 to those in Fig. 15.) The basic tests to determine μ_V and μ_σ are described below.

This model, unlike that given in (1.3), is capable of taking into account certain history effects that are completely outside the scope of the latter, such as past overpressuring or normal stress cycles combined with shear stress changes as would occur during excavation of an underground opening. Moreover, acoustic emissions associated with slip on joints in Grouse Canyon welded tuff [*Holcomb and Teufel*, 1982] can be instabilities in slip, which can be approached through a hereditary friction law such as (1.6).

The constitutive law embodied in (1.6) addresses normal stress change effects that can occur on smooth surfaces. Almost certainly, rougher surfaces will undergo irreversible asperity crushing and thus are as yet too complex to be described adequately by an equation such as (1.6). This is because this type of law was developed for surfaces that have no fundamental dependence on slip, only short-term, fading dependence.

The hereditary integral in (1.6) is a linearization of a very general functional constitutive relation for slip [*Olsson*, 1984c]. For certain forms of the kernels, this type of integral equation is equivalent to an algebraic equation relating the shear stress to a function called the internal state variable and a first-order differential equation for the state variable [e.g., *Nunziato et al.*, 1974].

Ruina [1983] introduced the idea of internal state variables to rock friction work based on extensive experimentation of *Dieterich* [see refs.] This approach assumes that the surface is characterized by its state at each value of slip. The time rate-of-change of the state is an evolution law for the interface. *Ruina's* formulation (simplified versions of equations constructed by *Dieterich*) is nonlinear and, evidently [*Rice and Ruina, 1983*], hereditary integrals like those in (1.6) can also be considered linearizations of state variable relations developed by *Ruina* [1983]. The connection between the hereditary integral and the linear state variable approaches is shown below. Then the connection to *Ruina's* nonlinear state variable constitutive equations is explained.

Let σ remain steady ($\sigma_d = 0$) for all time; this causes the second line of (1.6) to vanish. Following *Nunziato et al.* [1974], take $A - B(1 - e^{-t/t_r})$ as the simplest function, μ_σ , that is finite at $t = 0$ and decays to some asymptotic value for long times, where t_r is a characteristic relaxation time and A and B are constants. This gives

$$\begin{aligned}\mu_\sigma(0) &= A \\ \mu_\sigma(\infty) &= A - B\end{aligned}\quad (1.7)$$

and

$$\dot{\mu}_\sigma(t) = -\frac{B}{t_r} e^{-t/t_r}.\quad (1.8)$$

Then define the state variable, θ , by

$$\theta(t) = \int_0^\infty \frac{B}{t_r} e^{-t'/t_r} V_d(t-t') dt'.\quad (1.9)$$

Now the time-dependent shear strength following a step change in velocity can be written

$$\tau(t) = \tau_0 + A V_d - \theta(t).\quad (1.10)$$

$A V_d$ is the magnitude of the shear stress jump corresponding to the velocity jump, V_d , and the gradual stress decay is given by the evolving state variable, θ . Time differentiation of θ to obtain the evolution law gives [cf. *Ruina, 1983*]

$$\dot{\theta} = \frac{1}{t_r} [\theta(t) - B V_d].\quad (1.11)$$

For $t \rightarrow \infty$, $\theta = B V_d$ and the shear stress evolves to a steady-state value given by

$$\tau_{ss} = \tau_0 + (A - B) V_d.\quad (1.12)$$

This is seen to be the same form as that given for $\dot{\theta}$ in *Gu et al.* [1984] for the nonlinear theory. It is normally found in experiments [*Dieterich, 1979*] that the steady shear stress is related in a simple way to $\ln V/V_0$. Thus, in the nonlinear theory, the rate

effects are linear in $\ln V/V_0$. For $V \rightarrow V_0$, $\ln V/V_0 \rightarrow V_d$ and the connection between the linear version and the nonlinear is established, in the limit of small V_d .

The nonlinear theory is better suited to the description of the experiments to be discussed below because they involve velocity jumps of $V/V_0 = 10$; thus, equations (1.10), (1.11), and (1.12) become [cf. *Gu et al.*, 1984]

$$\tau(t) = \tau_0 + A \ln(V/V_0) - \theta(t) \quad (1.13)$$

and

$$\dot{\theta} = (V/L)[\theta - B \ln(V/V_0)], \quad (1.14)$$

with τ evolving to

$$\tau_{ss} = \tau_0 + (A - B) \ln(V/V_0). \quad (1.15)$$

Here $1/t_r$ has been replaced by the dimensionally equivalent V/L . A physical model based on asperity contact dynamics suggesting this equivalence was proposed by *Dieterich* [1978]. Ideally, θ should be related to the physics of the sliding process; however, in the absence of the necessary data, the state variable is taken as just a phenomenologically determined function. An analogous measure of property evolution in the rate-independent plasticity theory of *Plesha* [1985] is the hardening function, \mathcal{H} , of (1.3).

1.3 Summary of the Constitutive Parameters

- *Stiffnesses.* The most critical stiffnesses are K_{tt} and K_{nn} . These should be measured, ideally, at $du_n = 0$ and $du_t = 0$, respectively. The second condition is met in the normal test procedure. However, the first condition has been temporarily replaced by $d\sigma_n = 0$. Later testing will be done in accordance with the first condition. Data for smooth ground, surfaces, and laboratory-induced tensile fractures are required to bound natural roughnesses. Environmental conditions have been air dry and room temperature; later testing will include wet specimens.
- *Generalized coefficients of friction.* The generalized coefficients of friction, μ_V and μ_σ , are being determined on smooth, air-dry surfaces by means of Heaviside input histories. The effects of the presence of water will be investigated later.
- *Slip condition.* The slip condition is being determined for air-dry, smooth, and laboratory-induced tensile fracture surfaces. Different stress paths are being used to probe the slip condition.
- *Dilatancy.* The dilatancy is being determined for laboratory-induced tensile fractures because the ground surfaces show no measurable dilatancy.

All of the above constitutive parameters come from the same basic test type. In this test, a normal stress is first applied to the joint, then the torque is increased until uniform sliding occurs. The generalized coefficients of friction are measured by suddenly changing velocity or normal stress during uniform sliding. The stiffnesses and the dilatancy are determined by deformation-measuring instrumentation at appropriate stages of the test. The details are given in a later section.

Chapter 2

APPARATUS AND PROCEDURES

2.1 Rotary Shear Machine

2.1.1 Configuration and Capacities

The rotary shear machine consists of a load frame containing a hydraulic rotary actuator in series with a hydraulic linear actuator. The maximum torque capability is 7000 N·m and the maximum axial force is 900 KN. These actuators are independently servocontrolled by 410 function generators and 442 controllers from *MTS Systems, Inc.* Angle of rotation, axial load, and torque are calibrated yearly by *MTS Systems, Inc.*

2.1.2 Variables Recorded

In each test, the far-field twist angle, torque, and axial force are recorded by the data acquisition computer and stored on a floppy disk using software described in *Holcomb and Jones [1983]*. Occasionally, slip is directly measured by a modified clip-on extensometer. The data are transferred immediately to the Department 1530 *VAX 11/780 (Digital Equipment Corporation)* computer where they are stored indefinitely for analysis and plotting.

2.2 Sample Preparation

Westerly granite and Topopah Spring tuff were used for development of the test techniques described below. The one granite sample referred to in this report was cored from a block already available in the rock mechanics laboratory. The densely welded Topopah Spring tuff was collected from outcrop at Busted Butte, near Yucca Mountain on the Nevada Test Site. Details of specimen preparation can be found in Schwartz [1984]. Because several experiments may be performed on one sample, the correspondence between experiment number and the sample number is given in Appendix 3.

2.2.1 Shear Compliance

The samples of granite were short hollow cylinders ranging in length from 25 to 35 mm, and had inner diameters of 26 to 54 mm. Outer diameters were in all cases about 88 mm. Tuff samples began as short cylinders 44.45 mm long. Inner diameters were 50.8 ± 0.13 mm and outer diameters were 88.9 ± 0.25 mm. Some of these were later remachined to lengths of 16.9 mm with inner diameters increased to 69.8 mm. The reason for this was to study samples with a smaller wall-thickness-to-radius ratio. The samples to be used for basic friction studies were first glued to end pieces, either aluminum or steel, that could be bolted into the machine. Before mounting in the machine, the sample-endplate assembly was placed in a surface grinder and the surface of the sample ground flat so that the rock surface was parallel to the surface of the endplate; i.e., the two ends of the assembly were made parallel; this ensured that the joint would be perpendicular to the axis of rotation when mounted in the machine.

Samples to be studied for rough joint response were selected from those described in the next section, after a tensile fracture had been created. These were already mounted to endplates as discussed below and were mounted in the rotary shear machine as they were after normal stiffness testing.

2.2.2 Normal Stiffness

The original samples for normal stiffness testing were hollow cylinders 133.35 mm long with an 88.9 ± 0.25 -mm outside diameter and a 50.8 ± 0.13 -mm inside diameter. The ends were parallel to within 0.1 mm. Machined into the outside surface was a circumferential groove lying in a plane perpendicular to the cylinder axis. The groove was originally 1.6 mm wide and 3.175 mm deep with an approximately flat bottom. The

groove dimensions and shape evolved through testing to the currently used depth of 6.35 mm with a V-shaped bottom having radius of curvature of 0.127 mm. This change in depth and shape came about through attempts to get a fracture contained entirely within the machined groove. Metal endplates identical to those noted above were glued to the ends of the rock cylinder. Next the endplate-rock-endplate assembly was mounted in the rotary shear machine and pulled in tension. After creating a fracture within the groove, the sample was ready for normal stiffness testing, and subsequent shear testing.

2.3 Test Procedures

2.3.1 Shear Compliance

Normal stress history effects

The effect of constant normal stress on the frictional properties of rock has been often studied. A standard test procedure is to apply a known, constant, uniform normal stress, and then to increase the shear stress until sliding is established [see references in *Byerlee, 1978*]. The rotary shear machine is being used to study, in addition to this effect, the influence of changes of normal stress, and, more particularly, the effects of the way the normal stress is changed. Thus, the whole history of the normal stress is being taken into account. This is a very new field, and the rotary shear machine is singularly appropriate to this type of testing. Basically, four different normal stress histories are applied:

1. In the simplest type of test, an initial normal stress is applied to a stress-free sample. Then, the twist is increased until steady sliding conditions are achieved as evidenced by an essentially constant torque. Then, the torque is reduced to zero, and subsequently the normal stress is reduced to zero. Next, the sample is repositioned before the normal stress is increased to some new value and sliding is again established. This procedure is repeated several times.
2. A slightly different kind of test is run in which after achieving steady sliding at a given normal stress, the sliding is stopped by placing the function generator in hold, and then the normal stress is increased or decreased to a new value. Subsequently, sliding is again established. This procedure is repeated for both increments and decrements in normal stress.
3. An experimentally more difficult type of test is run in which, after the establishment of a steady torque, the normal stress is changed nominally instantaneously

during continued uniform sliding; in other words, a step-function normal-stress-time history is applied.

4. A variant of number 2 above is run in which the normal stress is set to zero between changes to new operating levels.
5. Lastly, a completely new type of test has been devised that is suggested by the constitutive equation (1.6). For this test, the sample ends are brought together so that they just touch under essentially zero normal stress. Then, following the establishment of a constant rate of sliding, the normal stress is increased at a constant rate. This normal stress rate is chosen to be such that steady sliding continues throughout. In this way, a complete slip condition can be obtained with one sample in one test. Thus, the effect of sample variability can be completely eliminated and may be studied separately.

Sliding velocity effects

The effect of the sliding velocity on the frictional strength has been studied by running separate tests at a given normal stress and applied sliding rate [e.g., *Olsson*, 1974]. More recent rate sensitivity investigations [e.g., *Dieterich*, 1979] are run in a manner consistent with constitutive equation (1.6). For example, after steady sliding has been established at a predetermined velocity and normal stress, the velocity is suddenly changed by a known amount. The subsequent shear stress response is monitored continuously. There are two parameters to be obtained by rate testing: (1) the magnitude and sign of the instantaneous change in frictional strength caused by a step in the sliding velocity at constant normal stress and (2) the magnitude and sign of the residual friction strength dependence on velocity.

2.3.2 Normal Stiffness

Attempts at measuring the stress-closure relation in the rotary shear machine immediately after the fracture was formed proved unsuccessful. The original idea for testing in this configuration was that while the sample was held in axial alignment after the fracture was formed, it could be rotated to mismatch the rough surfaces by a predetermined amount and then brought back into contact for stiffness testing. However, the probability is that the largest asperities cause the sample halves to be in contact at only one or two points. This leads to very poor sampling and is probably not particularly representative of the true stiffness. Therefore, the procedure was changed so that after introducing the tensile fracture in the rotary shear machine, the sample was removed to a standard compression frame where a hemispherical loading seat allowed the fracture

surface to be initially in more uniform contact; at three points, at least. Following the stress-closure test in the standard load frame, the sample was returned to the rotary shear machine where the shear response of this rough surface was measured. The shear response for a sample with a laboratory-induced tensile fracture is described in section 3.6.

The sample had strain gauges mounted on the inside and outside cylindrical surfaces at the ends of two orthogonal diameters. In addition, a linear variable displacement transducer (LVDT) measured total displacement from endcap to endcap. The sample was then loaded in compression several times, both with the opposing fracture surfaces mated and unmated. Strains, displacement, and load were recorded continuously throughout the test.

Chapter 3

EXPERIMENTS AND DATA REDUCTION

3.1 Displacement Measurement

There are two methods for measuring the joint deformations u_i^j . Both are based on the fact that the total measured displacement δ_i^t , can be decomposed as

$$\delta_i^t = u_i^r + u_i^j + u_i^m, \quad (3.1)$$

where u_i^r is the displacement contribution due to the rock, u_i^j that due to the presence of the joint, and u_i^m that due to the machine. u_i^j can be further decomposed according to (1.1). In some setups, $u_i^m = 0$ because the displacement measuring device is located entirely on the sample. The simplest and probably the most accurate method is to measure the overall displacement, δ_i^t , of an intact sample, including any machine part(s) comprising the gauge length, and then repeat the process after the joint has been introduced. Subtracting the two curves gives the response in terms of the joint displacement, u_i^j , alone. The second method is required if the sample is from the field and already contains a natural joint; then, an independent measure of u_i^r is necessary, often accomplished by means of a strain gauge on the sample.

3.2 Stresses on the Interface in Rotary Shear

3.2.1 Preslip Shear Stress Profile

The relationship between the tangential shear stress and the applied torque in the

joint plane before the onset of slip is found from elasticity theory [e.g., *Timoshenko and Goodier*, 1970]. If the torque is denoted T , the shear stress τ , and the radial coordinate r , then

$$\tau(r) = \frac{rT}{J}, \quad (3.2)$$

where $J = (\frac{\pi}{2})(R_o^4 - R_i^4)$ is the polar moment of inertia for an annulus of inner and outer radii R_i and R_o , respectively. Thus, the maximum elastic shear stress is $R_o T/J$.

3.2.2 Fully Sliding Shear Stress Profile

After the full establishment of slip, that is, when slip is occurring everywhere simultaneously over the joint, then the torque-stress relation is statically determinate. It has the same form as for a fully yielded plastic tube [*Smith and Sidebottom*, 1969], that is, the friction stress, τ_f , is found from

$$\tau_f = \frac{3T_{fs}}{2\pi(R_o^3 - R_i^3)}, \quad (3.3)$$

where the subscript fs denotes "fully sliding". The underlying assumption in deriving (3.3) is that the material has a flat-topped stress-displacement diagram in direct shear, analogous to the perfect elastic-plastic assumption in the torsion of elastic-plastic tubes.

For an ideal, uniform frictional resistance, the ratio of the fully sliding torque, T_{fs} , to the torque at the onset of sliding, T_o , is found to be

$$\frac{T_{fs}}{T_o} = \frac{4(1 - \lambda^3)}{3(1 - \lambda^4)}, \quad (3.4)$$

where $\lambda = R_i/R_o$ and $0 \leq \lambda < 1$. Thus, for a solid cylinder, $\lambda = 0$ and $T_{fs}/T_o = 4/3$; for an increasingly thinner wall, $\lambda \rightarrow 1$ and $T_{fs} \rightarrow T_o$. Equation (3.4) is useful in estimating the variation in friction stress over a given test surface. This is because T_{fs} is a measure of the average friction stress over the entire test surface and is relatively insensitive to localized extrema in the properties. On the other hand, T_o is a function of the friction stress over a very thin annulus and, therefore, is more strongly influenced by localized fluctuations in the friction stress. Thus, departure of T_o from its value calculated from T_{fs} is a measure of the minimum friction stress occurring in the outermost annulus of the test surface. In addition, the difference $T_{fs} - T_o$ is a measure of the range in friction stress on the test surface. This type of measure was noted for plane strain joint deformation, also [*Olsson*, 1984b].

T_o may be a more critical design parameter than T_{fs} , because it is a measure of the shear stress at the onset of sliding rather than the steady-state sliding value computed

from T_f . It should be noted that the coefficient of friction, μ , calculated from T_f , corresponds to the classical and often-reported value. The significance of the difference in the value between the stress at the onset of slip and the stress during steady sliding does not yet seem to be generally appreciated by designers and modelers.

3.2.3 Shear Stress Profile During Partial Slip

The relationship between torque and shear stress within the slipping zone that holds after the onset of slip but before the fully sliding condition is more complex and is given by equations (A.1) through (A.3) in Appendix A. The shear stress outside the slipping zone is given by (A.22). Outside the slip zone, the stress (A.22) can be calculated after the dislocation distribution inside the slip zone is computed by (A.8). The relationships between τ_{∞} , τ_f , and τ_i are shown in Figure A1.

3.3 Comparison of an Experiment with the Theory

Comparison of the theoretical model response is made to the response of a Westerly granite sample. This rock was chosen as the developmental material because of its well known frictional properties and uniformity. The test surface had been run-in until the torque-twist loop was constant in size and shape. The normal stress acting across the ground surface was 10 MPa. The torque *versus* offset curve (Fig. 4) is qualitatively similar to the theoretical one (Fig. A2). The salient features of the curve are the sticking regions represented by vertical segments, the gradual onset of sliding, and the difference between the first quarter-cycle and all other quarter-cycles. The qualitative response of Topopah Spring tuff is similar in all respects to the granite and also to the model.

To judge the quantitative agreement, appropriate material properties are introduced into equations (A.7) and (A.11). The needed values are 25 GPa for the shear modulus, computed from data in *Brace* [1964], and the fully sliding torque, 1040 N·m, taken directly from the curve (Fig. 5). Then, T_o is computed by (3.2) to be 867 N·m. The first departure from the idealized response to be noted (Fig. 5) is the computed-*versus*-measured value of T_o . The onset of slip actually occurs near 750 N·m rather than the predicted value of 867 N·m. This difference in the fully sliding torque and the onset torque was discussed in section 3.2.2 in terms of the difference between the average shear strength and some measure of the minimum value. Next, a torque-offset curve using these parameters was computed and plotted on the axes of Figure 5; it is indistinguishable from the ordinate. This means that the stiffness (torque/slip) of the

idealized model is of the same order as the elastic stiffness. Therefore, all deformation exhibited by the torque–offset curve is the result of direct slippage on the interface and has no significant contribution from radial deepening of the slip zone. Further experimentation on tuff samples with more strain gauges and several wall thicknesses is needed to substantiate this; but, if it holds true, then it is a very significant result from a practical point of view because it means that for all torques greater than T_o , the shear stress is simply found from the torque by (3.3) rather than from the integration of (A.2) with (A.3) and (A.22). In other words, the torque–offset curve may be read as a shear stress–slip curve, directly.

3.4 Shear Compliance of Smooth Surfaces

3.4.1 Evolution of Shear Strength During Steady Sliding

Strength evolution with ongoing slip for Topopah Spring tuff (RFT058, Fig. 6) is often observed. The starting surface had been ground flat and lightly sandblasted to a dull finish. There are five loading phases in this test at 5 MPa normal stress; all were restarted at the same position for each run. The first three loadings were run consecutively. Then, the surface was blown clean with compressed air and wiped with a disposable paper wipe. This was repeated after the fourth loading. Notice that a constant value of the fully sliding torque, T_{fs} , is reached at the third loading cycle and remains constant with successive cycles so that loadings 3, 4, and 5 nearly coincide. Most testing for basic friction properties was done in the “run-in” state, that is, after having reached a stationary value of T_{fs} for a clean surface.

3.4.2 Strength Increases during Stationary Contact

The time-dependent strengthening of rock interfaces during stationary contact was systematically studied by *Dieterich* [1972]. He found that the initial sliding stress was a function of the length of time that the interface was stationary at a constant normal stress. An apparent example of this effect is shown in Figure 7 for Topopah Spring tuff test RFT026. The displacement (angle) hold was of 150 s duration, during which the strength increased about 8%. Resumption of loading causes slip-weakening to the original steady value. No systematic data are available on this effect as yet, but this would seem to be an important phenomenon. It is possible that this slip weakening is actually a time-independent effect and, as discussed below, may be a true indication of the existence of identifiable static and dynamic coefficients of friction. If this is a time-

dependent effect, it is a manifestation of the stress and velocity history dependence of the mechanical properties of joints in welded tuff.

3.4.3 Effects of Sliding Velocity History

Increases in the steady-state sliding velocity on joints in Topopah Spring tuff cause decreases in the shear strength; concisely, $d\tau_{ss}/dV < 0$. This is the opposite of the rate effect found in intact rock but is a common finding in friction studies at low normal stress. In test RFT028 (Fig. 8 and 9), normal stress 5.8 MPa, the overall rate of decrease of stress is about 5% per decade increase in sliding velocity over the range 0.1 to 100 $\mu\text{m/s}$.

More subtle than the difference in steady-state strengths at different steady-state velocities is the effect of the history of the velocity. For example, if a Heaviside (step) velocity history is imposed on the sliding surface, and if the stress is a direct function of the velocity, then the stress should exhibit a step change, also. However, as shown by the curve in Figure 8 and 9, when the velocity is stepped up, the stress first jumps up, then gradually decays to a new lower value. Recalling the definitions of A and B from section 1.2.4, these changes, at constant normal stress, are described by

$$\left(\frac{\partial \tau}{\partial V}\right)_{\text{fixed state}} = A \ln(V/V_0) \geq 0, \quad (3.5)$$

indicating the instantaneous change, and

$$\frac{d\tau_{ss}(V)}{dV} = (A - B)/V \quad (3.6)$$

which describes the steady-state velocity effect as $\tau(t) \rightarrow \tau_{ss}$. The notation "fixed state" is consistent with the experimental fact that no slip occurs during the instantaneous jump in V ; thus, we are assuming that the state of the surface changes only with ongoing time or slip.

Thus, A and B characterize the rate dependence of the material. The following table gives a few representative values of the parameters for RFT028 for positive velocity jumps.

V_0	A	B	B_D	$L (= d_r)$	$d\tau_{ss}/dV$
(μm)	(MPa)	(MPa)		μm	(MPa/ $\mu\text{m/s}$)
0.1	0.032	0.086	-0.021	65	-0.054
1.0	0.019	0.052	-0.021	86	-0.003

The characteristic slip distance called L here is referred to as d_r by *Dieterich* [1981]. The values for Topopah Spring tuff are of the same magnitude as for joints in granite with various thin layers of granite gouge. B_D is a rate sensitivity measure defined by *Dieterich* [1981] as $B_D = \Delta\mu / \log_{10}(V/V_0)$, where μ is computed with the steady-state values of shear stress. This parameter for Topopah Spring tuff (Fig. 10) is a factor of 2 greater in magnitude than those for the gouge-filled joints in granite just mentioned. *Soldberg and Byerlee* [1984] find $B_D > 0$ for gouge filled joints in granite under triaxial compression. The effect of gouge on Topopah Spring tuff is as yet unknown. The sign of B_D , or that of $A - B$, is important because if positive, only stable sliding is a possible motion, whereas, if negative, instabilities are possible. These results show that Topopah Spring tuff is somewhat more rate sensitive than Westerly granite [*Dieterich*, 1978].

Data from two samples suggest that $A = 0$ for velocity jumps from 100 to 10 $\mu\text{m/s}$ and from 10 to 100 $\mu\text{m/s}$. Velocity jumps from 0.1 to 1 $\mu\text{m/s}$ always give $A > 0$. The steps from 1 to 10 $\mu\text{m/s}$, and the reverse, give small values of A . It appears that there is a critical velocity above which no transient strengthening occurs, and that A may depend on V_0 .

3.4.4 Effects of Normal Stress History

Two sets of experiments were carried out to investigate the potential effects of *changes* in normal stress. The first set to be discussed is less precise in terms of the constitutive theory in (1.6) because the slip velocity was not maintained constant nor were the various hold times encountered in the test determined *a priori*, although they were recorded. Therefore, the stress changes were made during stationary contact. In the second set of experiments, the normal stress changes were made during continuous sliding.

Normal stress changes during stationary contact

Two different types of test were run during periods of twist hold (nominally no slip) to investigate the effects of normal stress history, $\sigma_n(t)$. Figures 11 and 12 show representative results. The first type of test, represented by RFT030, shows the stress history with the most pronounced effect (Fig. 11). First a constant normal stress of 3 MPa was applied. Then, the twist was begun, which caused a torque build-up until the onset of slip at about 200 N·m. Next, seven unload/load loops were introduced. The first through fourth, and the seventh were done during constant normal stress. However, the fifth and sixth unload/load loops were accomplished by holding the angle constant and reducing the normal stress to zero, reapplying 3 MPa, and retorquing.

In each case where the normal stress was maintained constant during the unload/reload cycle, the torque-twist curve is characterized by a small stress peak at the resumption of slip during reloading. In the unload/reload loops accompanied by momentary vanishing of the normal stress, the torque-twist curve takes on a shape very similar to the initial loading. The small difference in the curves obtained after σ_n has been reduced momentarily to zero is attributed to the fact that the surfaces are in contact in different locations.

The second type of normal stress history test is illustrated in Figure 12. Here the normal stress was raised successively through prechosen steps while the angle was held momentarily constant. A marked effect of the history of the normal stress is apparent in this figure. After each successive increase in normal stress, the torque-twist curve shows a more rapid onset of fully sliding conditions, as manifested by the sharper "yield" regions. After the increase to $\sigma = 5$ MPa, the onset of slip is characterized by a peak in the torque-twist curve. The portion of the torque-twist curve characterized by a negative slope is referred to as slip-weakening.

All unloading steps in normal stress show slip weakening except for the 3 to 2 MPa jump.

Summarizing, there are four related phenomena that seem to result from changes in normal stress at stationary contact.

1. After unloading from the slipping regime, while maintaining the normal stress constant, the onset of renewed slip is very rapid, giving a torque-twist curve that suddenly resumes the original path. Usually, the sharp yield is punctuated by an additional small blip. (Fig. 11, reloading loops 1, 2, 3, and 4; Fig. 12, normal stress increments 4 to 5 and 5 to 6 MPa).
2. After momentarily reducing the normal stress to zero and then retorquing, the

shape of the torque-twist curve resumes its original, first-time torquing shape (Fig. 11, torquings at 3.8 and 5.4 deg).

3. When the normal stress is increased while maintaining the angle of rotation constant, and without first reducing the normal stress to zero, the onset of sliding is progressively more rapid after each normal stress change (Fig. 12). As in item 1, the later positive normal stress increments are enhanced by a small spike.
4. On decrements of normal stress, the onset of slip is rapid (Fig. 12, decreasing steps in normal stress) and exhibits slip weakening.

These features can be explained by an extension of the dislocation theory of the stress history of frictional slip presented by *Olsson* [1984]. As shown in section 3.3 the in-plane tangential shear strain is for practical purposes negligible at the low normal stresses encountered in this testing program. This causes the joint dislocational deformations to be dominantly of edge type (lines parallel to radii, Burgers vectors tangent to the circumferences) rather than screw type (lines circumferential, Burgers vector radial). The fundamental hypothesis is that friction on some relevant scale is nonuniform as sketched in Figure 13a. In the simplest case, the frictional stress, τ_f , is just the product of the effective normal stress times the coefficient of friction and thus any variation in either causes variation in frictional stress along the joint. The indications of non-uniform friction stress in the present case are abundant (see sections 3.2.2 and 3.4.5). The variability in friction causes all the non-creep-related slip that accumulates between the onset of slip at T_o and the attainment of fully sliding conditions at T_{fs} ; it is due to localized patches of slip that spread to cover the entire cross section.

The normal stress history dependence revolves around the interaction history of the several stresses τ_∞ , τ_f , and τ_i , i.e., the applied stress, the friction stress, and the internal stress. For analytical tractability, let us assume that the friction stress in the neighborhood of one of the local minima, such as S in Figure 13a, varies with distance away as $|x|$ such that

$$\begin{aligned} \tau_f(x) &= \tau_0 + (\tau_1 - \tau_0)|x/a| & x \in [-a, a] \\ \tau_f &= \tau_1 & x \notin [-a, a] \end{aligned} \quad (3.7)$$

where τ_1 and τ_0 are defined in Figure 13b. The half-width of the slipping zone is b , and the half-width of the V-shaped friction inhomogeneity is a . Assume also that the applied stress is uniform with position.

Figure 13 shows the three existing components of shear stresses, (1) the applied far-field stress, $\tau_\infty(x)$, (2) the frictional resistance $\tau_f = \mu\sigma$, and (3) the internal stress $\tau_i(x)$. The internal stress also goes by the names dislocation stress and elastic backstress. The

relationship between them within the slipping zone is $\tau_\infty(x) + \tau_i(x) + \tau_f = 0$. For an interface that has undergone no inhomogeneous slip, there will exist no internal stress, $\tau_i(x) = 0$, and the applied stress must just equal the friction stress for slip. Note that by interchanging the roles of the applied stress (now uniform), with the friction stress (now a function of position) the problem is analogous to that solved in the appendix; slippage in each case is driven by the difference $|\tau_\infty - \tau_f|$. Outside the slipping zone, the internal stress is obtained from the displacement as shown in the appendix in (A.22). For the specific direct shear variables these equations read:

$$\begin{aligned} \tau_i(x) &= \tau_f(x) - \tau_\infty & x \in [-b, b] \\ \tau_i(x) &= (2(\tau_1 - \tau_0)/\pi a) [x \arcsin(b/x) - b] & x \notin [-b, b]; |b| < |a|. \end{aligned} \quad (3.8)$$

Suppose that after some inhomogeneous slippage has occurred and the slip zone has spread some distance b , the torque is reduced to zero, and then also $\tau_\infty = 0$. The friction stress and the internal stress will still appear as they do in Figure 13b and 13c, but the straight line indicating the applied stress will move downward to zero. Now, for a subsequent torque cycle, the internal stress on the joint can be considered as an additional friction stress so that the total resisting stress to further slip is $\tau_r(x) \equiv \tau_f(x) - \tau_i(x)$. See *Weertman* [1964] for a discussion of reloading of previously slipped interfaces. This resistive stress is plotted in Figure 13d. As the torque is increased from zero, the straight line $\tau_\infty(x)$ begins to move upward, eventually contacting the total resistance curve, $\tau_r(x)$, over the entire extent of the previously slipped zone, $[-b, b]$. Thus, the onset of slip is more sudden than the first loading because the entire previously slipped region begins at once to slip again, and, therefore, the slope of the torque-twist curve is the same as it was at the immediately previous cessation of torquing. To regain the original torque-twist curve one needs only to reduce the normal stress to zero, which in turn releases all locked-in internal stress. Then, the resistive stress is just equal to the friction stress alone, and the problem is just as it was at the beginning. After reapplying the normal stress and the torque is again increased, the slip will start at the minimum in friction when $\tau_\infty(x)$ just equal to $\tau_f = \tau_0$.

The slip weakening behavior at the onset of slip may result from the time-dependent strengthening that occurs during the period of untorquing and retorquing when the interface is stationary. Alternatively, this may be a time-independent material response that is usually masked by the effects of nonuniform stress on the spread of slip zones during torquing from stress-free states. The fact that slip-weakening occurs on the initiation of slip immediately following normal stress decrements actually supports the idea that this is a time-independent response rather than time-dependent strengthening. If the spike was the result of time-dependent strengthening, it seems unlikely that it would occur on normal stress decrements because during those phases, the surface is in a constant state of slippage, which is inconsistent with strengthening during stationary contact.

Observations 1 and 2 above are thus explained in terms of the relative size of the slipping area compared to the total area. Explanation of the effects of normal stress increments, $\Delta\sigma$, made without prior reductions to zero of the applied stress seems to be the result of the same phenomenon. Assume that after a normal stress increment of $\Delta\sigma$, the total resistive stress is given by $\tau_r \equiv (\tau_f + \mu\Delta\sigma) - \tau_i(x)$ (Fig. 13e). Therefore, increments in normal stress cause upward translation of the total resistance curve, and decrements cause downward translation. These changes are carried out during nominally stationary contact. Notice that after an increment in normal stress shifts the total resistance curve upward, renewed torquing causes the τ_∞ line to move upward to coincide with the total resistance curve over the entire slipped interval again, just as in the case where there is no intervening increase in normal stress. Thus, the simple relationships between the stresses sketched in Figure 13 can explain most of the stress history effects observed in these types of tests.

The type of behavior shown in Figure 12 is referred to as discrete memory [Hueckel and Nova, 1979; Olsson, 1984]. The fact that torque-twist excursions from the slip condition are characterized by a return to the same point on reloading is thought of as the interface remembering that torque-twist point where it left the slip condition. The time that it takes to make the loop is inconsequential—the joint has a perfect memory for that particular torque-twist state. Temporary removal of the normal stress erases the interface's memory of past torques. There is little evidence of a fading memory in these tests.

With a view toward eventual connection of the mechanical response to the surface characterization, notice that a measure of the sharpness of the yield region on the torque-twist (stress-displacement) diagram is the difference, in some sense, between the applied stress, $\tau_\infty(x)$, and the resistive stress, $\tau_r(x)$. A unique measure for the relationships shown in Figure 13 is $\max |\tau_1 - \tau_0|$; for $\tau_\infty = \tau_0$, this is called the maximum norm. This was noticed in an earlier study on direct shear slippage [Olsson, 1984b]. In that study, it was emphasized how inhomogeneous resistive stress; possibly the result of variations in normal stress, pore pressure, friction coefficients, etc., affected stress-displacement curves for slippage. Because the frictional resistance of a natural fracture is likely to be a much more complicated function of position than that of Figure 13, it is necessary to give more precisely the state of slippage or, equivalently, the closeness to the slip condition for each point along the interface. It is necessary to specify the "distance" between the two curves, $\tau_r(x)$ and $\tau_\infty(x)$. The maximum norm could be used to specify this distance, but it is sensitive to only the maximum and does not take into account how the resistive stress actually varies with x . Thus, if the maximum norm is very high at just one point in the interval of interest, in this case, the whole test surface, and the rest of the surface was near to the slip condition, then this is not a useful measure.

For a surface characterized by a spatially variable resistance to slip, there may be many local extrema in $|\tau_r(x) - \tau_\infty(x)| = \phi(x)$ over any interval of interest. Under these circumstances, a more appropriate measure of the distance between the two functions, or the size of ϕ , is the *mean square norm*, $\|\phi\|$, defined as

$$\|\phi(x)\|^2 = \frac{1}{d} \int_0^d \phi(x)^2 dx. \quad (3.9)$$

Now, the size of the mean square norm, when it can be calculated, will be a predictor of the rate of onset of sliding, or the sharpness of the torque-twist (stress-displacement) curve. In other words, the magnitude of $\phi(x)$ is a measure of the propensity of the interface for unrestrained sliding.

Normal stress change during constant velocity slip

It is apparent from the structure of (1.6) that the search for normal stress history effects parallels that described in the previous section on velocity history effects. That is, the putative effect of past normal stress history should be most simply found by subjecting the surface to a normal stress step while maintaining constant sliding velocity. Figures 14 and 15 show some results of this procedure. In test RFT064 (Fig. 14), run on a surface that had been ground and run-in, the normal stress was suddenly increased by 0.7 MPa while the sliding velocity was maintained constant at 10^{-6} m/s. This sample had a slip gauge mounted across the joint, verifying that the velocity of sliding remained constant during the normal stress increases. The result that the shear stress is a square-wave function of the slip, just as is the normal stress, shows a lack of significant effect of normal stress change.

A marked effect of normal stress history was found, however, in test RFT077 (Fig. 15). This test surface was ground and run-in, also. No slip gauge was mounted on this specimen so the slip velocity was calculated from the rotation rate as 10^{-5} m/s. The finite initial slope of the shear stress-slip curve at the point of normal stress increase indicates that the slip must have momentarily stopped. The onset of nonlinearity marks the resumption of slip. The shear stress then evolves to a new higher level over a slip distance of order 2 mm. It is thought that this brief (not more than a few seconds) period of stationary contact does not alter the conclusion that a true effect of normal stress history is shown. In any case, if some time-dependent strengthening occurred during this period of no slip, it should have the effect of increasing the amount of observed instantaneous shear stress increase. The test record for RFT077 gives $(\partial\tau/\partial\sigma)_{state} = 0.31$, $d\tau_{ss}/d\sigma = 0.8$, and a slip distance, L_V , for the transient increase of about 1.85 mm.

The data from this type of test is not yet systematic enough to determine why some tests show a fading memory effect and others do not. The differences between the two

tests just described are the difference in σ_d ; 0.7 MPa for RFT064, which does not show a transient in shear stress, and 1.4 MPa for RFT077, which does. Also, the sliding velocity is different by two orders of magnitude. Further testing may shed light on this problem.

To date, six tests with stepped normal stress histories show memory effects, and the data are summarized in the following table, where L_V is the distance over which the shear stress evolves to a new steady value at a constant slip velocity.

Test Name	V_0 (m/s)	$(\partial\tau/\partial\sigma)_{state}$	$d\tau_{ss}/d\sigma$	L_V (mm)
RFT035	2.5×10^{-5}	0.28	0.32	0.03
RFT036	2.1×10^{-5}	0.15	0.35	0.14
RFT037	2.5×10^{-5}	0.16	0.37	0.21
RFT074	1.3×10^{-5}	0.29	0.77	0.41
RFT075	1.3×10^{-5}	0.46	0.67	1.45
RFT077	1.3×10^{-5}	0.31	0.80	1.85

An alternative method of determining μ_V is to differentiate (1.6) at constant V , arriving at

$$\frac{d[\tau(t) - \tau_{ss}]}{dt} = \mu_V(t)[\dot{\sigma}] \quad (3.10)$$

where $[\dot{\sigma}]$ is the jump in the value of the normal stress rate at time $t = 0$. This test is described in part 5 under section 2.3.1. Briefly, at $t = 0$, the sliding is begun at zero normal stress, then the normal stress is raised at a constant rate $[\dot{\sigma}]$. Unfortunately, plots of differentiated experimental data often are very noisy, making interpretation difficult. One example with a fairly good output is shown in Figure 16. The time-dependent generalized coefficient of friction is given directly only by the part of the curve between about 50 and 150 s, that is, only during the increasing normal stress phase. The rest of the curve, in principle, can then be computed using the data from the first phase. Examination of the complete data set shows that $d\tau(t)/dt$ usually decreases somewhat with time during the first loading phase.

Note that after setting $V_d = 0$, (1.6) can be rewritten

$$\tau(t) = \tau_0 + \int_{-\infty}^t \mu_V(t-t')\dot{\sigma}(t') dt', \quad (3.11)$$

or, because $\dot{\sigma} = \sigma/t$, as [Smith, 1976]

$$\Sigma(t) \equiv \frac{\tau(t)}{\sigma(t)} = \frac{1}{t} \int_0^t \mu_V(t-t') dt', \quad (3.12)$$

where $\tau_0 = 0$ because $\sigma(0^-) = 0$, and $\Sigma(t)$ is called the constant stress rate modulus. Differentiating with respect to t results in $\mu_V(t) = \Sigma(t) + t d\Sigma(t)/dt$ or

$$\mu_V(t) = \Sigma(t) \left[1 + \frac{d \log \Sigma(t)}{d \log t} \right]. \quad (3.13)$$

Hence, $\mu_V(t)$ can be obtained by computing the slope of the plot of $\log \Sigma(t)$ versus $\log t$ and using the result as a correction factor on $\Sigma(t)$. Figure 17 shows the result for four tests at several combinations of slip velocity and normal stress rate. The slopes lie between 10^{-6} and 10^{-3} ; clearly, the correction factor is very small in comparison to 1. Thus, the generalized coefficient of friction, $\mu_V(t)$, is defined simply by a plot of $\tau(t)/\sigma(t)$ versus t (Fig. 18). The negative, constant slope of μ_V in semilog space indicates that the process is represented by a decaying exponential as is often found for μ_σ [Dieterich, 1979; Ruina, 1983].

Equation (3.11) indicates that the current shear stress may be a function of the applied normal stress rate. This was checked in RFT078 by stepping the rate by a decade during steady sliding. Figure 19 shows that the rate of increase of shear stress with normal stress decreases by nearly half when this is done.

3.4.5 Slip Condition

It was noted in an earlier section that the slip condition was essentially a surface in stress space that separates the elastic, preslip behavior from the sliding behavior; for example, $|\tau| - \mu\sigma = 0$. The usual method of constructing the slip condition is to plot some chosen value of shear stress against the appropriate normal stress. There are infinitely many values of shear stress for slippage explicit in each torque-versus-angle curve, bounded below and above by T_0 and T_{fs} , respectively. Some results are shown in Figure 20 for test RFT059. This figure represents the results of four sequential friction tests on the same surface at normal stresses of 2, 4, 6, and 4 MPa. The fourth test, at 4 MPa, reproduces the second test, also at 4 MPa, nearly exactly so that surface evolution was not a factor. The triangles represent the shear stress required for the onset of slip, τ_0 , at the outer edge of the test surface; the circles were computed at the steady sliding stress, τ_{fs} . The lines through these data points are best-fit power laws. The region bounded above by τ_{fs} and below by τ_0 is characterized by slip hardening response. The difference in the τ_{fs} and the τ_0 curves is due only to evolution of the

frictional resistance. The deviation of the measured value of τ_0 from τ_{fs} is assumed to result from fluctuations of the friction stress. In other words, the experimentally observed value of stress for the onset of slip is less than the theoretical value because the frictional stress is less than the average value in some regions. For details on how the stress path in relation to these two curves influences stress-slip response, see *Olsson [1984]*.

This particular example (Fig. 20) is extreme, $T_{fs}/T_o = 2.17$ compared to the ideal value of 1.214. Another curve such as that for RFT030 (Fig. 11) shows $T_{fs}/T_o = 1.6$ and is more typical of the data base as a whole. Evidently, the vertical distance between τ_{fs} and τ_0 is connected by $||\phi(x)||$ to the spatial variation of the surface properties. Thus, initially smoother surfaces would approach the theoretical T_{fs}/T_o of 1.214 as $||\phi(x)|| \rightarrow 0$.

A new way to determine the slip condition is based on the test type described in the preceding section. This procedure maps out the slip criterion in one test on one surface, and in this way removes all specimen variability effects. Figure 21 shows the results of a typical test of this type. Here, after the establishment of uniform, constant sliding velocity at nominally zero normal stress, the normal stress was ramped at a constant rate until 5.4 MPa was reached, whereupon the normal stress was ramped downward to zero, again at a constant rate. This sample had been well run-in and was wiped clean of gouge before running this test. There is a clear normal stress history effect present in this test. On loading, the relation between τ_f and σ is linear with $\mu_V = 0.57$. On unloading, however, μ_V is initially 0.33 and increases to 0.83. The increased shear stress at any given normal stress on unloading compared to the shear stress at the same normal stress on loading may be due to the crushing of the asperities into more intimate contact at the highest normal stresses, causing greater contact area during unloading.

The shear stress for fully sliding conditions for several different stress paths is superimposed in Figure 22, two (RFT056, RFT062) stepped, one individual (RFT059), and two continuous (RFT063, RFT065). For comparison, the range of stresses during run-in of RFT058 is included. In terms of the slope of any line that might be drawn through the points, there is not much to be distinguished. The continuous curve is lower than the discrete points.

The effect of the underlying sliding velocity is shown in Figure 23. Here the velocity is different by a factor of 10. The slip condition is lower for the higher velocity test as would be expected from the previous discussion. The interpretation of this data is difficult at this time because it is not known whether these data represent steady-state as defined above. Nevertheless, this test type represents one way of defining the steady-state velocity; for example, tests could be run at successively slower velocities until there is no increment in $\tau(\sigma)$ for an increment in V .

3.5 Shear Compliance of Rough Surfaces

Sample 16D was a grooved cylinder pulled in tension to form a rough fracture. The surface profile of the laboratory-induced tensile fracture was measured with a profilometer, and the maximum amplitude was found to be 1.91 mm. The sample was tested for normal stiffness, as described below, and for shear stiffness, as now explained. Test RFT013 was the shear stiffness test run on sample 16D at a nominal normal stress of 2 MPa, the results of which are summarized in Figure 24. In the development of this test type, it was first thought that the specimen deformation could be computed from the strain gauge outputs, but the most accurate method is to measure the total deformation before and after the fracture is introduced and then subtract, as described above. Thus, in an after-the-fact manner, the total specimen-machine deformation in shear was measured after the fracture was formed by carefully mating the two sample halves back together, applying the normal stress, and then twisting. Because the rough surface was mated and the asperities were interlocked, no slippage occurred if the torque was kept below 70 N-m. The torque-angle relation thus obtained, which represents the combined stiffness of the specimen plus the machine, is shown in Figure 24 by the squares. The dashed curve represents the total deformation in a subsequent test carried to torque sufficiently high as to cause fully sliding conditions. This test was begun in the unmated condition. When the elastic, rock+machine curve is subtracted from the total deformation, the joint deformation curve is obtained (solid line, Fig. 24). The data show that $\infty \geq K_{tt} > 0$, that is, the shear stiffness is infinite until the stress is sufficient to induce sliding, whereupon the stiffness decreases monotonically to near zero as sliding progresses.

The verticality of the unloading curve indicates that there is virtually no elastic recovery so that, recalling (1.1), $\bar{u}_i^t = 0$. The coincidence of the u_i^t curve with the $u_i^t + u_i^m$ curve in the linear range shows that the simplest way to determine the contribution of the joint alone is simply to remove the elastic deformation calculated from the slope of this linear portion from u_i^t . That is, the elastic contribution to the total deformation is made up entirely of machine and intact rock contributions.

3.5.1 Dilatancy

During the shear test on sample 16D, described in the previous section, the dilatancy, $\beta = \partial u_n / \partial u_t$, was also measured. This is the only value currently available for Topopah Spring tuff. Figure 25 shows the torque and dilatancy plotted against slip angle. The joint shows monotonic compaction with increasing slip. During untorquing, the dilatancy remains essentially stationary. It seems probable that if the test had

begun with the joint halves mated, there would have been joint opening rather than closing.

3.6 Normal Stiffness

3.6.1 Experimental Observations

Normal stiffness testing was successfully carried out on sample 16D in tests NST005 through NST008. Rock displacement, \bar{u}_n^r , was computed from strain gauge readings taken from the external sample surfaces. The linearity and recoverability of the gauge output justifies the use of the overbar on the rock displacement, i.e., the rock response is linear elastic. Axial displacement, $\bar{u}_n^r + u_n^j$, was measured with an LVDT located coincident with the sample axis. Forming the difference of these two quantities gives the response of the joint alone (Fig. 26). In the mated condition, the near closure of the hysteresis loops (Fig. 26) indicates that $\bar{u}_n^j \approx 0$. In the mated condition, then, the cyclic loading response of the joint in normal closure is, to a very good approximation, nonlinearly elastic.

Next, the sample halves were rotated with respect to one another about the cylinder axis to achieve a completely unmated condition then loaded in compression again to obtain the stiffness of a rough joint (Fig. 27). Again, the elastic rock deformation was subtracted from the total to obtain the joint response. The most obvious difference between the response of the unmated and the mated surfaces is the large displacement at a given stress for the unmated surfaces. For example, at 5 MPa the closure of the mated surface is about 50 μm compared to 200 μm for the unmated surface.

Additionally, both the size of the hysteresis loops and the amount of permanent, nonrecoverable deformation are greater for the unmated surface. The increased hysteresis indicates greater contribution from frictional processes. Increased plastic deformation of the the asperities causes the larger permanent deformations. Apparently, the mated joint is completely closed by a normal stress of 3 MPa, whereas the unmated surface is still closing rapidly at the maximum achieved stress of 6 MPa.

Differentiating the stress–displacement relations gives the normal joint stiffness, K_{nn} which is plotted for both mated and unmated conditions in Figure 28. The stiffness of the mated joint ranges from 0 to about 500 GPa/m at $\sigma_n = 9$ MPa. For the unmated joint the stiffness increases from 0 to about 100 GPa/m at a stress of 6 MPa.

Chapter 4

CONCLUSIONS

The results presented in this report suggest the following conclusions for room-temperature, air-dry Topopah Spring tuff.

1. The coefficient of friction can vary from an initial value of about 0.3 to a steady-state value of about 0.8. This range can be found on an individual clean, smooth surface.
2. The elastic (that is, preslip) shear stiffness of smooth and rough joints was found to be infinite when measured and calculated correctly.
3. All displacement attributable to slippage on the joint is plastic, that is, non-recoverable.
4. The normal joint stiffness is found to be consistent with results reported in the literature in that it is a continuously increasing function of normal stress. The normal closure displacement is composed of elastic (recoverable), plastic (non-recoverable), and frictional (recoverable but hysteretic) components.
5. Shear strength decreases by about 5% per decade increase in slip velocity.
6. The effect of a sudden change in slip velocity can be interpreted in terms of hereditary integral or internal state variable descriptions.
7. There may exist a critical velocity. Below the critical velocity, a sudden increase in velocity causes an instantaneous increase in strength, which then decays gradually to a new, lower value. Above the critical velocity, there is no instantaneous increase in strength following a jump in velocity—just a smooth decrease.
8. The strength of the joint may increase with time of stationary contact.

9. Normal stress history has a measurable effect on the strength; the slipping interface retains a fading memory of past normal stress.
10. The stress-path traversed on the way to the slip condition has a measurable effect on the observed strength, thus casting doubt on shear strength and stiffness data from triaxial tests run at constant confining pressure.
11. True slip-weakening for initially smooth surfaces may have been found in Topopah Spring tuff. This response is usually masked by inhomogeneous resistive stresses.
12. For the low normal stresses used in this study, the torque-twist curve appears to be a direct measure of the shear compliance of a joint; that is, there is no significant contribution from the radial growth of the slip zone. Thus, the rotary shear results should be directly comparable to those from other tests such as direct shear and triaxial, insofar as these data are collected from similar stress and velocity histories.

4.1 Outlook

Many avenues remain to be explored, but the next few steps in the research program should attempt to:

- Define the magnitude and implications of the hereditary velocity and normal stress effects. This includes elucidation of the effects of stress path. It is likely that stress path will be even more important for rough surfaces representative of some natural joints.
- Construct constitutive equations that describe nonlinear normal stress history effects not predicted by equation (1.6). This may be best done in terms of state variable descriptions.
- Identify the critical velocity, V_0 , that decides whether $\partial\tau/\partial V$ is positive or zero. This is important in stability considerations.
- Define the conditions under which slip-weakening may be observed.
- Compare the results from rotary shear with those from triaxial friction tests. This is important because the triaxial machine will be more convenient when water content and temperature are studied.

This should be followed by the introduction of the environmental variables:

- **Temperature**
- **Water content**

The influence of surface roughness, particularly with respect to joint closure, needs further work. The possible effects of gouge or infilling material has not been investigated, but if these materials are present, the problem of joint slip and closure will take on a completely different character.

REFERENCES

- Bandis, S. C., A. C. Lumsden, and N. R. Barton, Fundamentals of rock joint deformation, *Int. J. Rock Mech. Min. Sci.*, *20*, 249-268, 1983.
- Barton, N. R., A model study of rock-joint deformation, *Int. J. Rock Mech. Min. Sci.*, *9*, 579-602, 1972.
- Brace, W. F., Brittle Fracture of Rocks, in *State of Stress in the Earth's Crust*, W. R. Judd (Ed.), Elsevier, New York, 111-174, 1964.
- Byerlee, J., Friction in rocks, *Pageoph.*, *116*, 615-626.
- Chen, E. P., Two-dimensional continuum model for jointed media with orthogonal sets of joints, in *27th Symp. on Rock Mech., Rock Mechanics: Key to Energy Production*, Univ. of Alabama, 1986.
- Christensen, R. J., S. R. Swanson, and W. S. Brown, Torsional Shear Measurements of the Frictional Properties of Westerly Granite, in *Advances in Rock Mechanics, Proceedings of the Third Congress of the International Society for Rock Mechanics*, 2214-225, 1974
- Dieterich, J. H., Time-dependent friction in rocks, *J. Geophys. Res.*, *77*, 3690-3697, 1972.
- Dieterich, J. H., Time-dependent friction and the mechanics of stick-slip, *Pageoph*, *116*, 790-806, 1978.
- Dieterich, J. H., Modeling of rock friction: 1. Experimental results and constitutive equations, *J. Geophys. Res.*, *84*, 2161-2168, 1979.
- Dieterich, J. H., Constitutive properties of faults with simulated gouge, in *Mechanical Behavior of Crustal Rocks: The Handin Volume, Geophysical Monogr. Ser.*, *24*, edited by N. L. Carter, M. Friedman, J. M. Logan, D. W. Stearns, 103-120, 1981.
- Erdelyi, W. W., F. M. Oberhettinger, and F. G. Tricomi, *Tables of Integral Transforms*, vol. 2, McGraw Hill, New York, 1954.
- Gladwell, G. M. L., *Contact Problems in the Classical Theory of Elasticity*, §3.2, Sijthoff & Noordhoff, Germantown, Maryland, USA, 1980.
- Goodman, R. E., and J. Dubois, Duplication of dilatancy in analysis of jointed rocks, *J. Soil Mech. Found. Div., ASCE*, *4*, 399-422, 1972.
- Goodman, R. E., R. L. Taylor, and T. L. Brekke, A model for the mechanics of jointed rock, *J. Soil Mech. Found. Div., ASCE*, *3*, 637-659, 1968.

- Gu, J.-C., J. R. Rice, A. L. Ruina, and S. T. Tse, Slip motion and stability of a single degree of freedom elastic system with rate and state dependent friction, *J. Mech. Phys. Solids*, *32*, 167-196, 1984.
- Holcomb, D. J., and A. K. Jones, Data acquisition for the rock mechanics lab, *SAND83-0646*, Sandia National Laboratories, Albuquerque, NM, 1983.
- Holcomb, D. J., and L. W. Teufel, Acoustic emissions during deformation of intact and jointed welded tuff, *SAND82-1009*, Sandia National Laboratories, Albuquerque, NM, 1982.
- Hobbs, B. E., and B. H. G. Brady, Normal stress changes and the constitutive law for rock friction, *EOS Trans. Amer. Geophys. Union* *66*, No. 46, 382, 1985.
- Hueckel, T., and R. Nova, Some hysteresis effects of the behavior of geologic media, *Int. J. Solids Struct.*, *15*, 625-642, 1979.
- Kutter, H. K., Rotary Shear Testing of Rock Joints, in *Advances in Rock Mechanics, Proceedings of the Third Congress of the International Society for Rock Mechanics*, 254-262, 1974.
- Leonov, M. IA., and N. IU. Shvaiko, Introduction to the Dislocation Theory of Elastic-Plastic Torsion, in *Problems of Continuum Mechanics*, SIAM, Philadelphia, PA., 260-266, 1961.
- Lockner, D. A., P. G. Okubo and J. H. Dieterich, Containment of stick-slip failures on a simulated fault by pore fluid injection, *Geophys. Res. Lett.*, *9*, 801-804, 1982.
- Mavko, G. M., Mechanics of motion on major faults, in *Ann. Rev. Earth and Planetary Sci.*, *9*, edited by G. W. Wetherill, A. L. Albee, and F. G. Stehli, Annual Reviews, Palo Alto, 81-111, 1981.
- Mavko, G. M., Easy computation of static stress drop, slip, and moment on two-dimensional heterogeneous faults, *Bull. Seismol. Soc. Am.*, *72*, 1499-1508, 1982.
- Michałowski, R., and Z. Mróz, Associated and non-associated sliding rules in contact friction problems, *Arch. Mech.*, *30*, 259-276, 1976.
- Mindlin, R. D., and H. Deresiewicz, Elastic spheres in contact under varying oblique forces, *J. Appl. Mech.*, *20*, 327-344, 1953.
- Muskhelishvili, N. I., *Singular Integral Equations*, p. 251, Noordhoff, Groningen, The Netherlands, 1953.

- Nunziato, J. W., K. W. Schuler, and D. B. Hayes, Wave propagation calculations for nonlinear viscoelastic solids, *Proc. Int. Conf. Computational Methods in Nonlinear Mechanics*, Univ. Texas, Austin, 1974.
- Olsson, W. A., Effects of temperature, pressure, and displacement rate on the frictional characteristics of a limestone, *Int. J. Rock Mech. Min. Sci.*, *11*, 267-278, 1974.
- Olsson, W. A., Some results from rotary friction tests, *EOS, Trans. Amer. Geophys. Union*, *63*, 1109, 1982a.
- Olsson, W. A., A translating slip condition for a jointed rock mass, *SAND82-0655*, Sandia National Laboratories, Albuquerque, NM, 1982b.
- Olsson, W. A., Experiments on a slipping crack, *Geophys. Res. Lett.*, *9*, 797-800, 1982c.
- Olsson, W. A., Rotary shear behavior of artificial joints in welded tuff, *EOS, Trans. Amer. Geophys. Union*, *65*, 1077, 1984a.
- Olsson, W. A., A dislocation model of the stress history dependence of frictional slip, *J. Geophys. Res.*, *89*, 9271-9280, 1984b.
- Olsson, W. A., A constitutive model for frictional slip on rock interfaces, *Mechanics of Materials*, *3*, 295-299, 1984c.
- Olsson, W. A., Normal stress history effects on friction in tuff, *EOS, Trans. Amer. Geophys. Union* *66*, No. 46, 1101, 1985.
- Olsson, W. A., The effects of changes in normal stress on rock friction, in *Constitutive Laws for Engineering Materials, Theory and Applications* eds., C. S. Desai, E. Krempl, P. D. Kioussis, and T. Kundu, Elsevier, New York, 1059-1066, 1987.
- Plesha, M. E., Constitutive modeling of rock joints with dilation, in *26th U. S. Symposium on Rock Mechanics*, ed. E. Ashworth, Balkema, Boston, 1985.
- Prager, W., and P. G. Hodge, Jr., *Theory of Perfectly Plastic Solids*, Chap. 3, Dover, New York, 1951.
- Rice, J. R. and A. L. Ruina, Stability of steady frictional slipping, *J. Appl. Mech.*, *50*, 343-349, 1983.
- Rosso, S., Comparison of joint stiffness measurements in direct shear, triaxial compression, and *in situ*, *Int. J. Rock Mech. Min. Sci.*, *13*, 167-172, 1976.
- Ruina, A., Slip instability and state variable friction laws, *J. Geophys. Res.*, *88*, 10,359-10,370, 1983.

- Schwartz, B. M., Unclassified internal memorandum to S. J. Bauer (Org. 6314), Sandia National Laboratories, June 7, 1984.
- Smith, J. O., and O. M. Sidebottom, *Elementary Mechanics of Deformable Bodies*, Chap. 9, Macmillan, Toronto, 1969.
- Smith, T. L., Linear viscoelastic response to a deformation at constant rate: derivation of physical properties of a densely crosslinked elastomer, *Trans. Soc. Rheol.*, 20 103-117, 1976.
- Soldberg, P., and J. D. Byerlee, A note on the rate sensitivity of frictional sliding of Westerly Granite, *J. Geophys. Res.*, 89, 4203-4205, 1984.
- Sun, Z., C. Gerrard, and O. Stephansson, Rock joint compliance tests for compression and shear loads, *Int. J. Rock Mech. Min. Sci. & Geomech. Abstr.*, 22, 197-213, 1985.
- Teufel, L. W., Frictional properties of jointed welded tuff, *SAND81-0212*, Sandia National Laboratories, Albuquerque, NM, 1981.
- Thomas, R. K., A continuum description for jointed media, *Sandia Lab. Tech. Rep.*, *SAND81-2615*, 1982.
- Timoshenko, S. P., and J. N. Goodier, *Theory of Elasticity*, Art. 101, Third Edition, McGraw-Hill, New York, 1970.
- Walsh, J. B., Mechanics of strike-slip faulting with friction, *J. Geophys. Res.*, 73, 761-776, 1968.
- Weeks, J. D., and T. E. Tullis, Frictional behavior of dolomite, *EOS Trans. Am. Geophys. Union*, 45, 1077, 1984.
- Weertman, J., Continuum distribution of dislocations on faults with finite friction, *Bull. Seismol. Soc. Am.*, 54, 1035-1058, 1964.

Appendix A

Theoretical Model

A.1 Torque-Stress Relations

Consider a right-circular cylinder of rock containing a planar cut perpendicular to the axis. For definiteness, take the cut to be near the midpoint of the axis. The cylindrical sample is subjected to a constant compressive load along the axis and a time-varying torque about the axis. These boundary loads cause a normal stress to act across the central cut and a shear stress to act perpendicularly to the radii in the plane of the cut. Erect a right-handed coordinate system with the origin at the outer edge of the circular cut. Let the z -axis coincide with a generatrix of the circularly cylindrical, outer sample surface, and let the x -axis point toward the center of the cut. Thus, the y -axis is tangent to the surface of the cylinder.

The shear stress, τ_{∞} , due to the remotely applied torque varies linearly from zero at the center to a maximum value at the outer edge of the cut [e.g., *Smith and Sidebottom*, 1969; *Timoshenko and Goodier*, 1970]. For the case of a hollow cylinder of inner and outer radii R_i and R , respectively, the stress on the test surface due to the applied torque is

$$\tau_{\infty}(x) = \frac{T}{J}(R - |x|), \quad (A.1)$$

where $J = \pi(R^4 - R_i^4)/2$ is the polar moment of inertia and T is the torque. The absolute value is taken because in a later section, an image dislocation solution is used; for this the symmetry in stress is needed.

At any radius the condition for the onset of slip is that the applied stress, τ_{∞} , plus the internal stress, τ_i , due to prior slip just equals the uniform friction stress, τ_f , such that

$$\tau_{\infty} + \tau_i = \tau_f. \quad (A.2)$$

Substituting (A.1) into (A.2) yields

$$\tau_i = \left(\tau_f - \frac{T}{J}R\right) + \frac{T}{J}|x|. \quad (A.3)$$

Because the shear stress is greatest at the outer edge, slip will begin there and will spread into the interior, up the stress gradient given by $\tau_f - \tau_\infty$, as the torque is monotonically increased. In this problem, the stress is known within the slipping zone; it is equal to the friction stress. Outside the slipping zone, the slip is everywhere zero. Thus, this is a mixed boundary value problem to which the solution can be found if it is assumed that the depth of slip is small with respect to the radius of the circular cut. In effect, a two-dimensional, anti-plane strain approximation is used. Figure 1 shows the relationships amongst the shear stress components over the test surface; τ_∞ is computed below.

A.2 Torque-Slip Relations

The relationships between the torque and the magnitude and distribution of offset in the slipping zone is derived using a continuum dislocation model. As noted previously [Weertman, 1964; Olsson, 1984], the idea of a distribution of dislocations in a problem with continuous displacements is merely a physical device to aid visualization. To treat the problem two-dimensionally, assume that the xy -plane of the coordinate system coincides with the interface separating two linear elastic half-spaces pressed together by a uniform normal stress, σ_n . If infinitely long, straight, screw dislocations parallel to y having infinitesimal Burgers vectors are distributed antisymmetrically about the origin; positive ones along the $+x$ -axis, and negative ones along the $-x$ -axis—in the image space; the yz -plane will be stress free and therefore may be taken as a free surface. Now, when the local stress at the origin becomes equal to the friction stress, screw dislocations nucleate there and move into the positive half-space to the depth d and into the image half-space to the depth $-d$. Because the yz -plane is stress free, the half-space $x \geq 0$ can be considered a good representation of the cylindrical problem for $d \ll R$. This is the same reasoning that makes it possible to model a strike-slip fault on the earth's curved surface as a shallow, long fault in a half-space.

Define the dislocation density function, $B(x)$, such that $B(x) dx$ is the total offset between x and $x + dx$. The slip, $D(x)$, is given by $dD(x)/dx = -B(x)$. Because it is a displacement gradient, $B(x)$ is evidently a strain measure. The shear stress, $\tau_i(x_0)$, at x_0 due to a unit dislocation lying at x is $(G/2\pi)/(x - x_0)$. Superposing the stress due to the distribution of dislocations gives

$$\tau_i(x_0) = \frac{G}{2\pi} \int_{-\infty}^{\infty} \frac{B(x) dx}{x - x_0}, \quad (A.4)$$

where G is the shear modulus. In a general sense, $\tau_i(x_0)$ can be thought of as the stress change on a fault due to the slip [Mavko, 1981]. Because $B(x)$ is not known on $(-d, d) \subset (-\infty, \infty)$ but τ_i is, equation (A.4) is an integral equation for the determination of $B(x)$ and can be inverted by the method of Muskhelishvili [1953]. At the ends of the slipping zone the stress is bounded by the friction stress so that the solution for bounded $B(x)$ is appropriate. Therefore

$$B(x_0) = \frac{2}{\pi G} (d^2 - x_0^2)^{1/2} \int_{-d}^d \frac{\tau_i(x) dx}{(d^2 - x^2)^{1/2} (x - x_0)}. \quad (\text{A.5})$$

The existence of equation (A.5) requires that

$$\int_{-d}^d \frac{\tau_i(x) dx}{(d^2 - x^2)^{1/2}} = 0. \quad (\text{A.6})$$

Integration of (A.6), with $\tau_i(x)$ from (A.3), gives

$$\hat{T} = \frac{1}{1 - 2d/\pi R} = 1 + \frac{2d}{\pi R} + o(d^2) \quad (d \rightarrow 0) \quad (\text{A.7})$$

for the relationship between slip zone depth, d/R , and the nondimensional torque, $\hat{T} = TR/\tau_f J$. The analysis in this paper is necessarily limited to small values of d , and thus terms in (A.7) of order less than two are dominant. For the limiting case of $d \rightarrow 0$, the excess torque, that is, the torque greater than that needed to just initiate slip, $\hat{T} - 1$, is linear in the slip zone depth just as in the plane strain case [Olsson, 1984]. Also, with the appropriate identification of the variables, equation (A.7) agrees with the depth of faulting found by Walsh [1964].

$B(x)$ and $\tau_i(x)$ are Hilbert transforms of each other [Weertman, 1964; Mavko, 1982], which makes computation easy for the stress distribution given by (A.3) because the appropriate transform is tabulated in Erdelyi et al. [1954]. Using (A.3) and taking the transform as in (A.5) gives

$$B(x) = \frac{4\tau_f}{\pi GR} \left(\frac{1}{1 - 2d/\pi R} \right) x \log \left| \frac{d + (d^2 - x^2)^{1/2}}{x} \right|. \quad (\text{A.8})$$

Note that in two-dimensional, plane strain, slippage problems described by edge dislocations, a similar form for $B(x)$ arises [Weertman, 1964; Olsson, 1984], but the collection of factors in front of the log term does not contain the slip zone depth as it does here. This is because in that problem, the applied stress was uniform and the friction varied linearly. Here the reverse is true; the friction is uniform, and the applied stress varies. Thus, as the torque increases, the stress gradient steepens, causing a greater increase in the amplitude of $B(x)$ for a given deepening of the slip zone. An equation with structure similar to (A.8) was derived by Leonov and Shvaiko [1961] for torsion of an

elastic-plastic cylinder. In that problem the plastic strain is distributed throughout an annular shell, whereas in the present problem, the plastic strain (slip) is confined to a planar annular disk.

Recalling that $B(x) = -dD(x)/dx$, the slip in terms of the dislocation density distribution function can be written

$$D(x) = \int_x^d B(\xi) d\xi. \quad (\text{A.9})$$

Substitution of (A.8) into (A.9) and integrating results in

$$D(x) = \frac{2\tau_f}{\pi GR} \left(\frac{1}{1 - 2d/\pi R} \right) \left[d(d^2 - x^2)^{1/2} - x^2 \operatorname{sech}^{-1}(x/d) \right] \quad (\text{A.10})$$

for the slip profile along x .

At the outer surface, where the slip can be measured experimentally, we obtain the relation

$$\frac{\pi G}{2\tau_f R} D_0 = \left(\frac{d}{R} \right)^2 \left(\frac{1}{1 - 2d/\pi R} \right), \quad (\text{A.11})$$

where $D(0)$ has been replaced by D_0 and is called the offset. This equation has the same form as that derived by *Walsh* [1968] for vertical strike slip faults. Equations (A.7) and (A.11) combine to give the parametric form of the torque-*versus*-offset relationship for first loading in rotary shear. Relationships for unloading and subsequent reloading are derived below. In the plane strain (direct shear) configuration, D_0 was found to be proportional to d^2 [*Olsson*, 1984], and therefore in the small d limit, the solutions are the same.

Unloading is accomplished by adding an additional torque, $-\hat{T}^u$ ($\hat{T}^u \geq 0$), to the maximum value of \hat{T} achieved during loading, \hat{T}' , so that $\hat{T} = \hat{T}' - \hat{T}^u$. When $\hat{T}^u = \hat{T}'$, unloading is complete. In terms of shear stress on the surface during reverse slipping,

$$\tau_i(x) = -2\tau_f + \tau_\infty^u. \quad (\text{A.12})$$

When the applied torque is reversed, the maximum shear stress again occurs at the outside of the circular cut, but the sign is reversed, causing negative screw dislocations to nucleate there and move into the interior, consuming positive dislocations as they go. By use of (A.6), the relationship between depth of reverse slip d^u/R and \hat{T}^u is found to be

$$\hat{T}^u = \frac{2}{1 - 2d^u/\pi R} \approx 2 \left(1 + \frac{2d^u}{\pi R} \right). \quad (\text{A.13})$$

Application of (A.5), (A.6), and (A.10) gives the rest of the unloading equations:

$$B^u(x) = -\frac{4\tau_f}{\pi GR} \left(\frac{2}{1 - 2d^u/\pi R} \right) x \log \left| \frac{d^u + (d^{u2} - x^2)^{1/2}}{x} \right|, \quad (\text{A.14})$$

and

$$\frac{\pi G}{2\tau_f R} D_0^u = - \left(\frac{d^u}{R} \right)^2 \left(\frac{2}{1 - 2d^u/\pi R} \right). \quad (\text{A.15})$$

Reloading may be realized by adding a torque, \hat{T}^r , to the minimum torque attained during unloading, $\hat{T}^{u'}$. By methods similar to those above, the reloading equations are:

$$T^r = \frac{2}{1 - 2d^r/\pi R} \approx 2 \left(1 + \frac{2d^r}{\pi R} \right), \quad (\text{A.16})$$

$$B^r(x) = \frac{4\tau_f}{\pi GR} \left(\frac{2}{1 - 2d^r/\pi R} \right) x \log \left| \frac{d^r + (d^{r2} - x^2)^{1/2}}{x} \right|, \quad (\text{A.17})$$

and

$$\frac{\pi G}{2\tau_f R} D_0^r = \left(\frac{d^r}{R} \right)^2 \left(\frac{2}{1 - 2d^r/\pi R} \right). \quad (\text{A.18})$$

Further loading and unloading cycles are described by equations (A.16) and (A.18), and (A.13) and (A.15), respectively. Thus, after the first torquing phase, oscillations in torque between fixed limits produce identical torque-offset loops. A similar result has been found for a direct shear configuration [Olsson, 1984] and for contacting spheres suffering oscillating, oblique loads [Mindlin and Deresiewicz, 1953].

A.3 Model Response

A calculated \hat{T} versus D_0 curve for a period of torquing followed by untorquing, reverse torquing, and then retorquing is shown in Figure A2. As \hat{T} is increased (at constant normal stress) from zero, no slip occurs until the applied stress at the outer edge of the sample surface equals the friction stress. At *A*, this condition is met and slip ensues, as indicated by D_0 taking on nonzero values. As the torque is further increased, there is a gradual increase in D_0 until torquing is reversed (*B*, Figure A2). The sliding surface sticks together until the torque is reversed to a value given by (13) (*C*, Figure A2), at which time reverse slip begins at the outer radius. At *D*, retorquing is first accompanied by sticking (*DE*, Fig. A2), then slip development along *EB*. With no surface property evolution accounted for in this simplified model, the torque assumes

the same level at B as during the first torquing. Again, this response is similar to plane-strain slippage [Olsson,1984] and to slippage at the contact of two spheres [Mindlin and Deresiewicz, 1953].

During the loading phase, the slip profile develops progressively, as shown in Figure A3. The increasing torque causes the continuing injection of new dislocations from the surface leading to progressive deepening of the slip zone as given by d , which is measured indirectly in experiments by D_0 . These slip profiles are similar to one heterogeneous fault model discussed by *Mavko* [1981]. Reversing sufficiently the sense of the torquing causes reverse slip to begin at the outer edge and to propagate into the sample. The development of the net slip profile during reverse torquing is illustrated in Figure A4. At the end of the torquing phase, the slip distribution is given by curve $ABCD$ (Fig. A4). During reverse torquing, $D(x)$ moves through successive distributions $EBCD$, FCD , and, finally, GD . During this process slip does not everywhere vanish at any torque. In fact, even after such a simple stress history as that applied in this example, the slip is quite complex.

Figure A5 depicts the evolution of the slip distribution for the three-part torque history shown in Figure A2 comprised of torquing to $\hat{T} = 1.2$, then reverse torquing to $\hat{T} = -1.2$, and then retorquing to $\hat{T} = 1.2$. The slip profile resulting from torquing to 1.2 (B , Fig. A2) is shown by ABC in Figure A5. Untorquing to -1.2 results in profile FGC (Fig. A5). Final retorquing to 1.2 (D to B in Figure A2) results in profile ABC again. Intermediate profiles are shown as EBC and DGC for reverse torquing and retorquing, respectively. When the retorquing profile coincides with the original torquing one, the current T, D_0 state coincides with the one passed through on the first loading. This is a reflection of the phenomenon of discrete memory [e.g., *Hueckel and Nova*, 1979], as was found earlier for plane-strain conditions [Olsson, 1984]. It is simply the result of the slip distribution returning to an earlier state. If torquing were to continue, the torque-slip curve would extend along the path of the original one.

A particularly important feature of slipping interfaces that are characterized by a nonuniform driving stress emerges in these figures (Figs. A3, A4, A5). If nonuniform slip occurs upon torquing, unloading to zero torque will not return the shear stress on the interface to zero anywhere. Further, reverse torquing to induce negative slip will, in general, not lead to uniformly zero slip and hence zero shear stress. It is concluded that once subjected to sufficient torque to cause slip, the interface will only under very special circumstances ever again be everywhere shear stress-free. These special circumstances include the vanishing of the normal stress, at least momentarily, and creep processes that are not included in this model. In the next section, one more process will be shown to return the interface to zero slip, uniformly.

A.4 *Returning the Interface to Uniformly Zero Shear Stress*

Study of Figure A5 suggests that a sufficiently large number of alternating slips of monotonically decreasing magnitudes would return the interface to as near to zero slip everywhere as desired. For convenience, $\hat{D}(\cdot) = (\pi GR/2\tau_f)D(\cdot)$. Clearly, after k alternating torquings into the slipping regime, the net displacement, $\hat{D}_k^{net}(x)$, is given by

$$\hat{D}_k^{net}(x) = \hat{D}_1(x) + \sum_{n=2}^k \hat{D}_n(x), \quad (\text{A.19})$$

where

$$\begin{aligned} \hat{D}_1(x) &= \left(\frac{1}{1-2d_1/\pi R} \right) \left[d_1(d_1^2 - x^2)^{1/2} - x^2 \text{sech}^{-1}(x/d_1) \right] \\ \hat{D}_n(x) &= (-1)^n \left(\frac{2}{1-2d_n/\pi R} \right) \left[d_n(d_n^2 - x^2)^{1/2} - x^2 \text{sech}^{-1}(x/d_n) \right] \end{aligned}$$

and n numbers the alternating torquings sequentially from $n = 1$, the first torquing, to a maximum of k . Thus $n = 2$ is the first reverse torquing, $n = 3$ is the first retorquing, $n = 4$ is the second reverse torquing, and so on. Because (A.19) is an alternating series

$$\lim_{k \rightarrow \infty} \sum_{n=1}^k \hat{D}_n^{net}(x) = L \quad (\text{A.20})$$

if only we make $d_n \geq d_{n+1}$ and $\lim_{n \rightarrow \infty} \hat{D}_n(x) = 0$. That the sum L is actually zero is established by inspection of Figure A5. Thus, an infinite number of alternating torquings of decreasing amplitude will in the limit return the interface to uniformly zero slip, which results in uniformly zero shear stress.

A practical implication of this result is that many-cycle, low-amplitude stressing, such as the diurnal tides, could play a role in destressing the inhomogeneously deformed joints, faults, and bedding planes existing in any rock mass.

A.5 *The Shear Stress in the Slip Plane During Slip Establishment*

At the very onset of slip, the stress on the joint is given by (3.2). After complete spread of slip over the entire joint, the shear stress, τ_{fs} , is given by equation (3.3). During the time that slip is spreading across the sliding interface, the stress is more

complex. Here, the stress profile for shallow slip is computed; deep slip is probably qualitatively similar, but that problem remains to be solved.

After tangential slip begins to spread across the joint so that the cross section is divided into a slipping and a sticking region, the stress due to the inhomogeneous slip is given by (A.4) using $B(x)$, as found in (A.8). Thus, the problem is reduced to the evaluation of

$$\frac{\pi R}{2i\tau_f \hat{T}} \tau_i(x_0) = \frac{1}{2\pi i} \oint x \log \left| \frac{d + (d^2 - x^2)^{1/2}}{x} \right| \frac{dx}{(x - x_0)}. \quad (A.21)$$

This integral is most simply computed using Cauchy's integral formula for the region outside the slipping zone. One arrives at

$$\tau_i(x_0) = \frac{2\tau_f \hat{T}}{\pi R} \left[x \arcsin \frac{d}{x} - d \right] \quad (A.22)$$

for the internal stress outside $[-d, d]$. The internal stress within the slipped zone is given by (A.3). Figure A1 shows the relationships amongst the three shear stress components τ_∞ , τ_f , and τ_i .

Appendix B

FIGURES

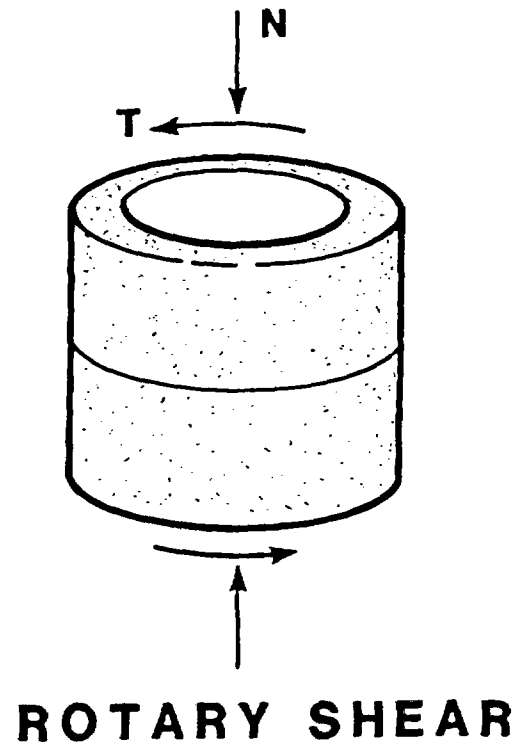
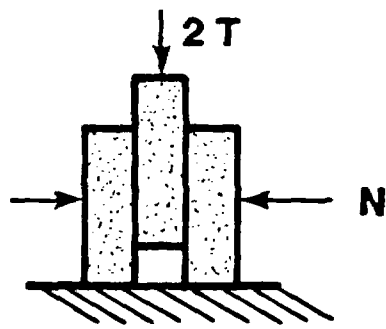
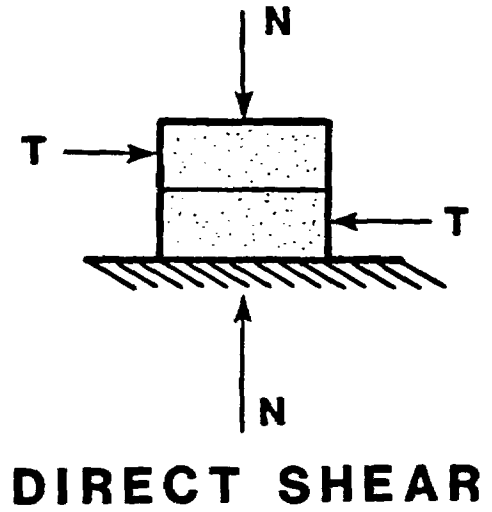
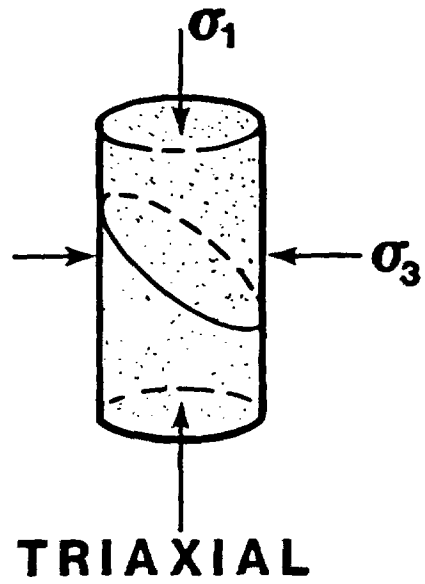


Figure 1. Various test configurations for determining frictional response of sliding surfaces and the usual measurements.

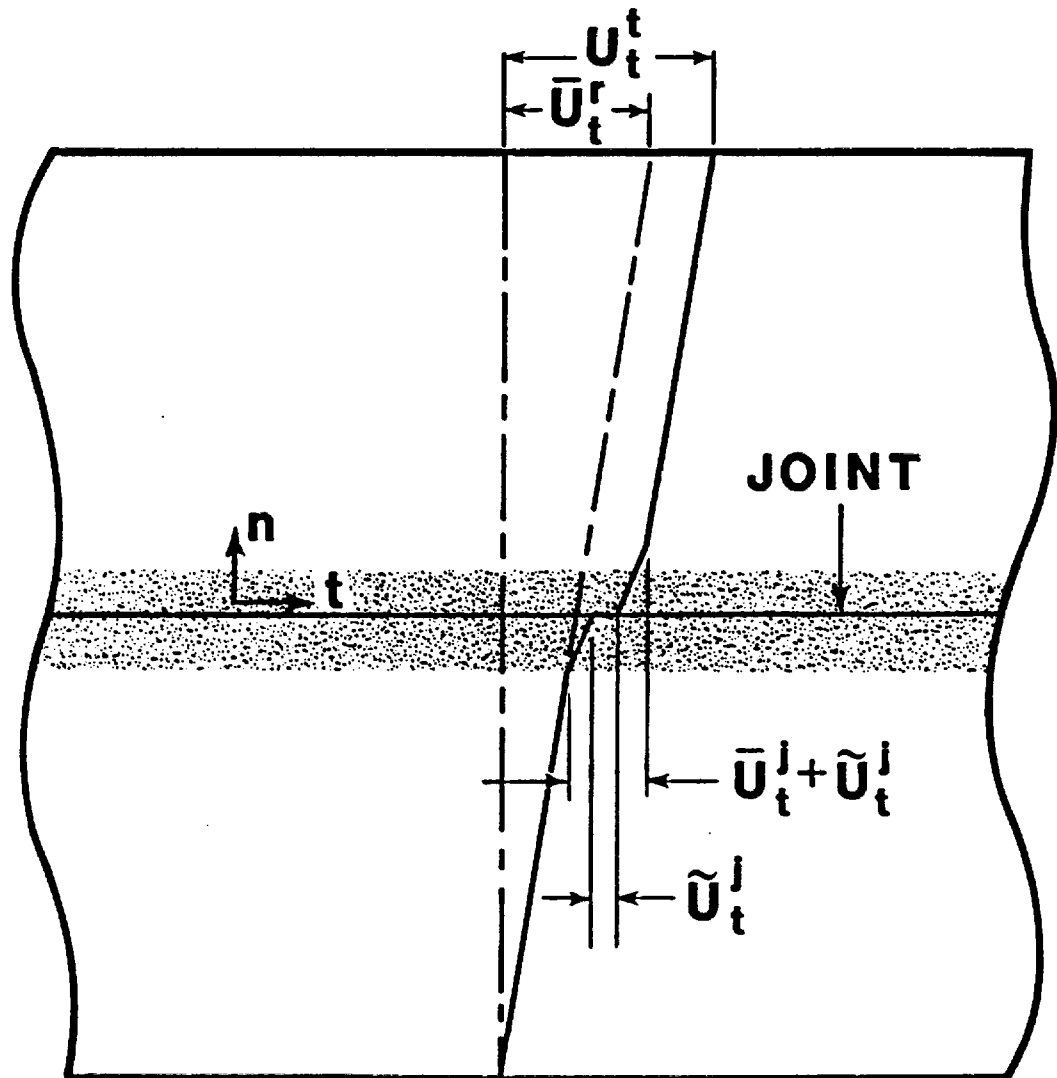


Figure 2. Definition of the various displacements that can be measured on a fractured sample.

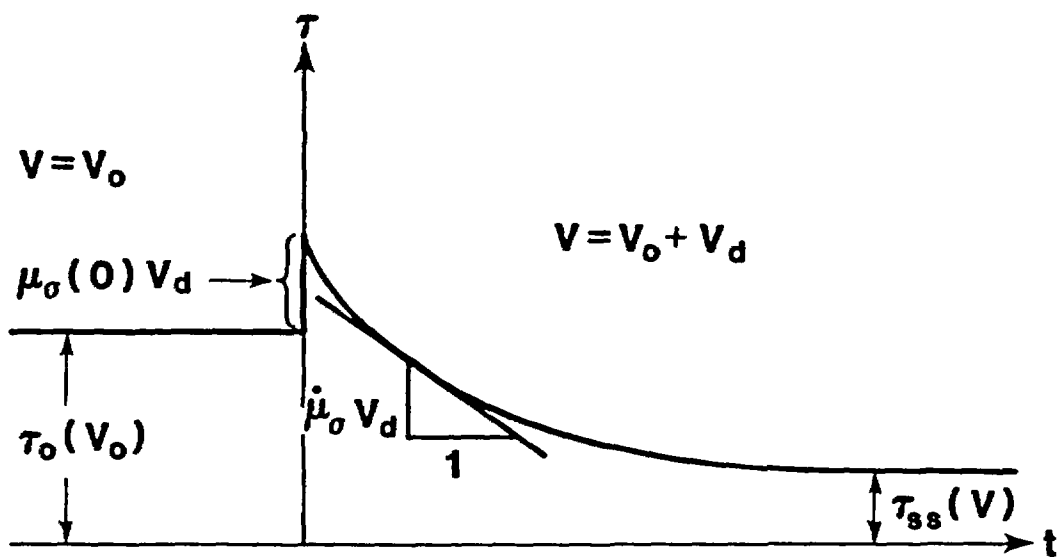


Figure 3. Definition sketch for velocity step tests.

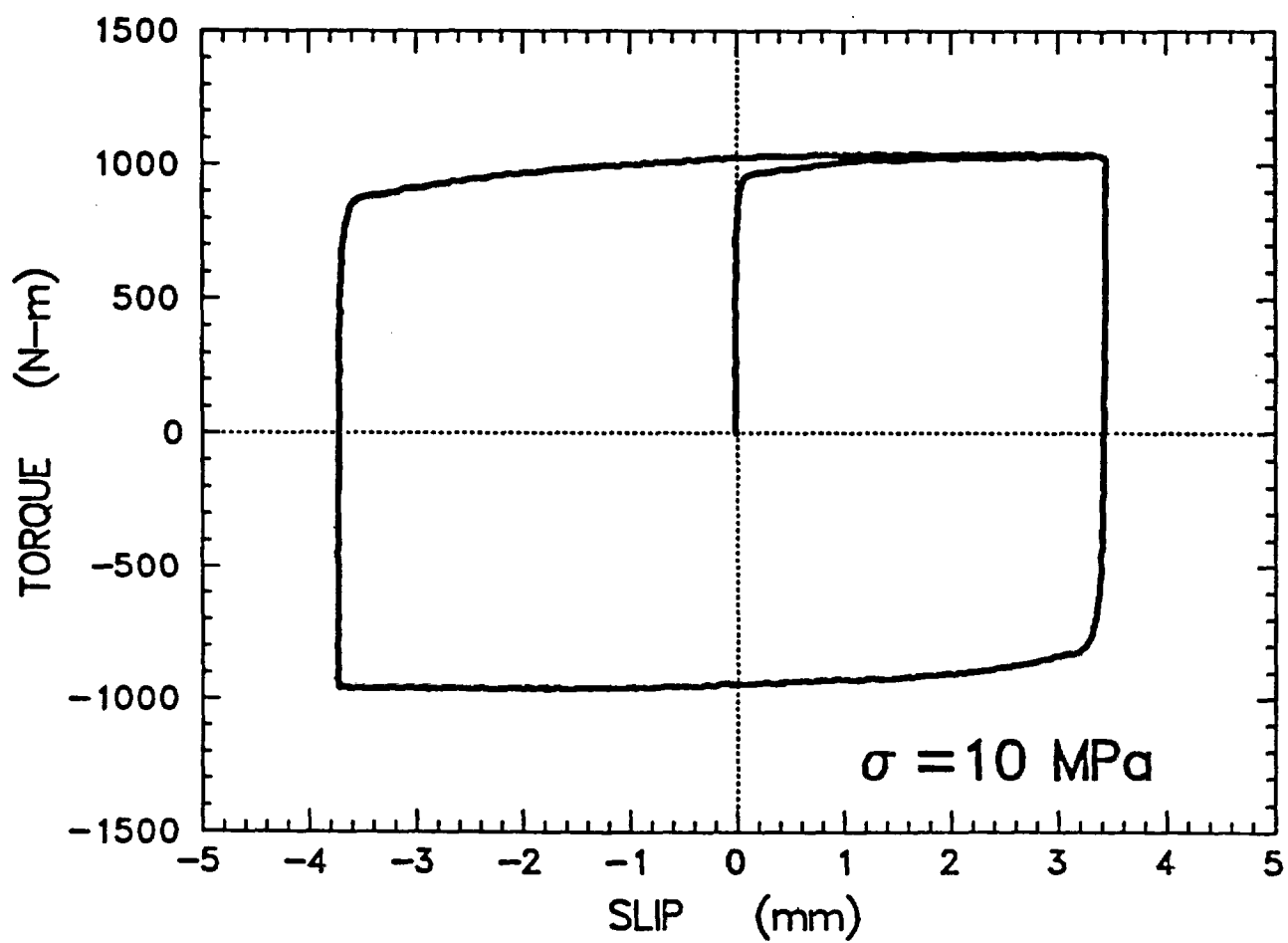


Figure 4. Torque-slip loop for Westerly granite at 10 MPa normal stress.

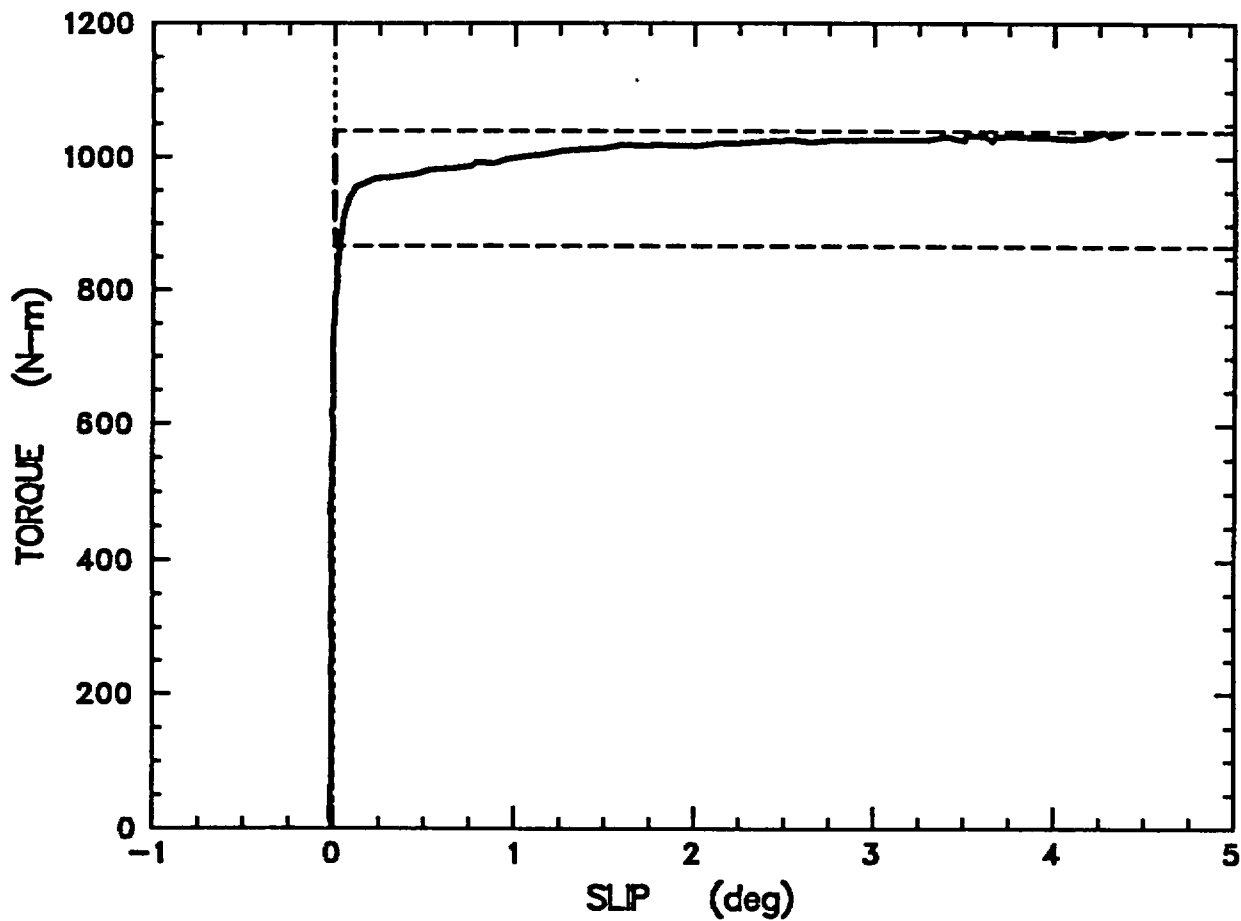


Figure 5. Enlargement of the first loading portion of test shown in Figure 4 (solid line). T_{fs} is taken as the maximum, steady value, and this is used to compute T_o . A calculated torque-slip curve is also plotted here using the data (dashed line); it is indistinguishable, at this scale, from the torque axis.

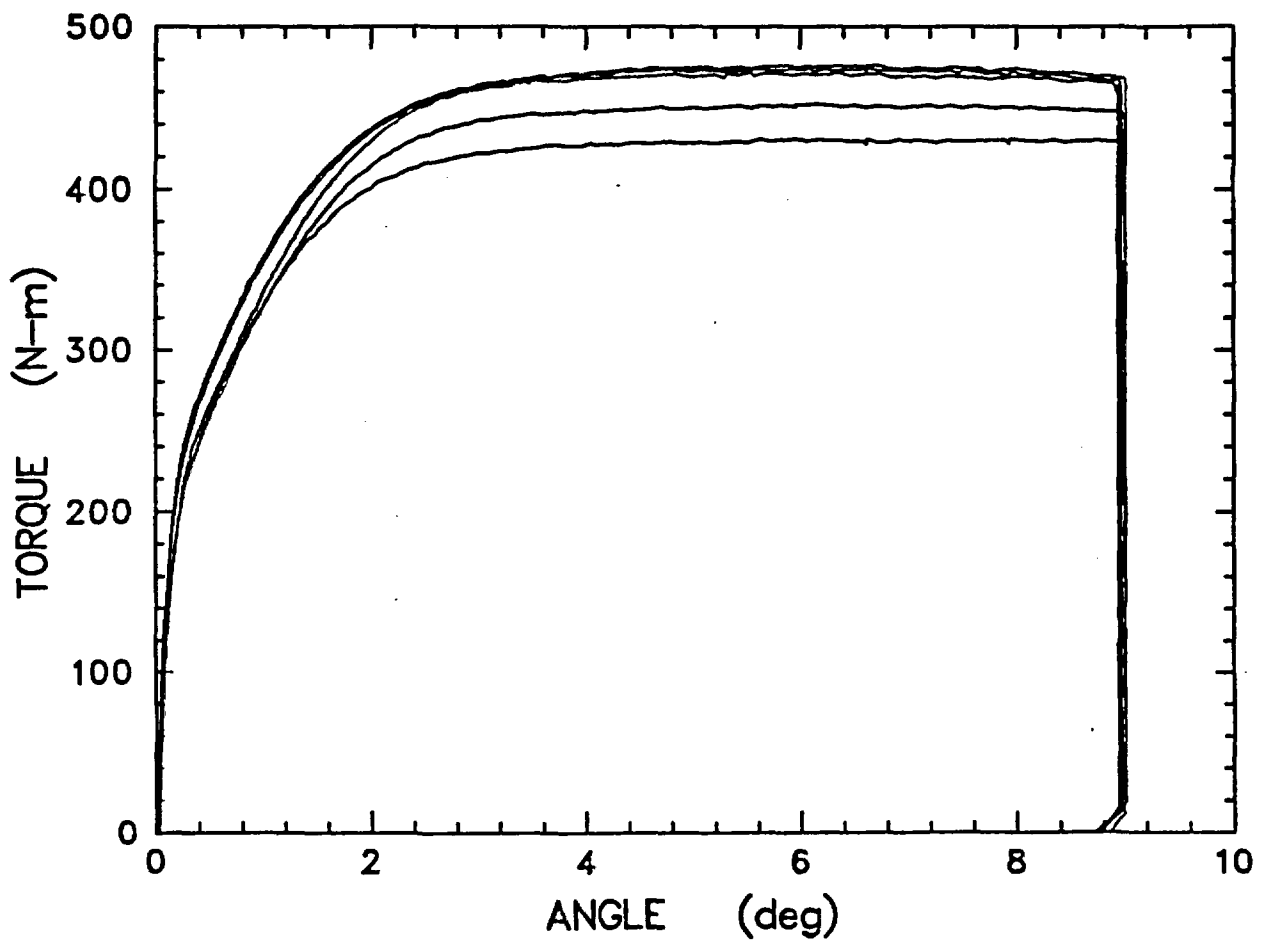


Figure 6. Approach to steady-state friction with continuing slip. The first three successive tests are progressively higher, and the fourth and fifth are the same as the third (Experiment RFT058).

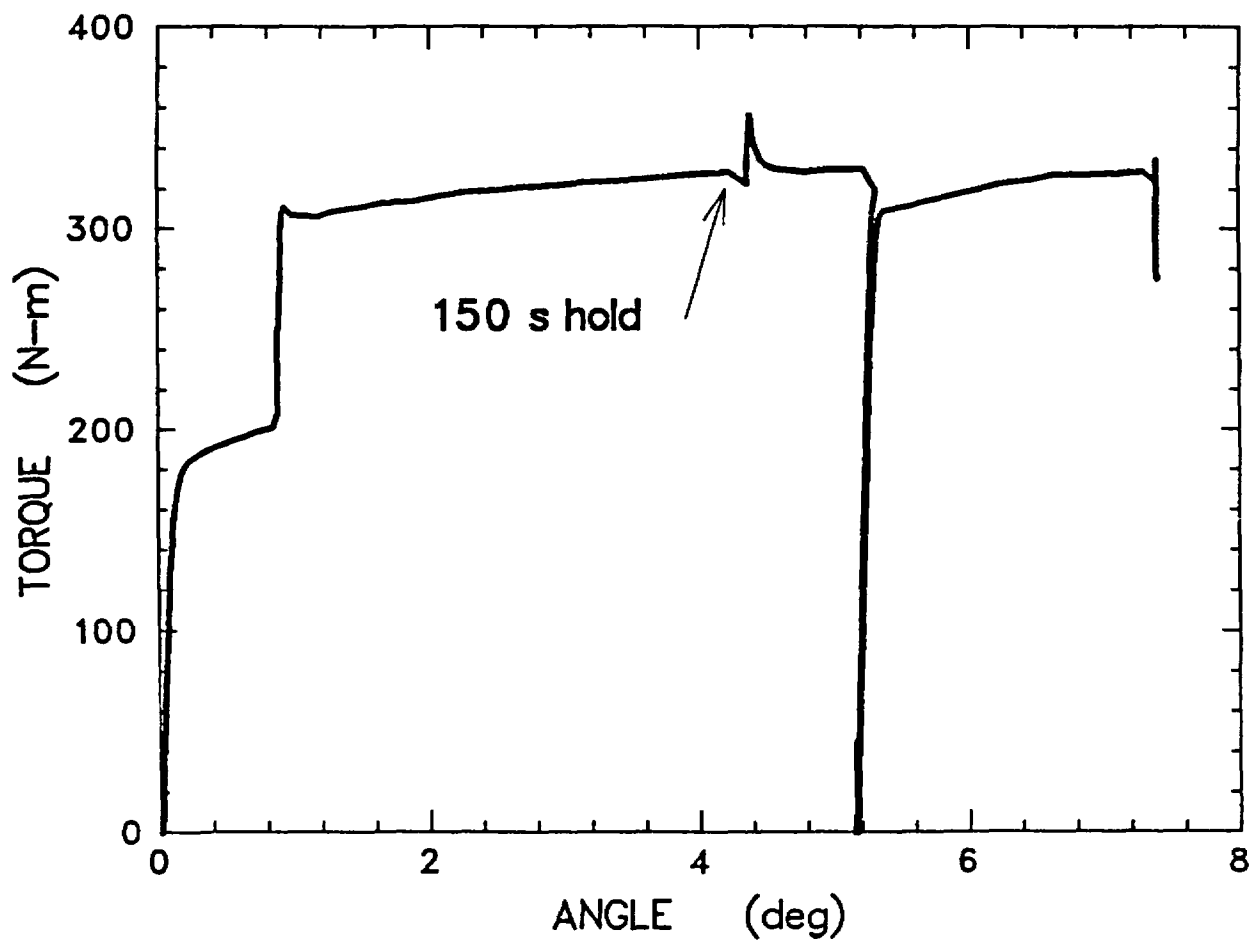


Figure 7. The effect of stopping the sliding for a period of 150 seconds (Experiment RFT026).

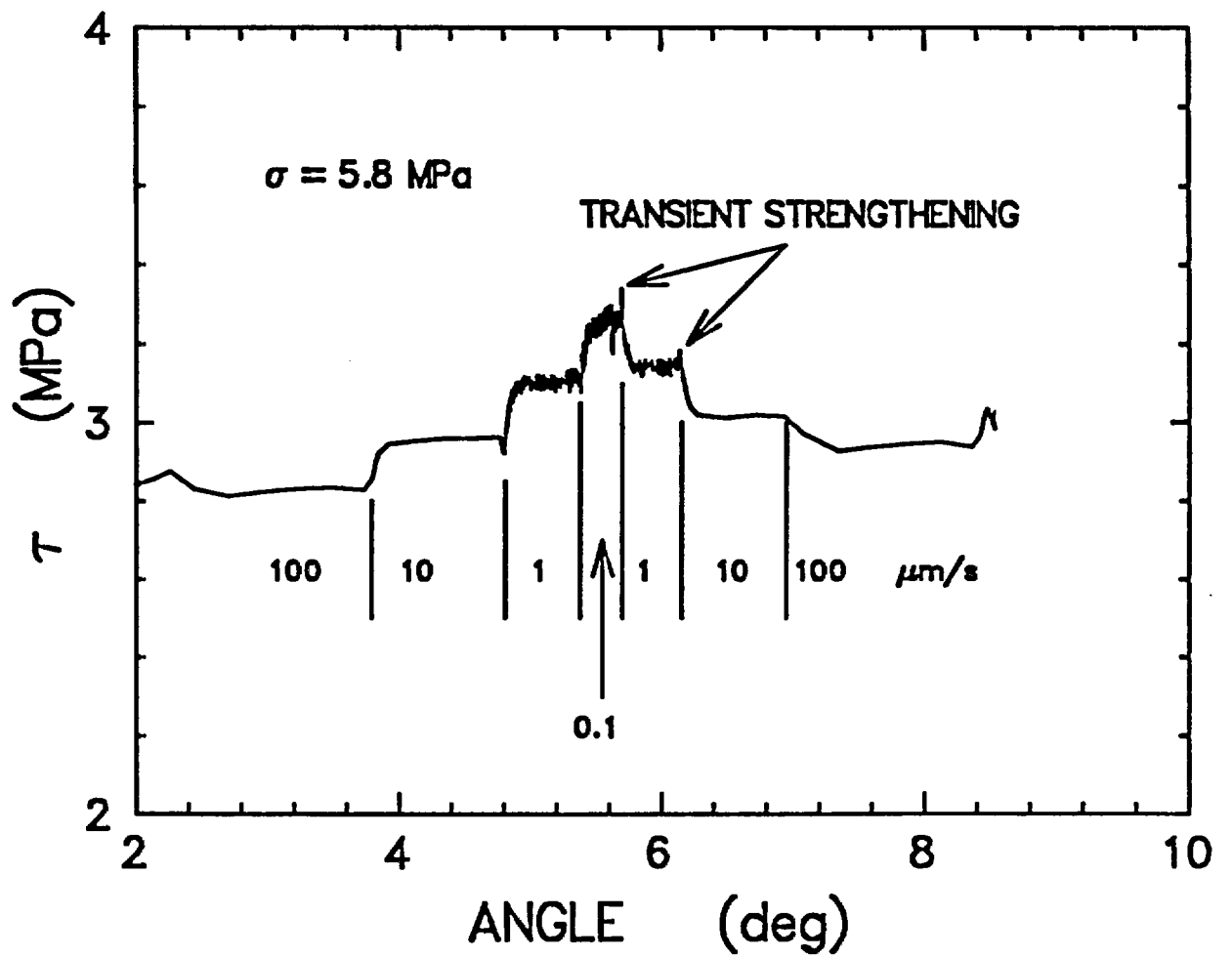


Figure 8. The effect of stepping the velocity on the friction stress for Topopah Spring tuff (Experiment RFT028).

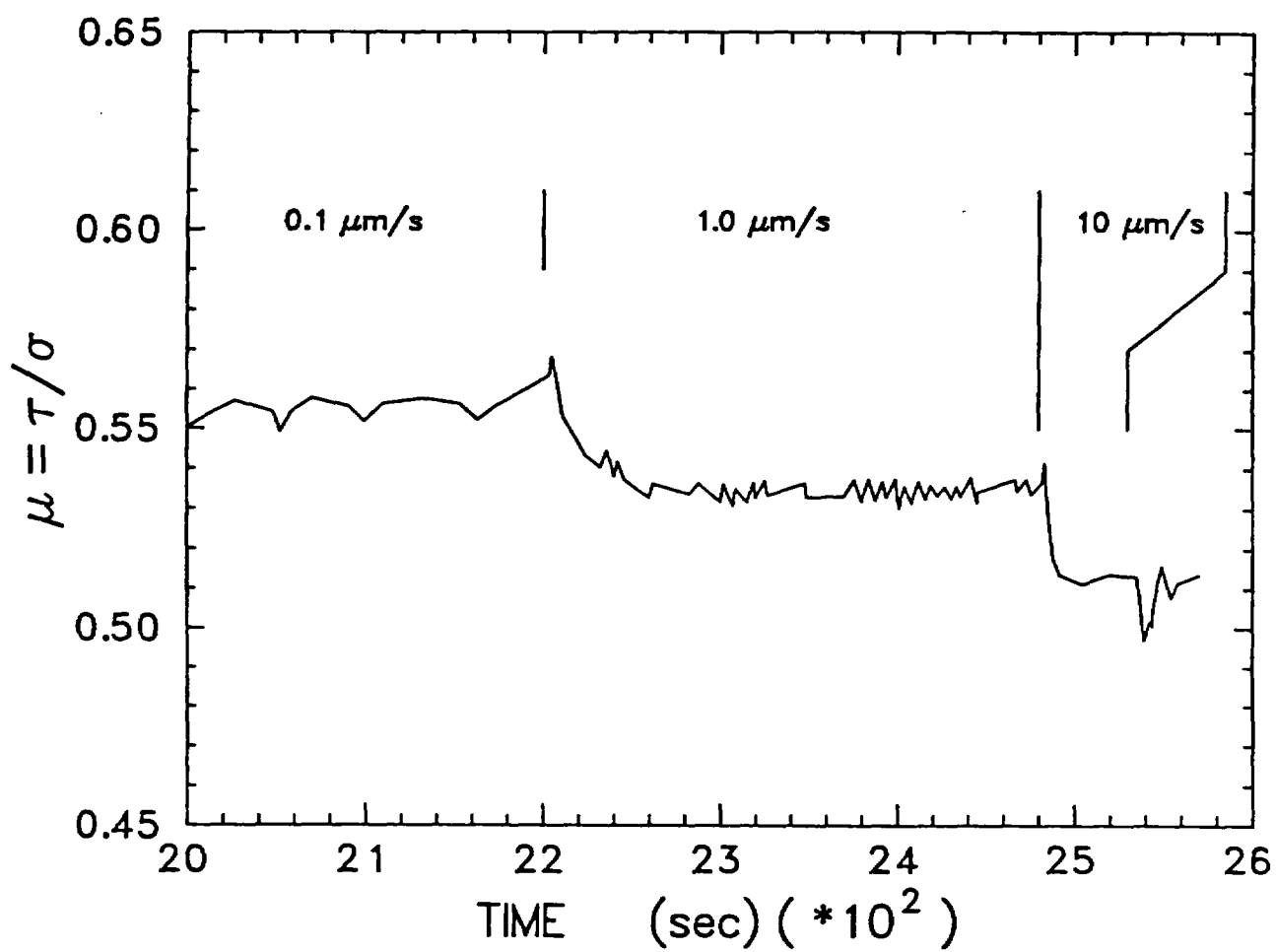


Figure 9. Enlargement of Figure 8 with the shear stress divided by the normal stress (Experiment RFT028).

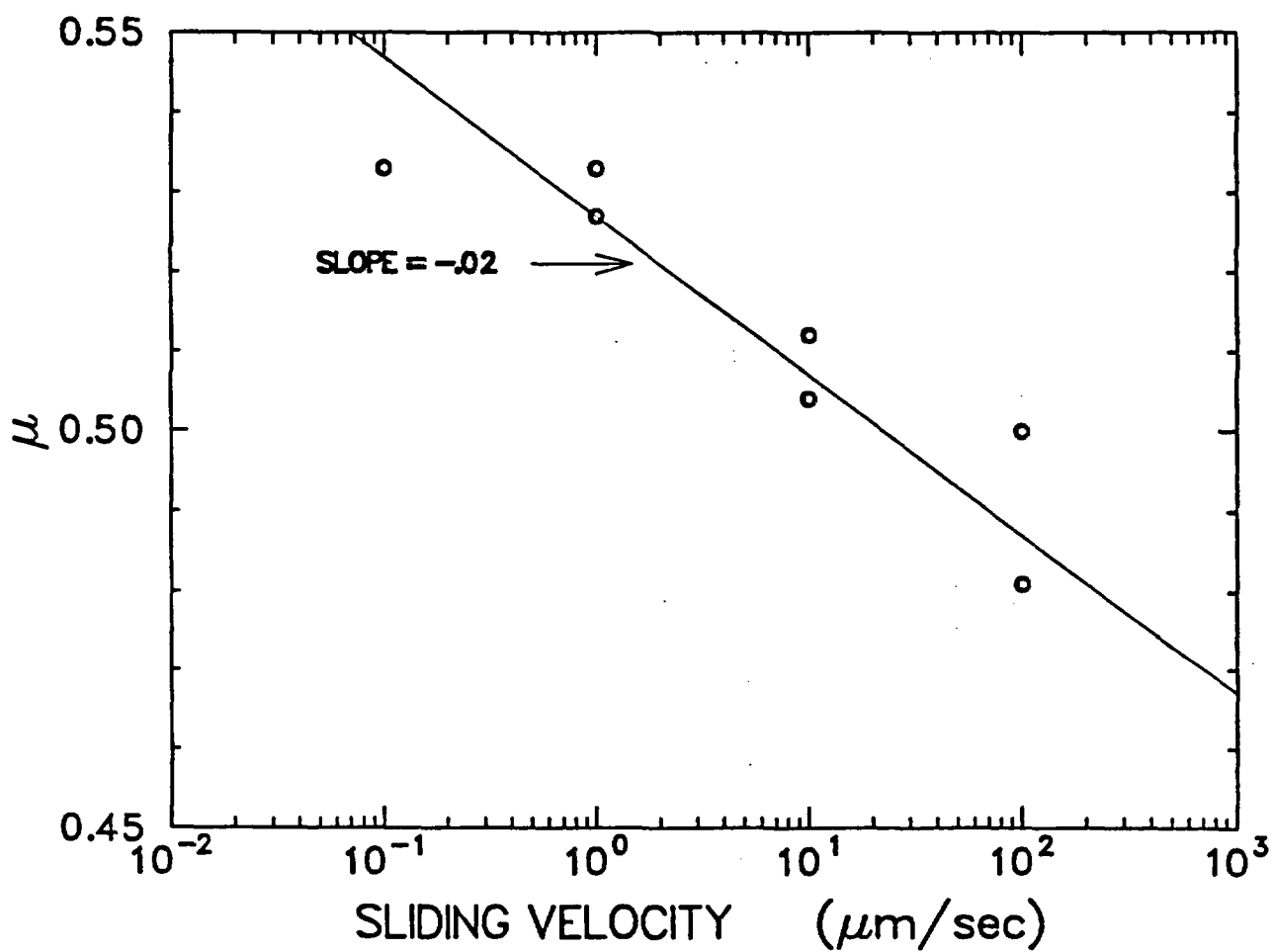


Figure 10. The steady-state coefficient of friction plotted against log sliding velocity for test RFT028 shown in 8 and 9.

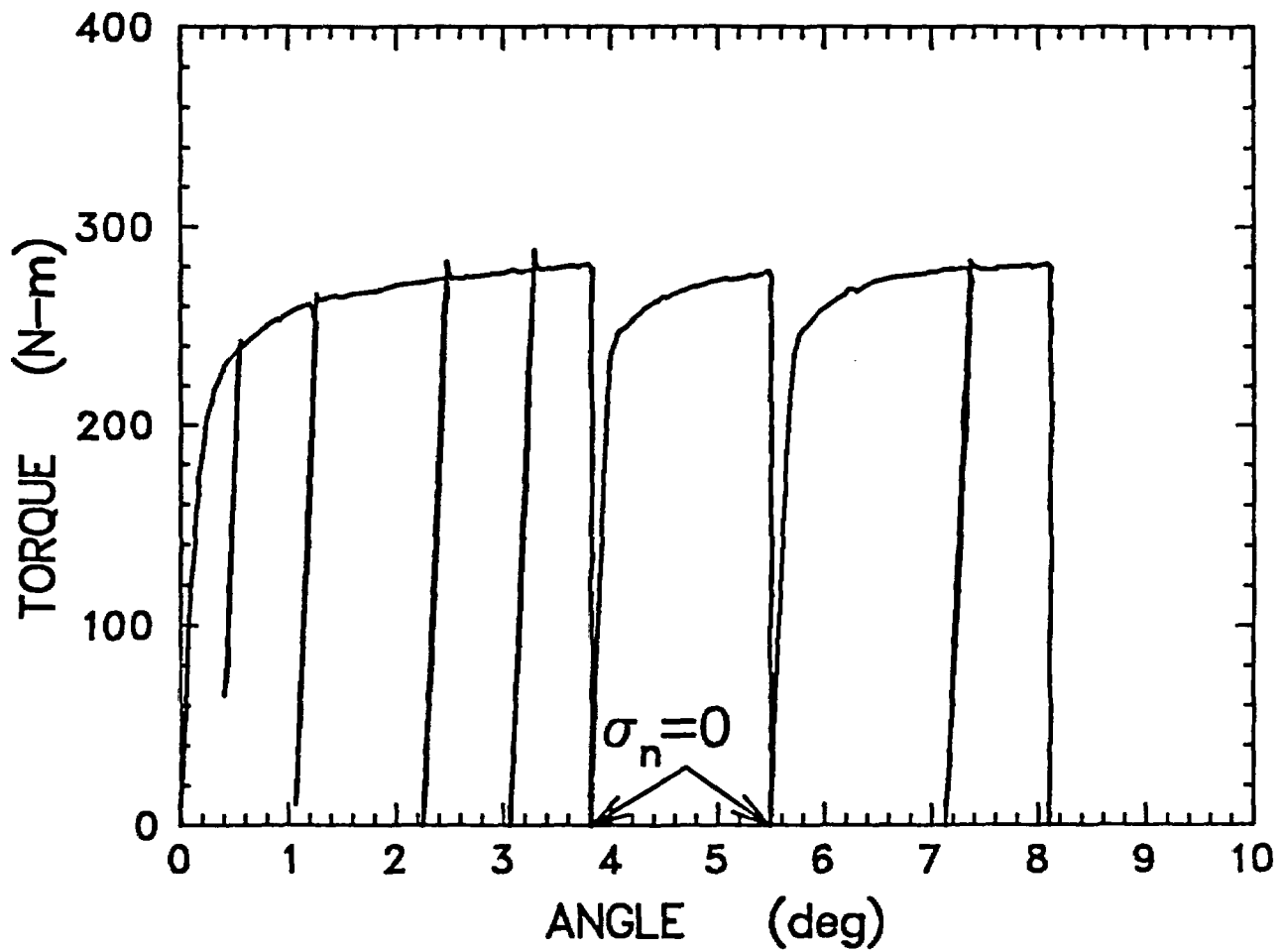


Figure 11. The effect of cycling the torque while maintaining the normal stress constant at 3 MPa (cycles 1 through 4) and with intervening removals of normal stress (cycles 5 and 6)(Experiment RFT030).

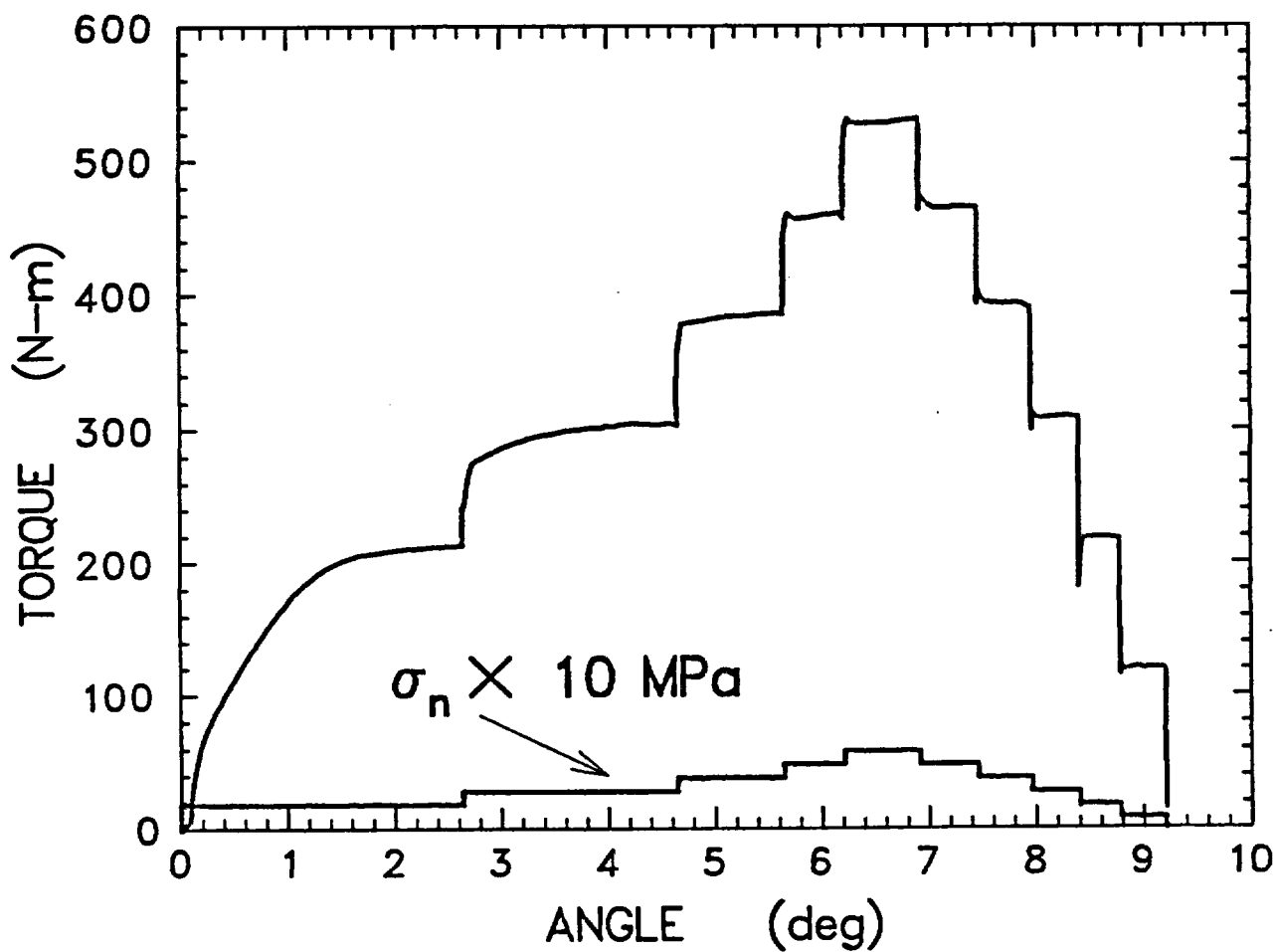


Figure 12. The effect of changes in normal stress during momentary stationary contact. Note the increasing sharpness of the yield regions with increasing normal stress and, also, the slip-weakening behavior on the two highest increments and all of the decrements, except 3 to 2 MPa (Experiment RFT062).

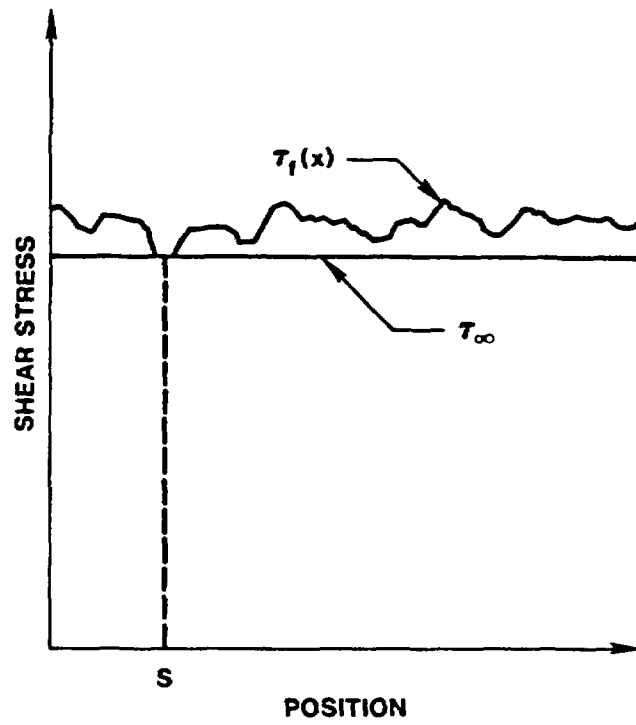
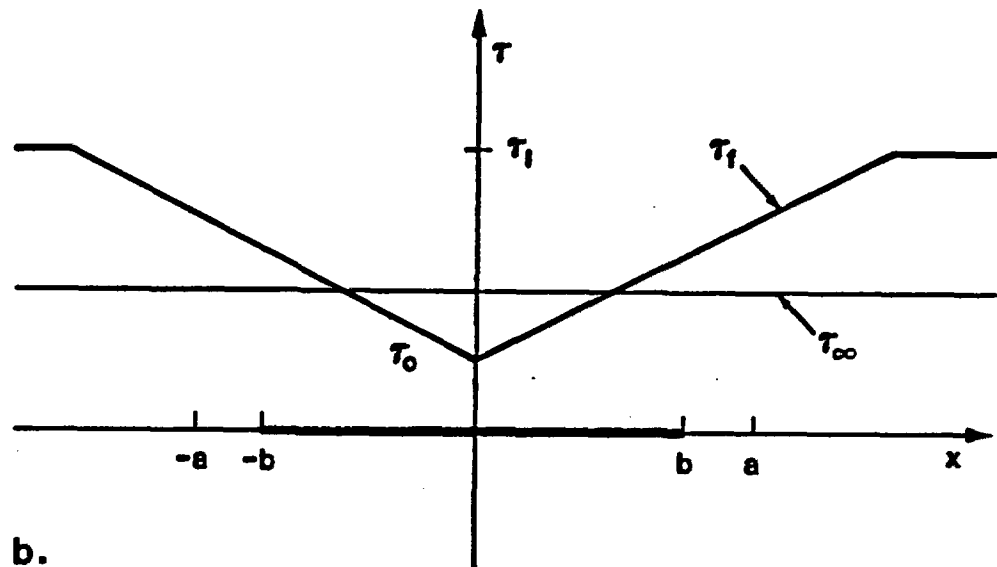
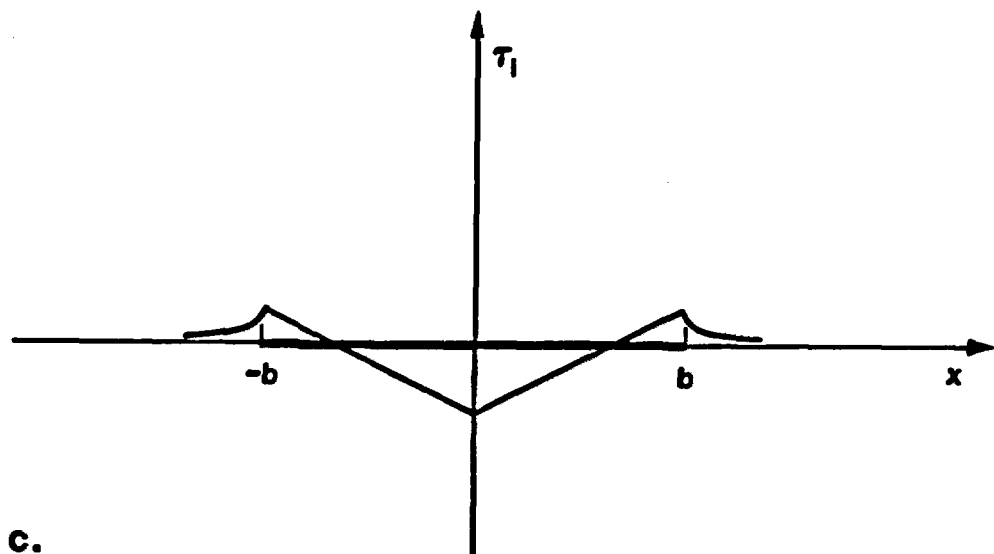


Figure 13. Friction stress, $\tau_f(x)$, and the applied stress, τ_{∞} , as a function of position.

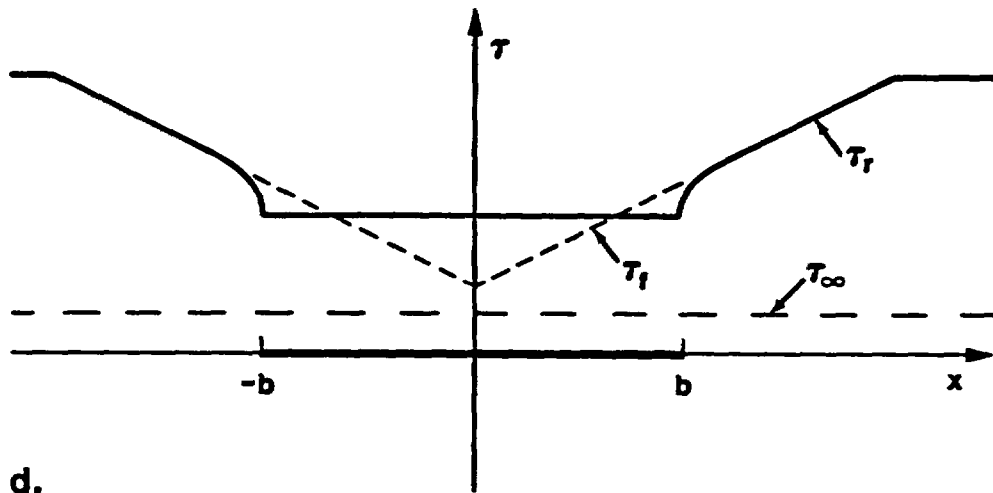


b.

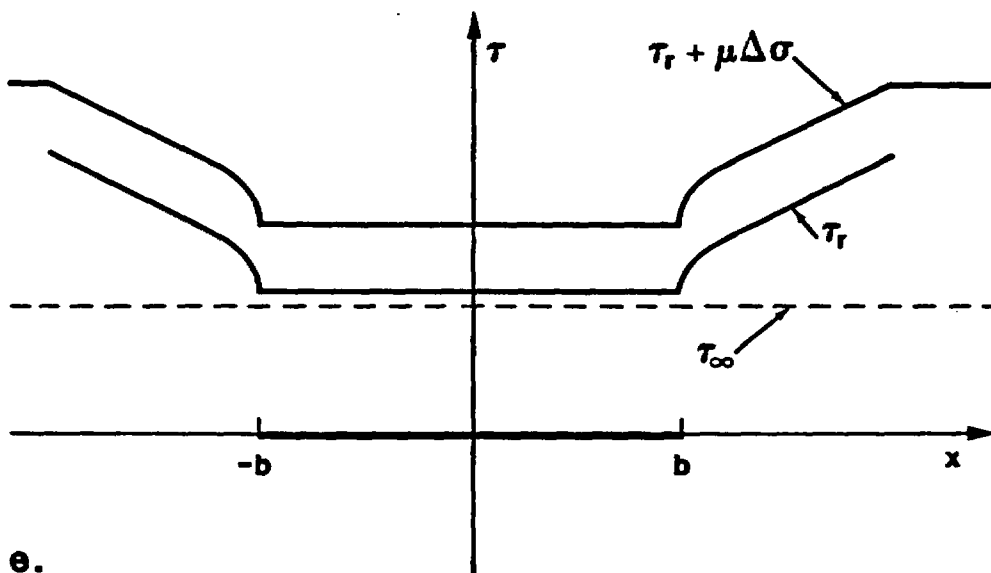


c.

Figure 13 cont. (b) The friction stress, $\tau_f(x)$, applied stress, τ_∞ , and the slip zone. (c) The internal stress resulting from slip in the interval $[-b, b]$.



d.



e.

Figure 13 cont. (d) The resistive stress, $\tau_r(x) \equiv \tau_f(x) - \tau_i(x)$ shown as a solid line; the friction stress $\tau_f(x)$ shown by dashed line. (e) The effect on the resistive stress, $\tau_r(x)$, of a change in the normal stress, $\Delta\sigma$.

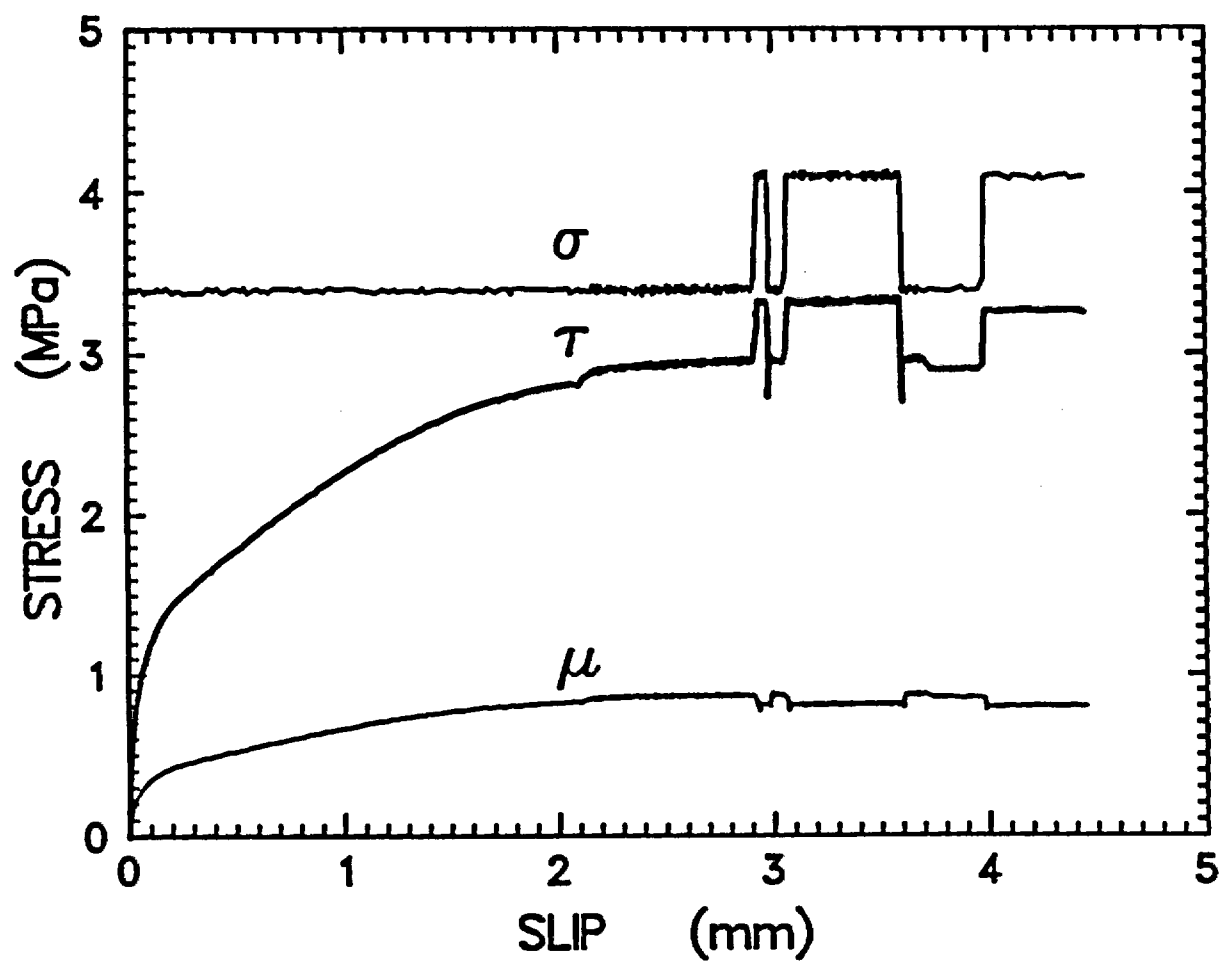


Figure 14. Shear stress response to a step-history normal stress during constant velocity sliding at 10^{-6} m/s for test RFT064. There is no significant memory of past normal stress indicated.

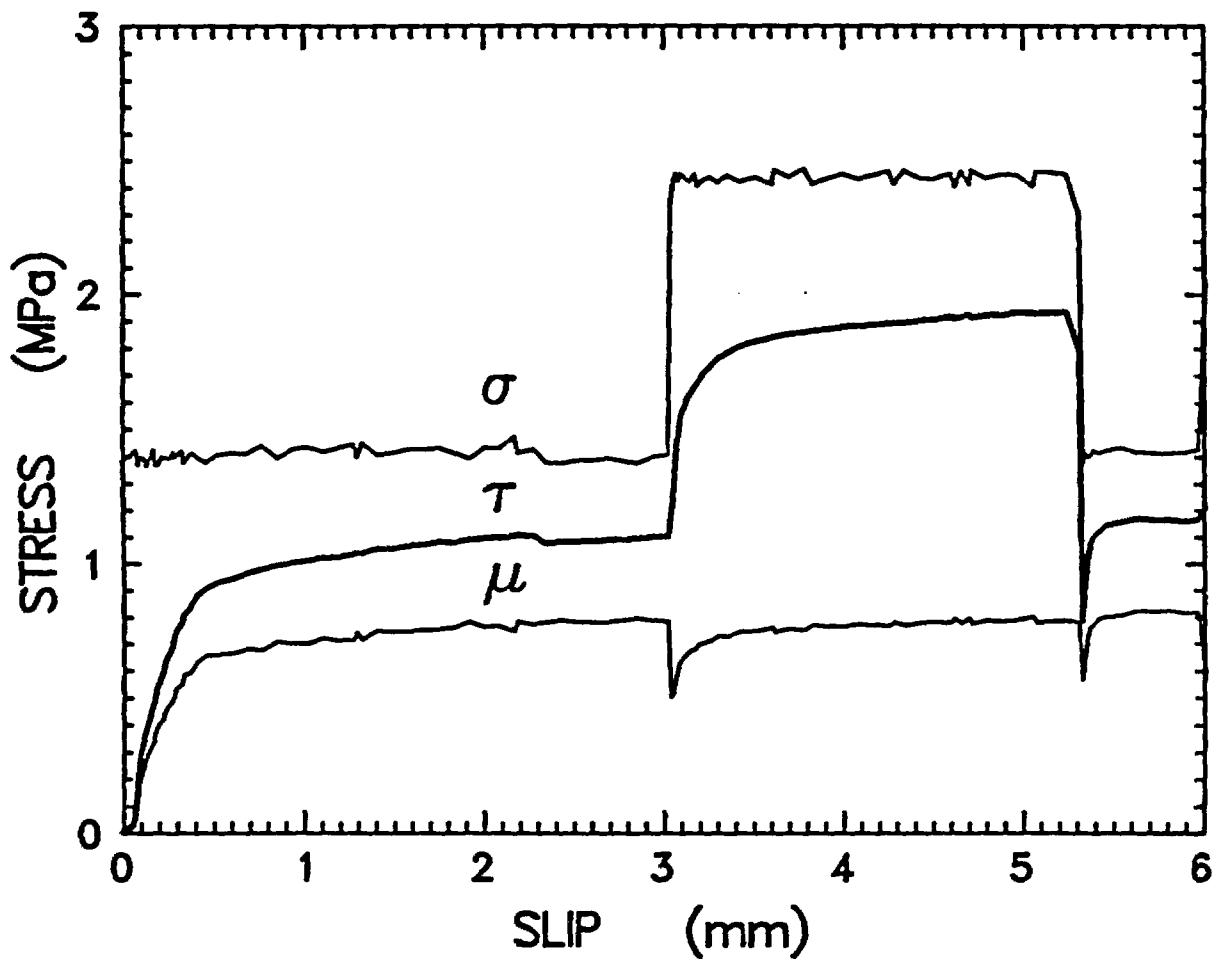


Figure 15. Shear stress response to a step-history normal stress during constant velocity sliding at 10^{-5} m/s for test RFT077. From a slip of about 3 to 5 mm there is a gradual strengthening of the interface following the step increase in normal stress. This is an example of a fading memory of past normal stress.

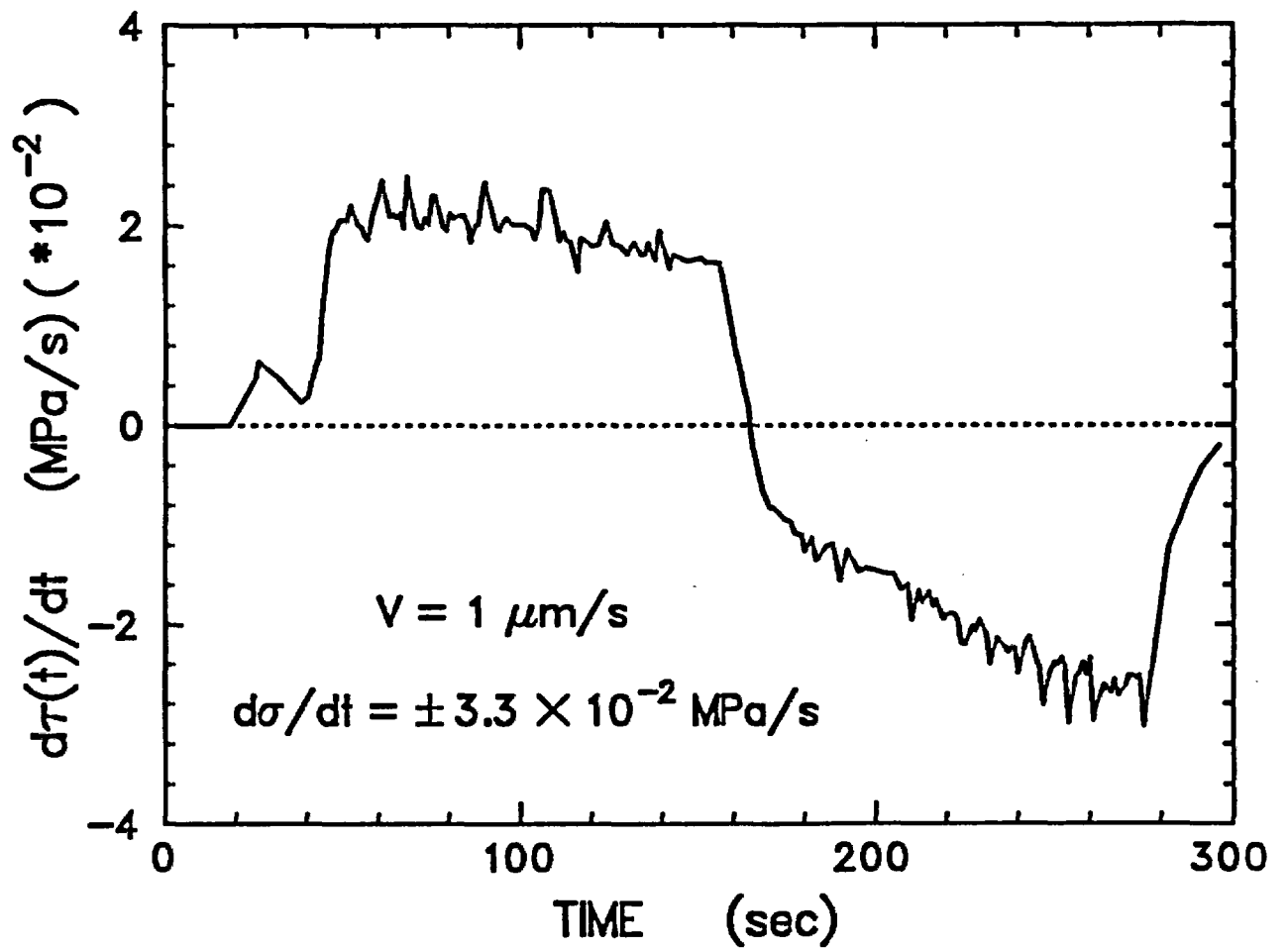


Figure 16. The variation of $d\tau(t)/dt$ with time (Experiment RFT079).

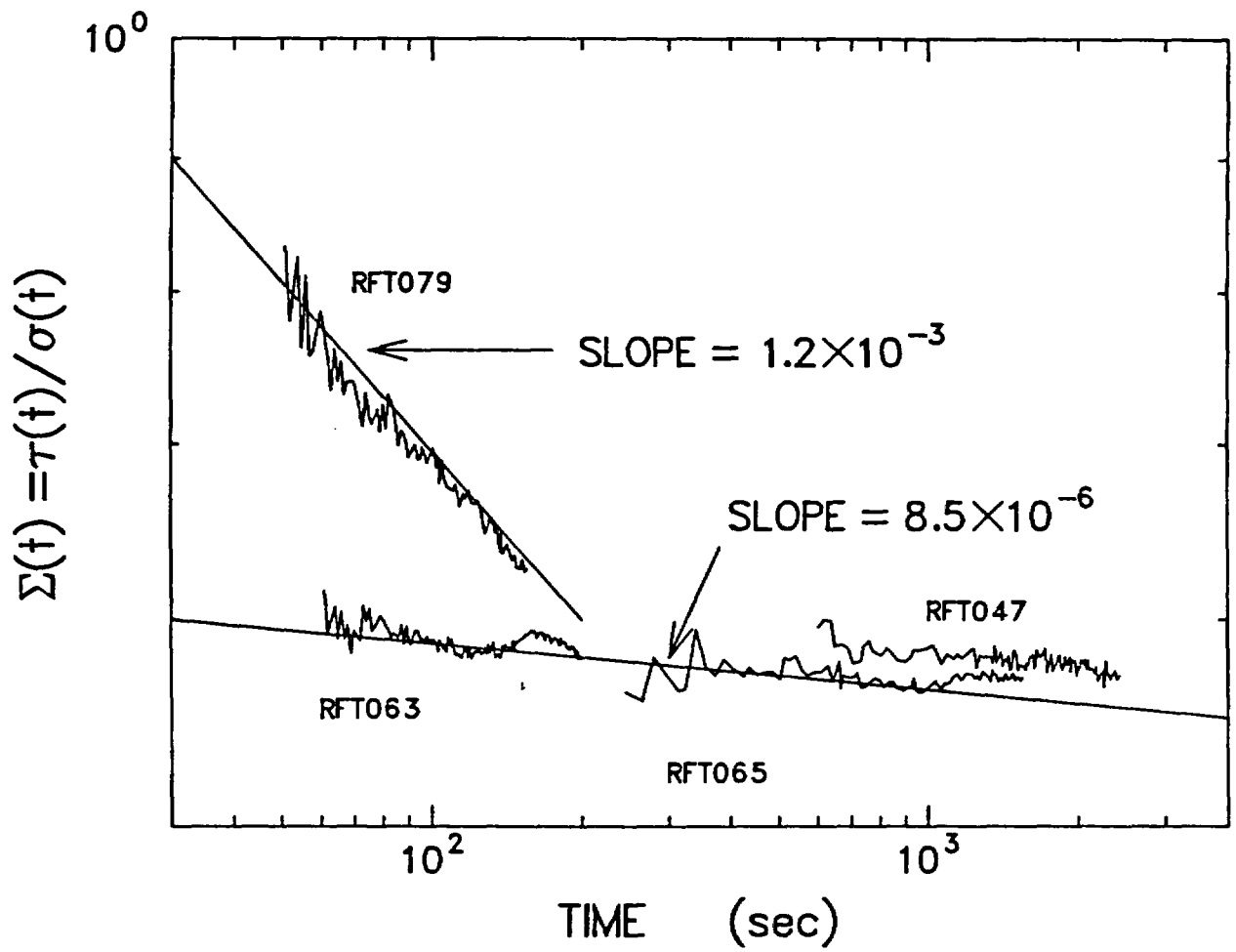


Figure 17. $\Sigma(t)$ plotted against time. The slope, which is interpreted as a correction factor, is small in comparison to 1.

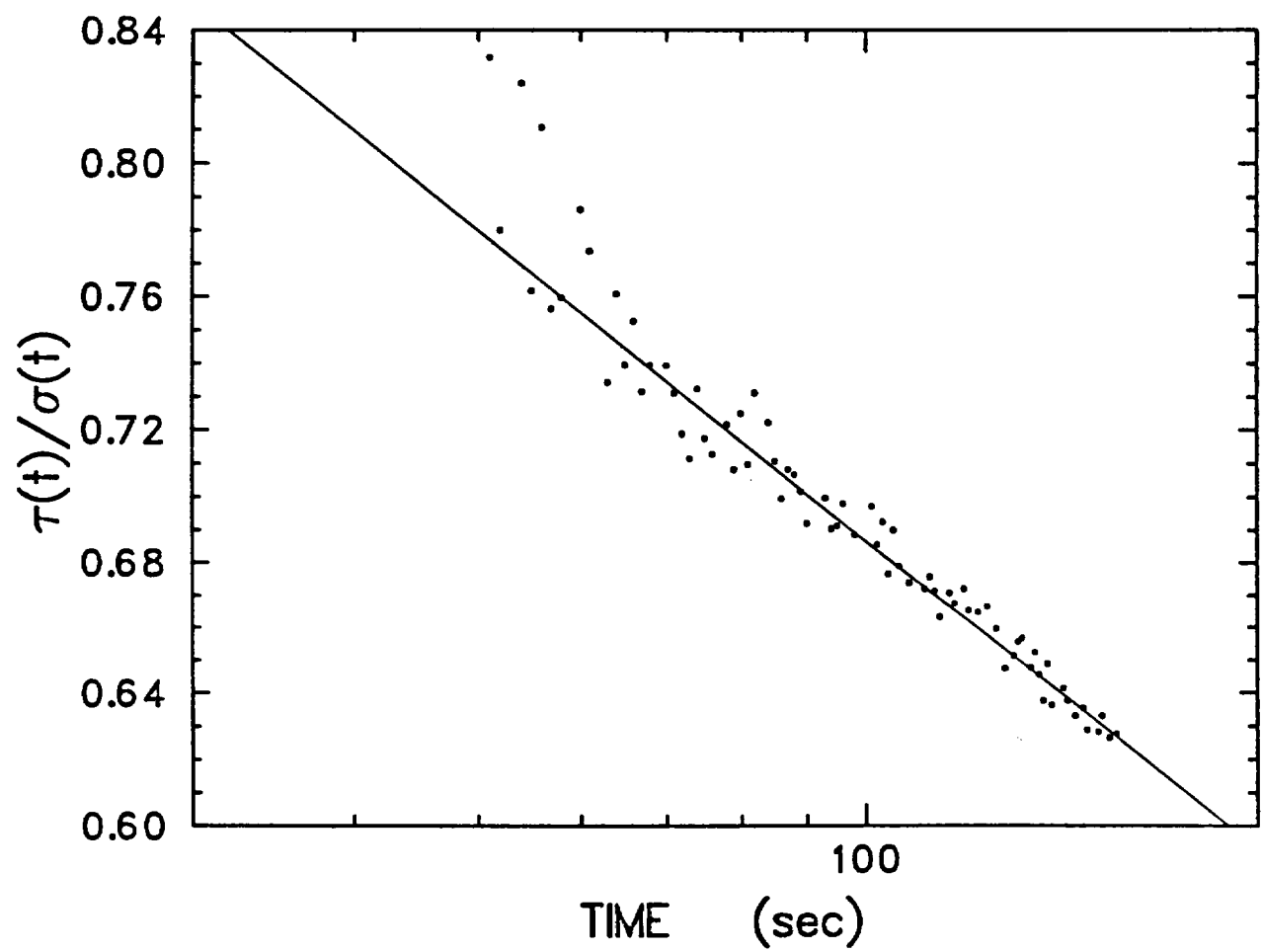


Figure 18. The generalized coefficient of friction is a decaying exponential in time (Experiment RFT079).

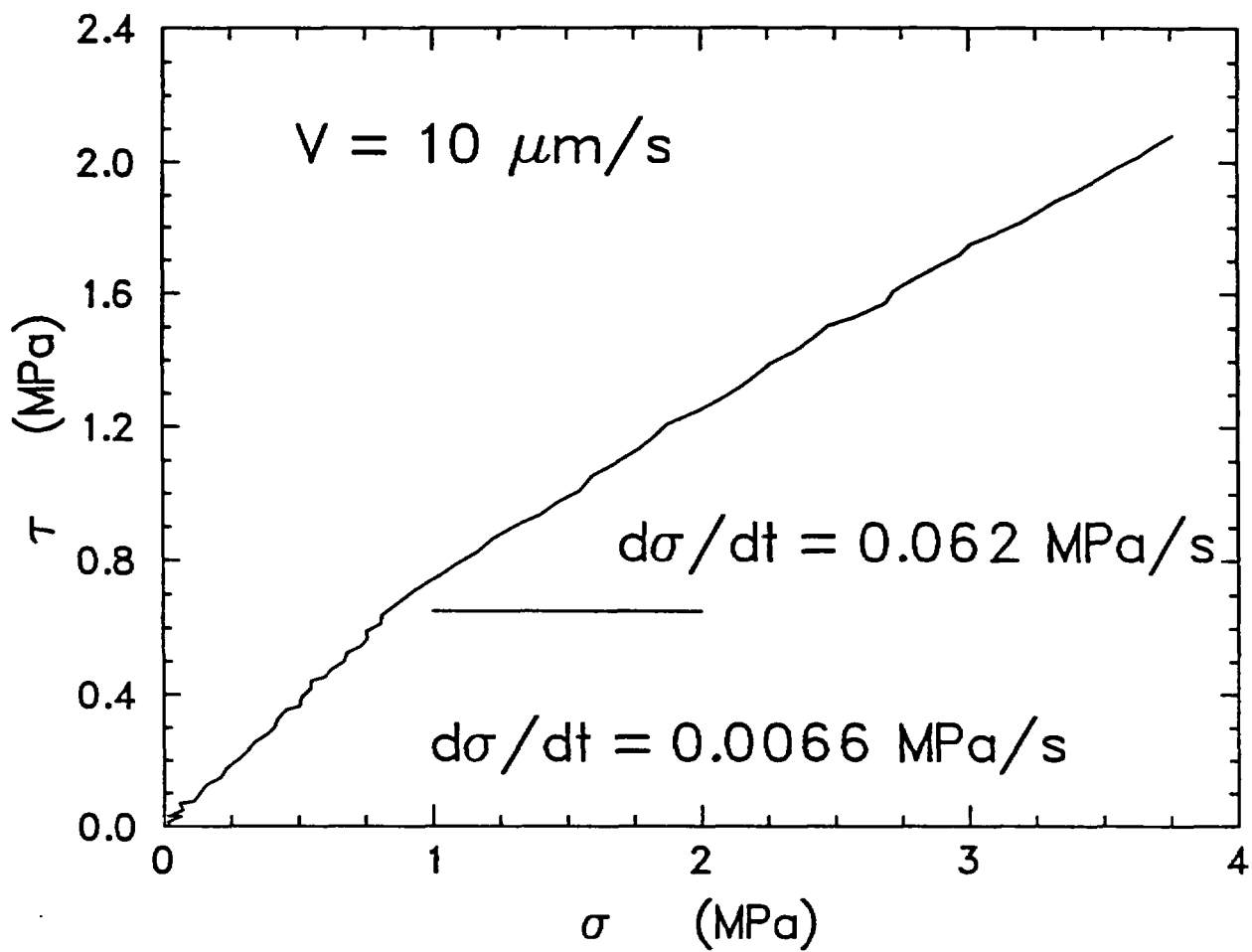


Figure 19. Effect of a decade increase in normal stress rate on the slip condition obtained at constant underlying sliding velocity (Experiment **RFT078**).

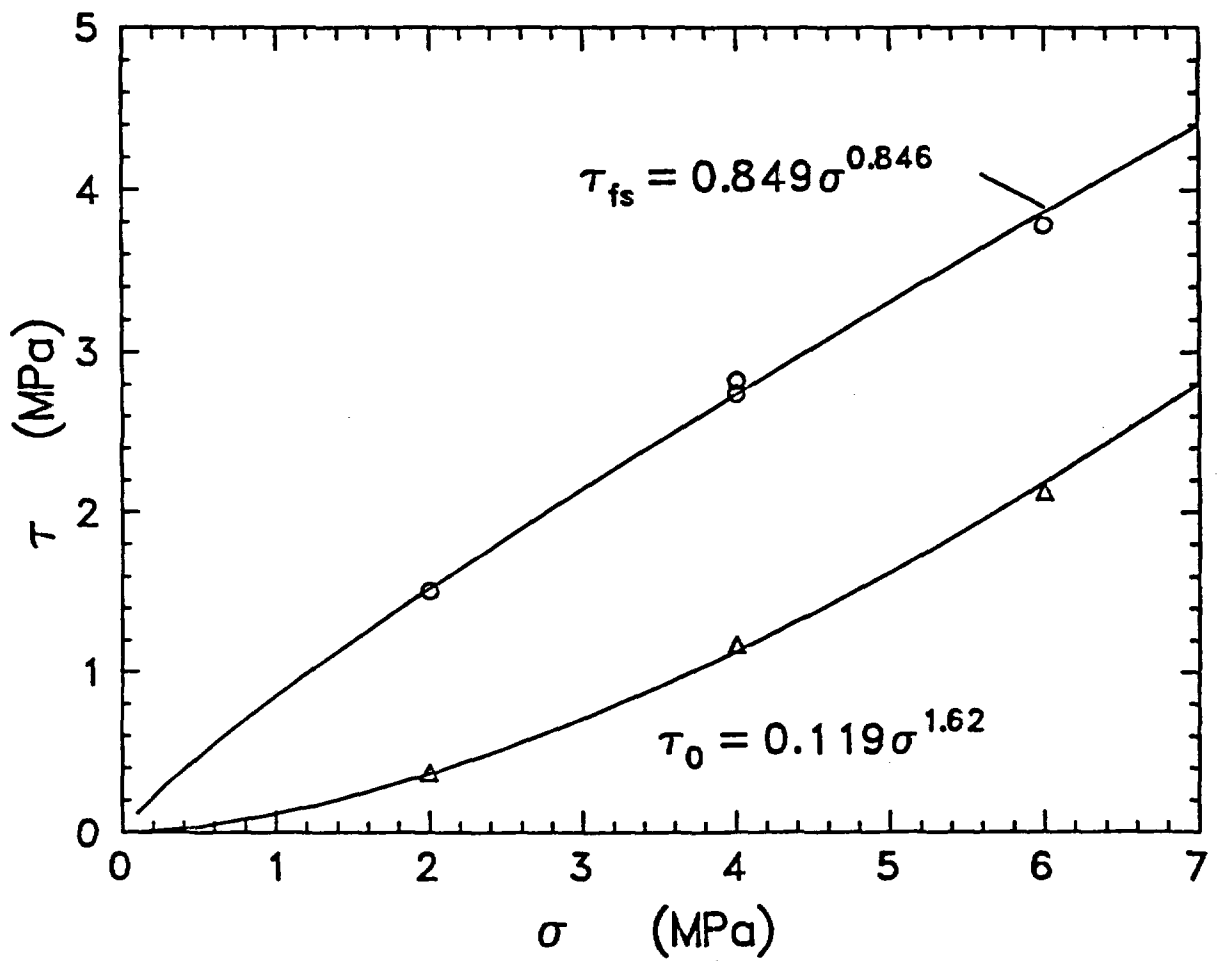


Figure 20. The duality of the slip condition; the upper curve is the stress at continuing, uniform slip, the lower curve is the onset of sliding (Experiment RFT059).

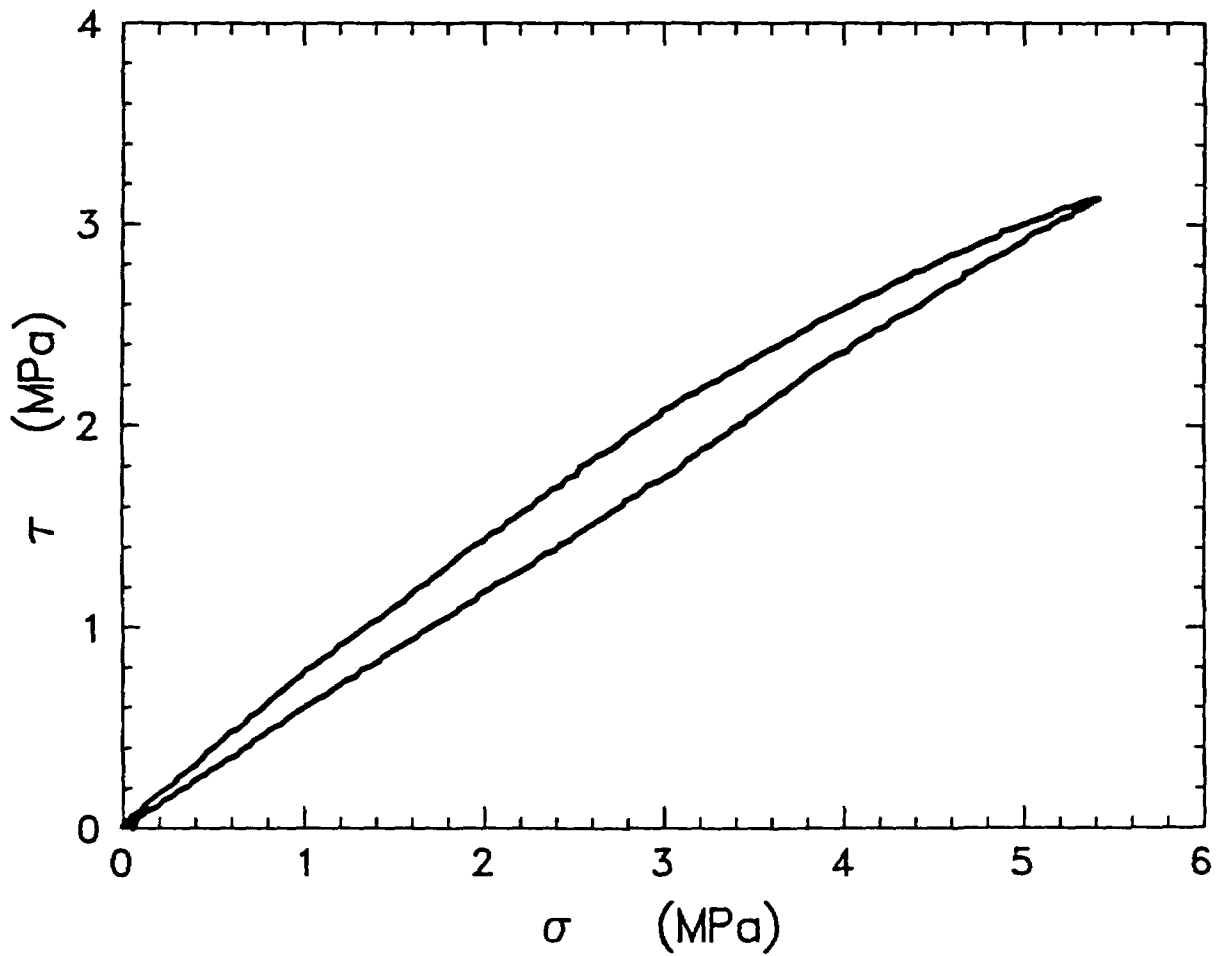


Figure 21. The slip condition mapped out in one test on one sample. The stress path is counterclockwise from the origin (Experiment RFT063).

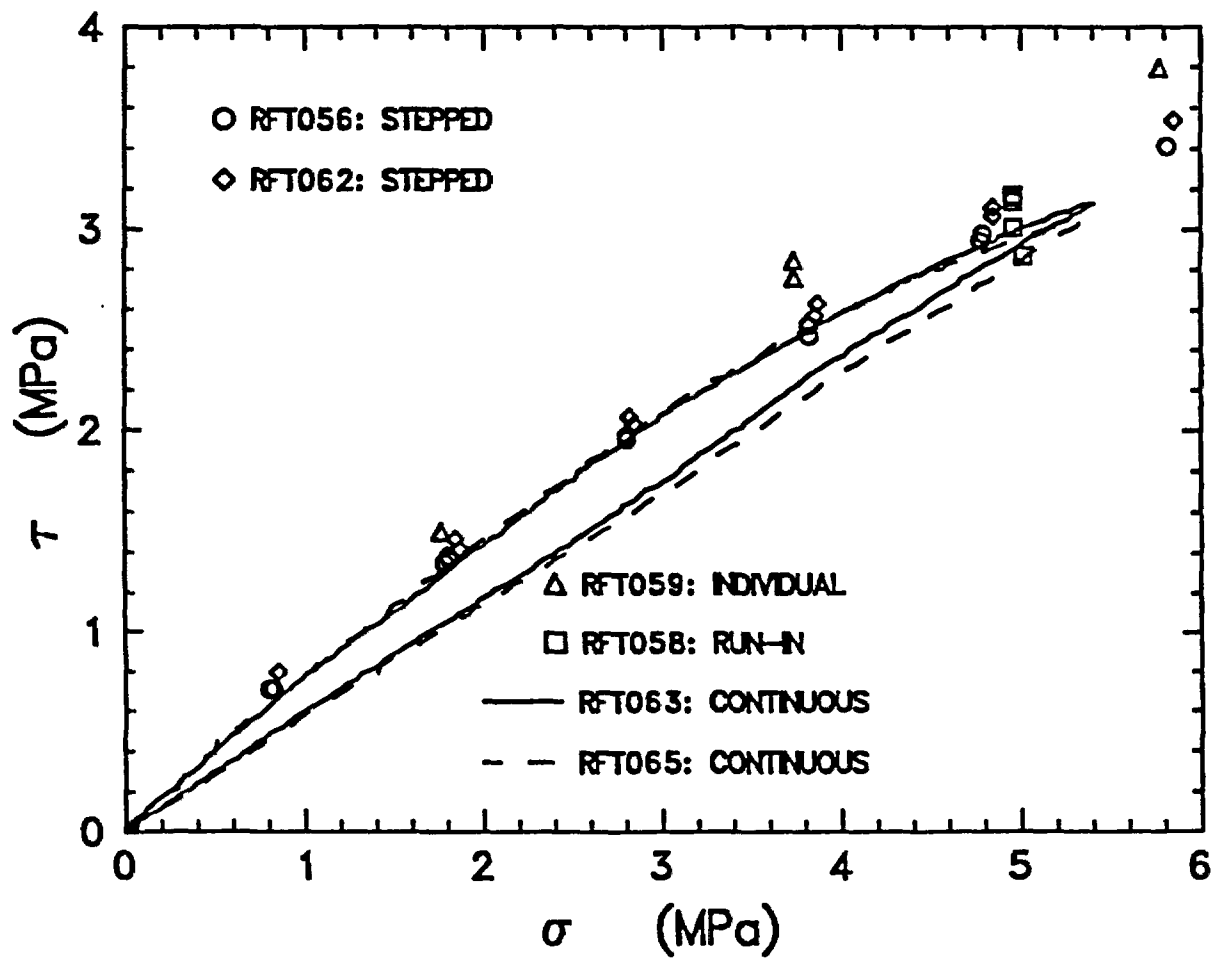


Figure 22. Comparison of the slip condition obtained from several stress histories.

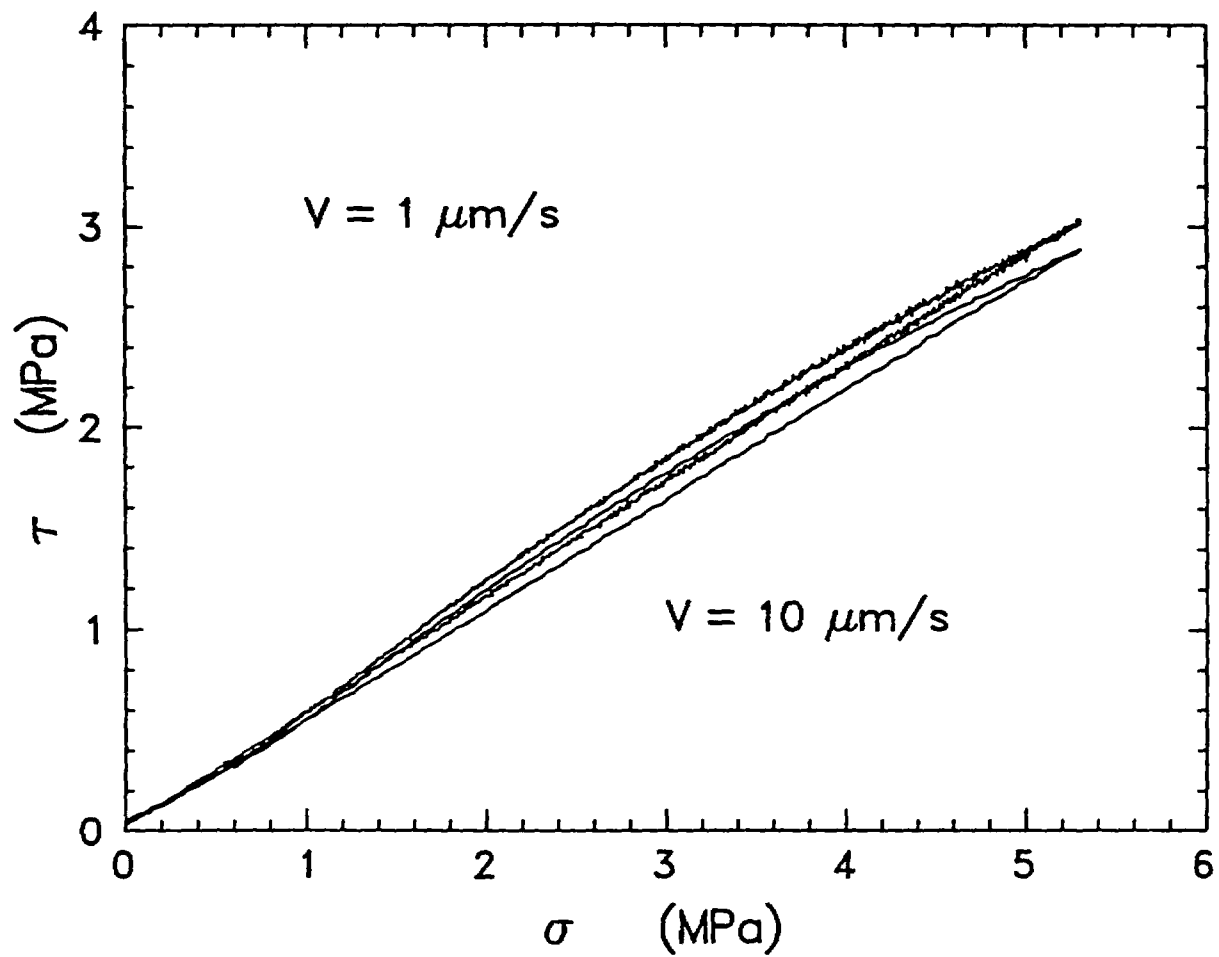


Figure 23. Effect of underlying sliding velocity on the slip condition obtained during ramping up and down of the normal stress (Experiment RFT046 and RFT047).

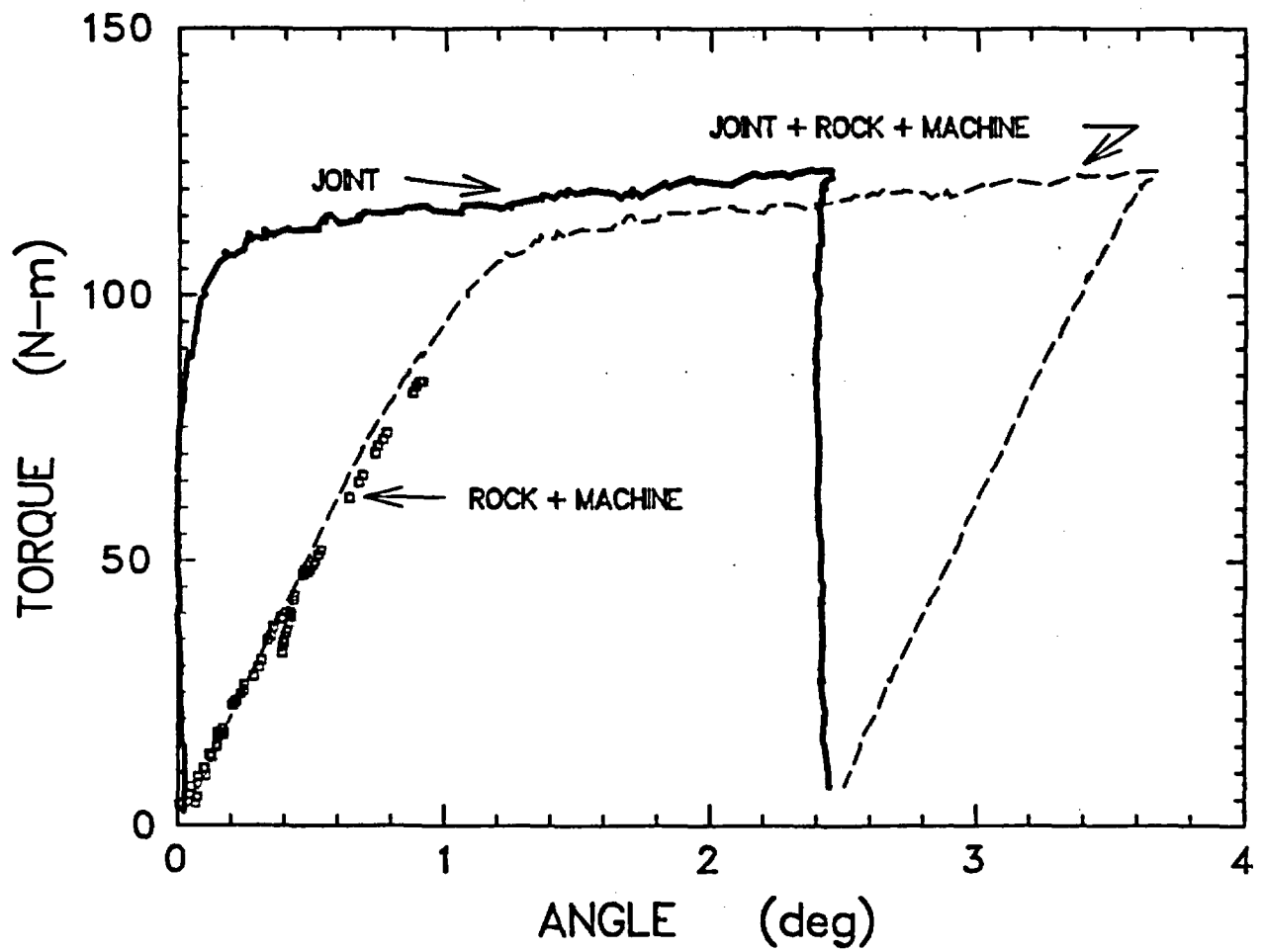


Figure 24. Torque *versus* offset for a rough surface (laboratory-induced tensile fracture) (Experiment RFT013).

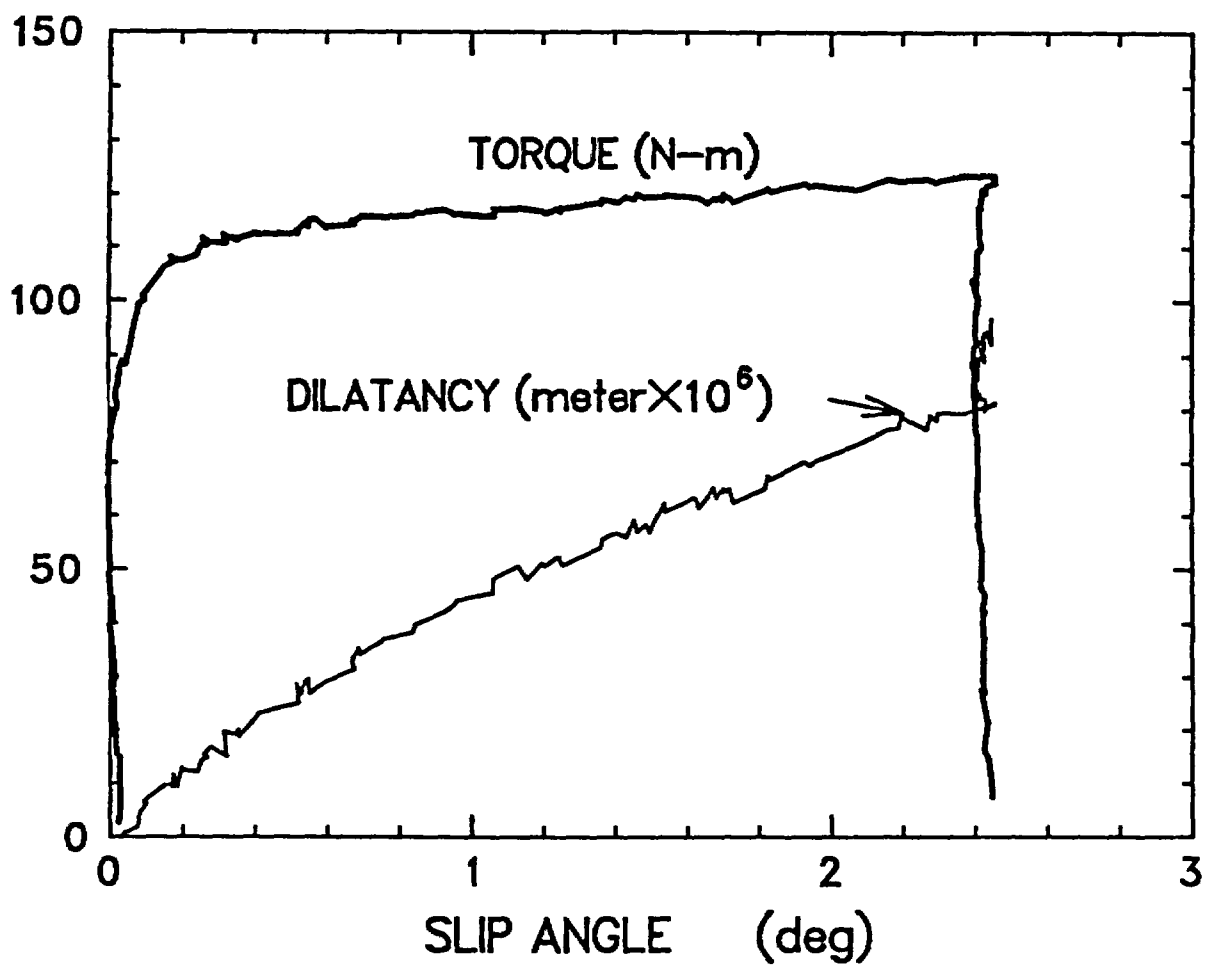


Figure 25. Same as Figure 24 but showing the dilatancy curve; compaction is positive. The surfaces were initially unmated; sample 16D.

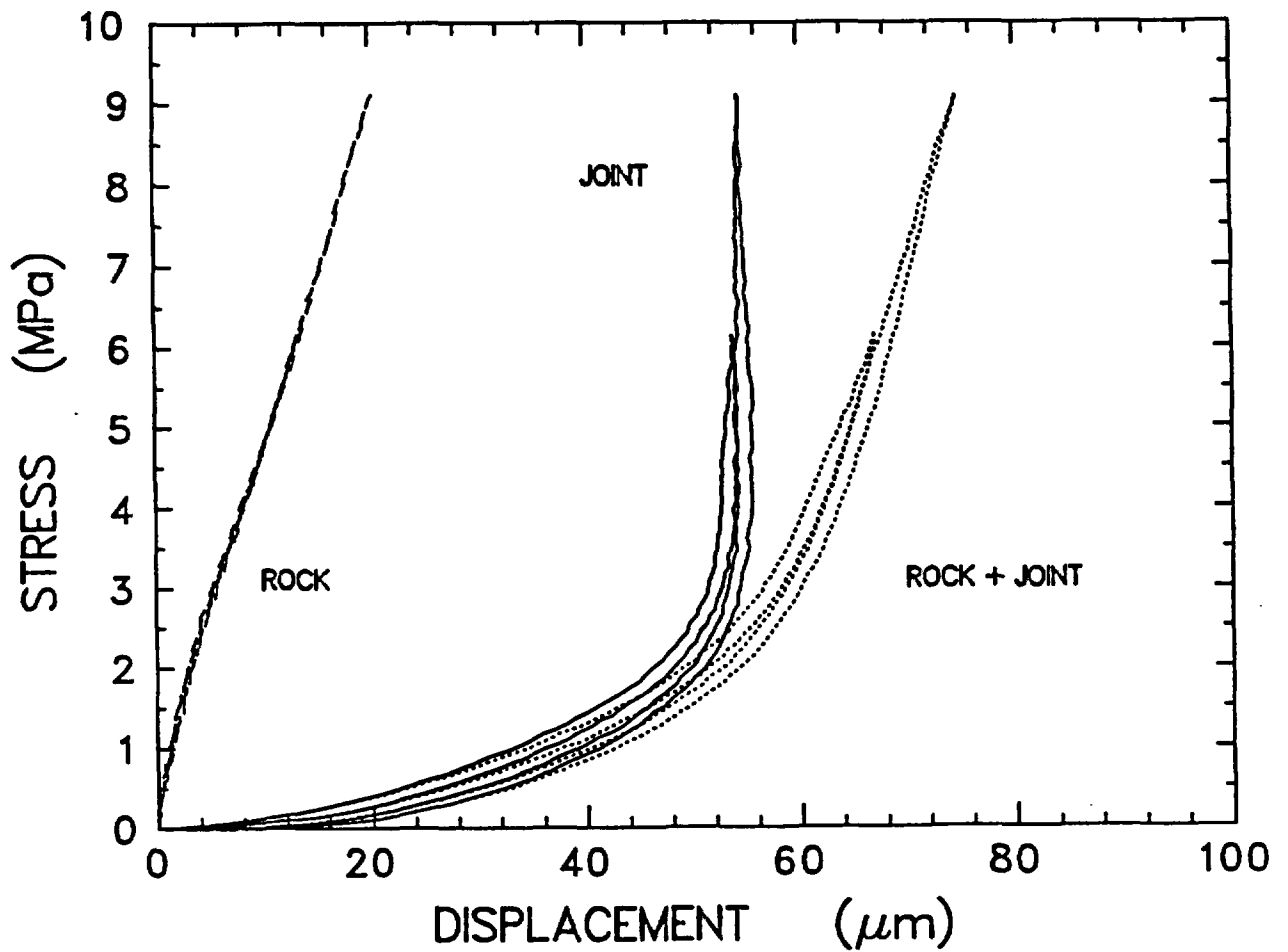


Figure 26. Normal stiffness for sample 16D in the initially mated condition. Notice that the stiffness becomes infinite at a stress near 3 MPa. The hysteresis loops are relatively small, and there is no measurable permanent deformation.

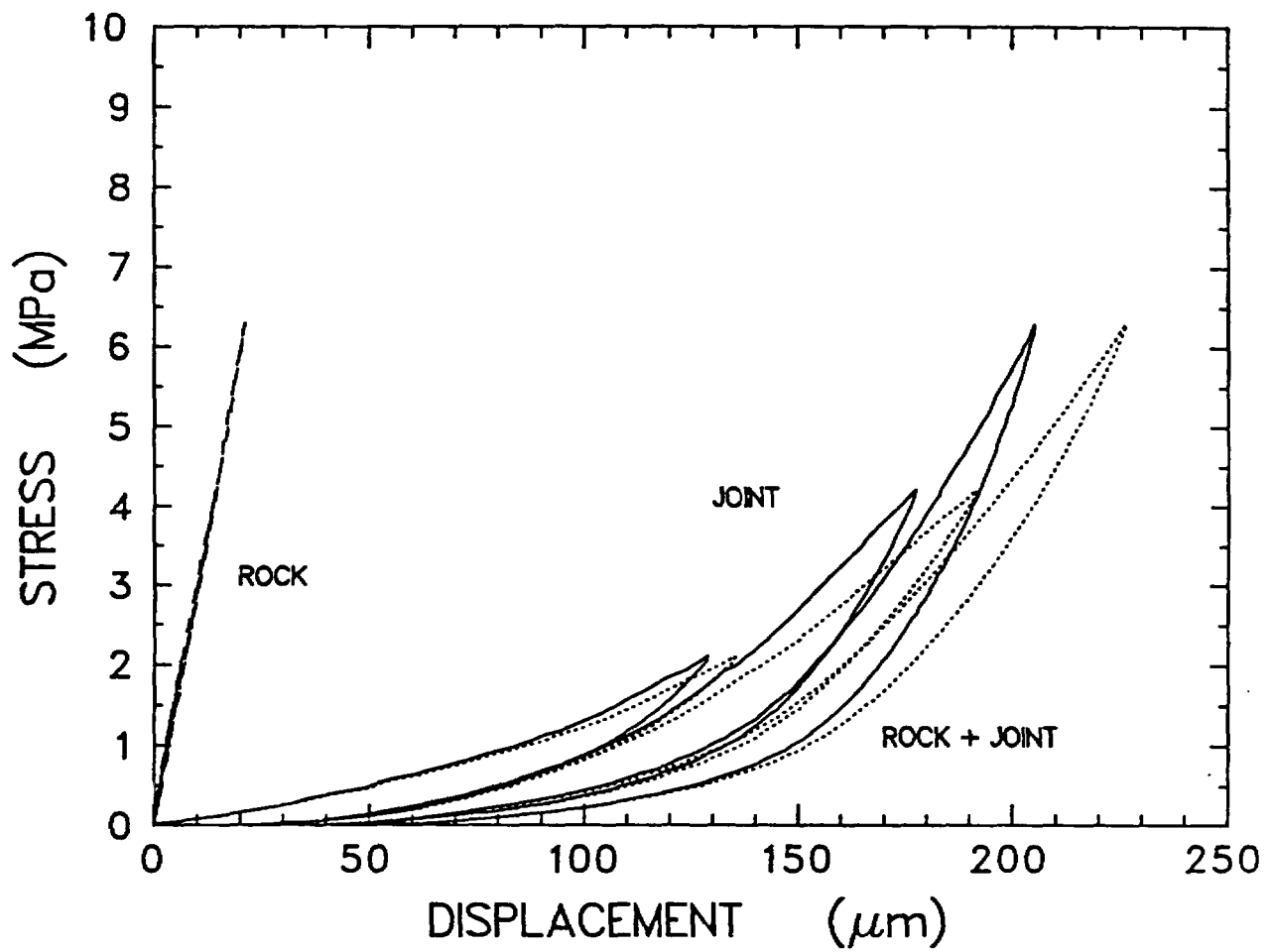


Figure 27. Normal stiffness for sample 16D in the initially unmated condition. Observe the large hysteresis loops and noticeable permanent deformations compared to the initially mated condition shown in Figure 27.

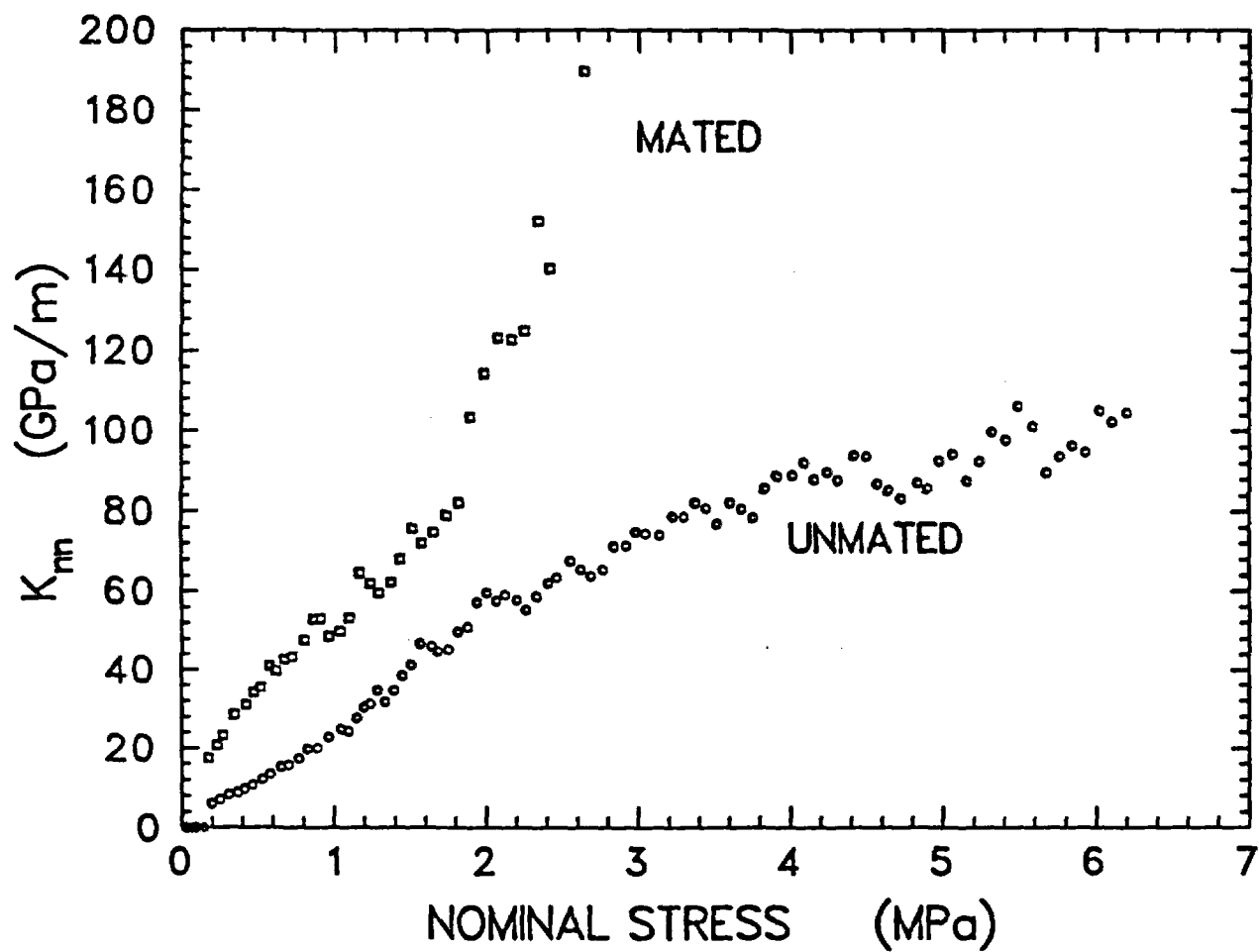


Figure 28. The normal stiffness as a function of (nominal) normal stress for the mated and unmated initial conditions for a rough surface of Topopah Spring tuff. (16D).

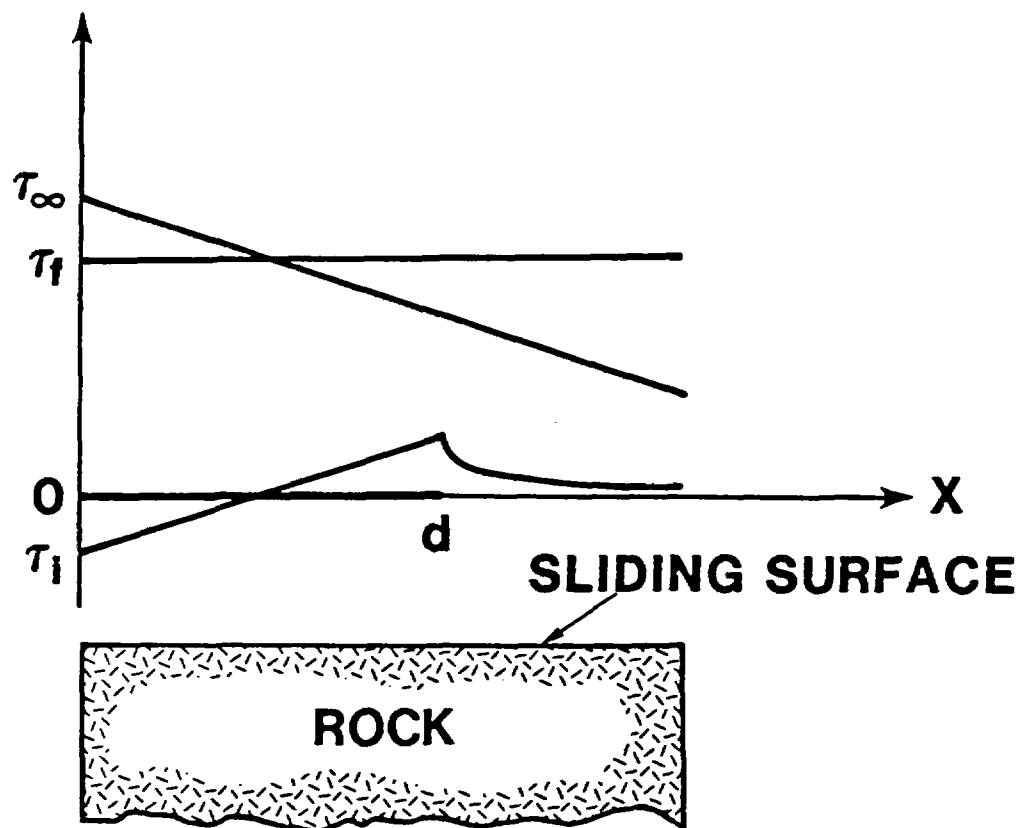


Figure A1. Shear stresses that exist on a slipping interface when the slip zone $(0, d)$ covers only part of the whole surface.

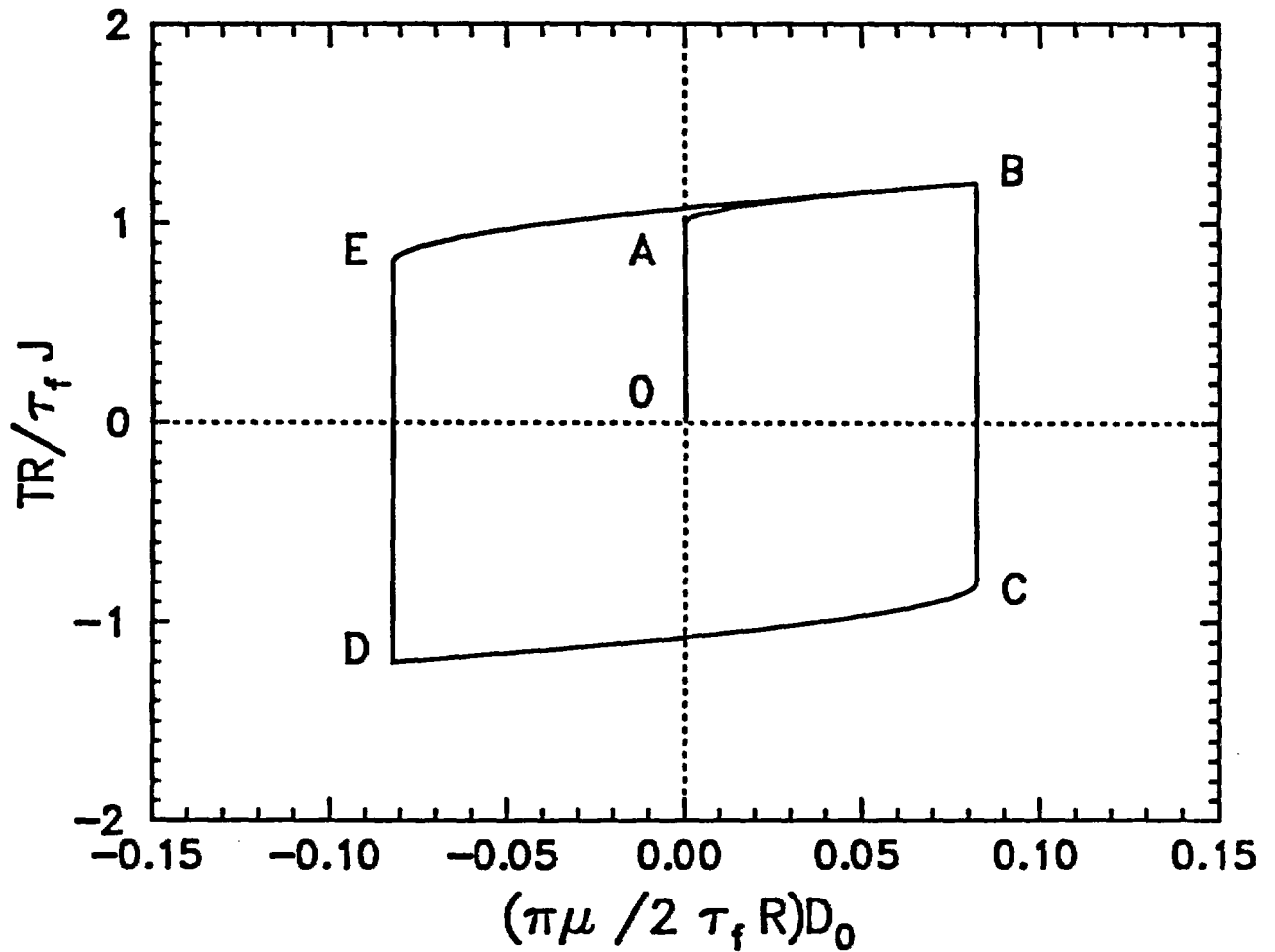


Figure A2. A response curve for the theoretical model in dimensionless units. The torque history starts at point 0. Slip begins at point A and continues to B, where the torque is reversed. The slipping surface then sticks together until the reverse torque causes reverse slip to begin at C and continue to D. Sticking again occurs from D to E, where renewed forward slip begins. The second phase of forward torquing ends at exactly the same point where the first phase ended, and is a result of discrete memory.

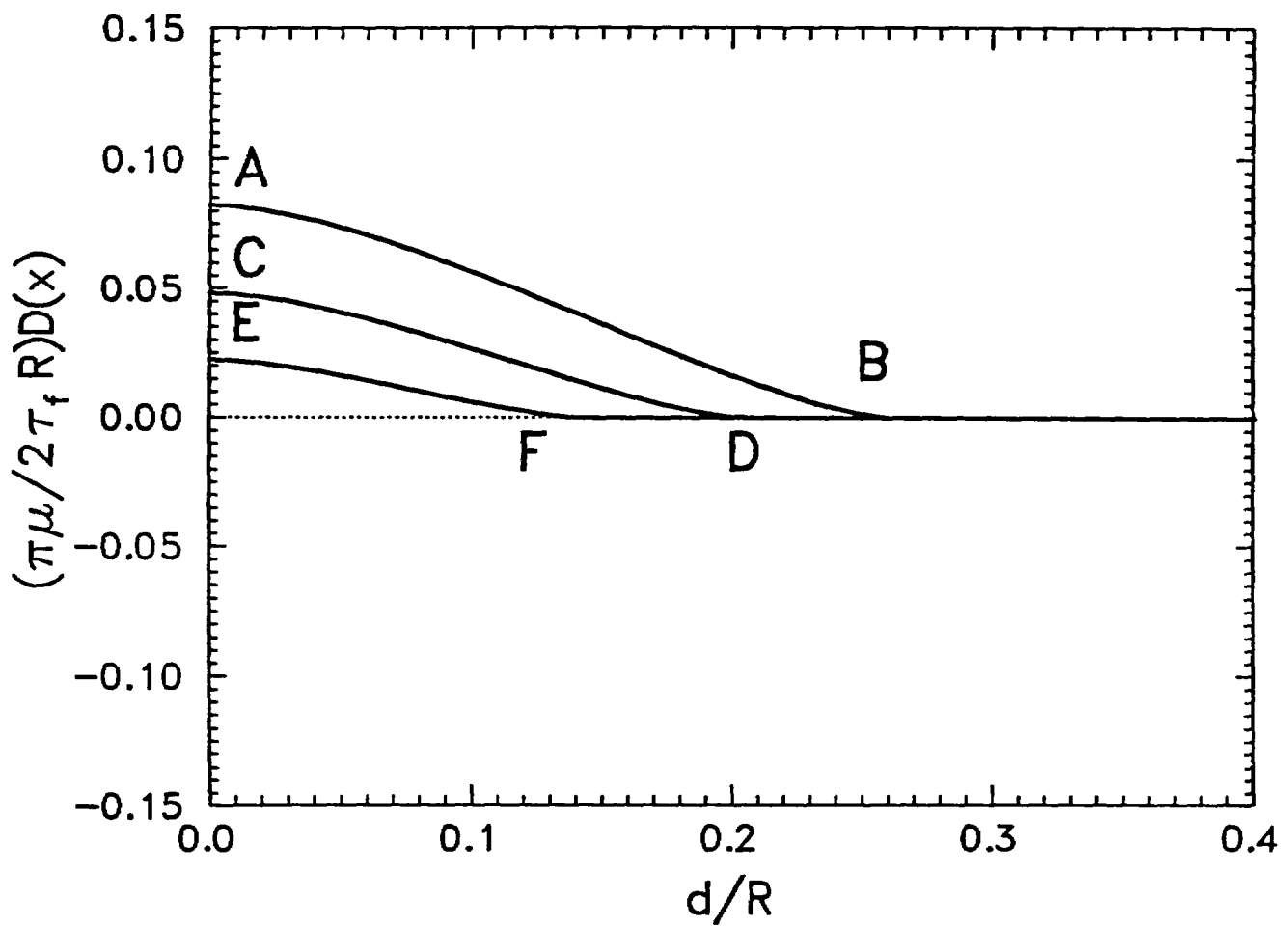


Figure A3. Growth of the slip zone during forward torquing. The successive curves EF, CD, and AB are associated with increasing torques.

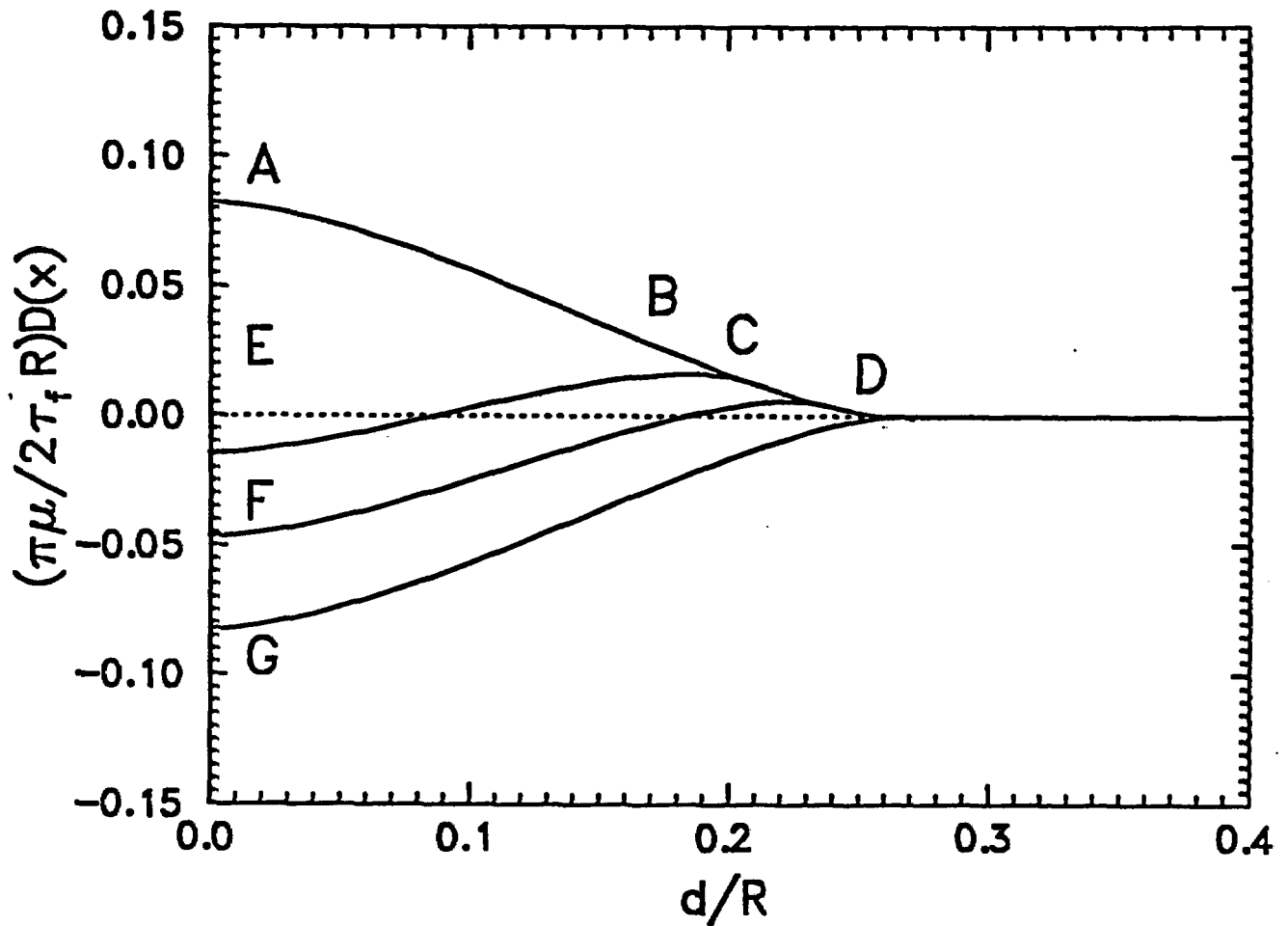


Figure A4. Development of the net slip distribution during reverse slip. The curve ABCD was produced at the furthest extent of forward torquing. During reverse torquing, the successive curves EB, FC, and, finally, GD are produced. Never during reverse torquing is the slip uniformly zero.

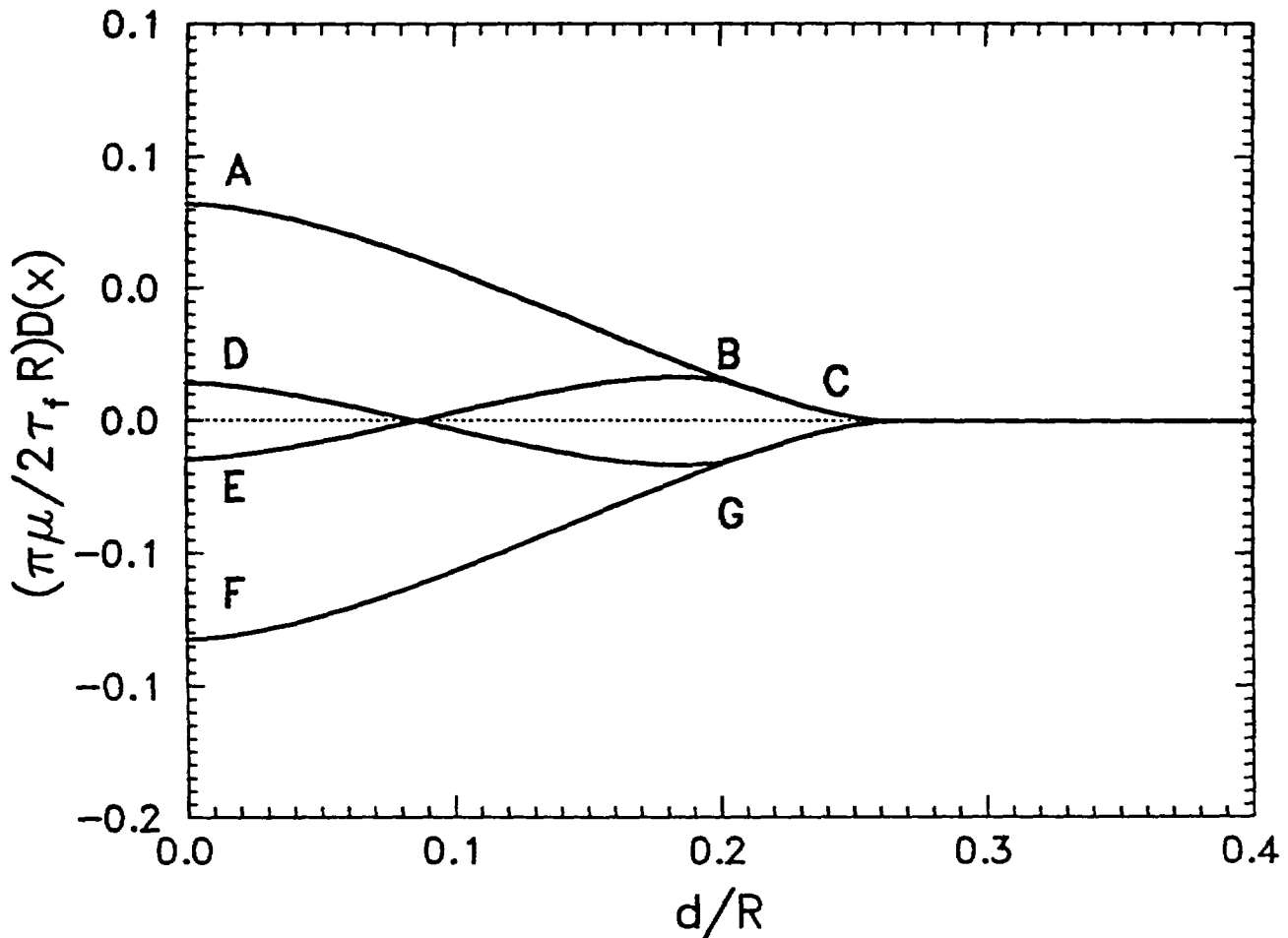


Figure A5. Development of the net slip distribution during the three-phase torquing history of Figure A1. At the cessation of first torquing, the profile is ABC. Partway through the reverse torquing phase, the profile is given by EBC, and at the end of reverse torquing, it is given by FGC. Following some second-phase torquing, the profile becomes DGC, and then, finally, the profile reassumes curve ABC. This causes the torque-versus-slip curve to return to exactly the same point where the first untorquing began.

Appendix C

Sample Key

<u>Experiment Number</u>	<u>Sample Number</u>
RFT013	16D
RFT026	16B-BB/16C-CC
RFT028	"
RFT030	"
RFT047	"
RFT056	16B-AA/16C-CC
RFT058	"
RFT059	"
RFT062	"
RFT063	"
RFT065	"
RFT078	16C-AA*/16C-CC
RFT079	"
NST007	16D
NST008	"

*16C-AA was sawed in half lengthwise and the inner diameter was ground out to 69.8 ± 0.15 mm.

Appendix D

Data Status

This report contains no data from, or for inclusion in, the RIB and/or SEPDB.

DISTRIBUTION LIST

B. C. Rusche, Director (RW-1)
Office of Civilian Radioactive
Waste Management
U. S. Department of Energy
Forrestal Building
Washington, D. C. 20585

R. Stein (RW-24)
Office of Geologic Repositories
U. S. Department of Energy
Forrestal Building
Washington, D. C. 20585

J. J. Fiore (RW-22)
Program Management Division
Office of Geologic Repositories
U. S. Department of Energy
Forrestal Building
Washington, D. C. 20585

M. W. Frei (RW-24)
Engineering & Licensing Division
Office of Geologic Repositories
U. S. Department of Energy
Forrestal Building
Washington, D. C. 20585

E. S. Burton (RW-25)
Siting Division
Office of Geologic Repositories
U. S. Department of Energy
Forrestal Building
Washington, D. C. 20585

C. R. Cooley (RW-24)
Geosciences & Technology Division
Office of Geologic Repositories
U. S. Department of Energy
Forrestal Building
Washington, D. C. 20585

V. J. Cassella (RW-22)
Office of Geologic Repositories
U. S. Department of Energy
Forrestal Building
Washington, D. C. 20585

T. P. Longo (RW-25)
Program Management Division
Office of Geologic Repositories
U. S. Department of Energy
Forrestal Building
Washington, D. C. 20585

C. Klingsberg (RW-24)
Geosciences & Technology Division
Office of Geologic Repositories
U. S. Department of Energy
Forrestal Building
Washington, D. C. 20585

B. G. Gale (RW-25)
Siting Division
Office of Geologic Repositories
U. S. Department of Energy
Forrestal Building
Washington, D. C. 20585

R. J. Blaney (RW-22)
Program Management Division
Office of Geologic Repositories
U. S. Department of Energy
Forrestal Building
Washington, D. C. 20585

R. W. Gale (RW-40)
Office of Policy, Integration, and
and Outreach
U. S. Department of Energy
Forrestal Building
Washington, D. C. 20585

J. E. Shaheen (RW-44)
Outreach Programs
Office of Policy, Integration,
and Outreach
U. S. Department of Energy
Forrestal Building
Washington, D. C. 20585

J. O. Neff
Salt Repository Project Office
U. S. Department of Energy
505 King Avenue
Columbus, OH 43201

D. C. Newton (RW-23)
Engineering & Licensing Division
Office of Geologic Repositories
U. S. Department of Energy
Forrestal Building
Washington, D. C. 20585

O. L. Olson, Manager
Basalt Waste Isolation Project Office
U. S. Department of Energy
Richland Operations Office
Post Office Box 550
Richland, WA 99352

D. L. Vieth, Director (4)
Waste Management Project Office
U. S. Department of Energy
Post Office Box 14100
Las Vegas, NV 89114

D. F. Miller, Director
Office of Public Affairs
U. S. Department of Energy
Post Office Box 14100
Las Vegas, NV 89114

P. M. Bodin (12)
Office of Public Affairs
U. S. Department of Energy
Post Office Box 14100
Las Vegas, NV 89114

B. W. Church, Director
Health Physics Division
U. S. Department of Energy
Post Office Box 14100
Las Vegas, NV 89114

Chief, Repository Projects Branch
Division of Waste Management
U. S. Nuclear Regulatory Commission
Washington, DC 20555

Document Control Center
Division of Waste Management
U. S. Nuclear Regulatory Commission
Washington, DC 20555

S. A. Mann, Manager
Crystalline Rock Project Office
U. S. Department of Energy
9800 South Cass Avenue
Argonne, IL 60439

K. Street, Jr.
Lawrence Livermore National Laboratory
Post Office Box 808
Mail Stop L-209
Livermore, CA 94550

L. D. Ramspott (3)
Technical Project Officer for NNWSI
Lawrence Livermore National Laboratory
Post Office Box 808
Mail Stop L-204
Livermore, CA 94550

W. J. Purcell (RW-20)
Office of Geologic Repositories
U. S. Department of Energy
Forrestal Building
Washington, D. C. 20585

D. T. Oakley (4)
Technical Project Officer for NNWSI
Los Alamos National Laboratory
Post Office Box 1663
Mail Stop F-619
Los Alamos, NM 87545

W. W. Dudley, Jr. (3)
Technical Project Officer for NNWSI
U. S. Geological Survey
Post Office Box 25046
418 Federal Center
Denver, CO 80225

NTS Section Leader
Repository Projects Branch
Division of Waste Management
U. S. Nuclear Regulatory Commission
Washington, DC 20555

V. M. Glanzman
U. S. Geological Survey
Post Office Box 25046
913 Federal Center
Denver, CO 80225

P. T. Prestholt
NRC Site Representative
1050 East Flamingo Road
Suite 319
Las Vegas, NV 89109

M. E. Spaeth
Technical Project Officer for NNWSI
Science Applications International, Corp.
101 Convention Center Drive, Suite 409
Las Vegas, NV 89109

SAIC-T&MSS Library (2)
Science Applications International, Corp.
2950 South Highland Drive
Las Vegas, NV 89109

W. S. Twenhofel, Consultant
Science Applications International, Corp.
820 Estes Street
Lakewood, CO 80215

A. E. Gurrola, General Manager
Energy Support Division
Holmes & Narver, Inc.
Post Office Box 14340
Las Vegas, NV 89114

J. A. Cross, Manager
Las Vegas Branch
Fenix & Scisson, Inc.
Post Office Box 15408
Las Vegas, NV 89114

N. Duncan (RW-44)
Office of Policy, Integration,
and Outreach
U. S. Department of Energy
Forrestal Building
Washington, D. C. 20585

J. Fordham
Desert Research Institute
Water Resources Center
Post Office Box 60220
Reno, NV 89506

J. S. Wright
Technical Project Officer for NNWSI
Westinghouse Electric Corporation
Waste Technology Services Division
Nevada Operations
Post Office Box 708
Mail Stop 703
Mercury, NV 89023

ONWI Library
Battelle Columbus Laboratory
Office of Nuclear Waste Isolation
505 King Avenue
Columbus, OH 43201

W. M. Hewitt, Program Manager
Roy E. Weston, Inc.
955 L'Enfant Plaza SW
Washington, DC 20024

H. D. Cunningham, General Manager
Reynolds Electrical & Engineering Company,
Inc.
Post Office Box 14400
Mail Stop 555
Las Vegas, NV 89114

T. Hay, Executive Assistant
Office of the Governor
State of Nevada
Capitol Complex
Carson City, NV 89710

R. R. Loux, Jr., Director (3)
Nuclear Waste Project Office
State of Nevada
Capitol Complex
Carson City, NV 89710

C. H. Johnson, Technical
Program Manager
Nuclear Waste Project Office
State of Nevada
Capitol Complex
Carson City, NV 89710

Dr. M. Mifflin
Desert Research Institute
Water Resources Center
Suite 1
2505 Chandler Avenue
Las Vegas, NV 89120

Department of Comprehensive Planning
Clark County
225 Bridger Avenue, 7th Floor
Las Vegas, NV 89155

Lincoln County Commission
Lincoln County
Post Office Box 90
Pioche, NV 89043

Community Planning and Development
City of North Las Vegas
Post Office Box 4086
North Las Vegas, NV 89030

City Manager
City of Henderson
Henderson, NV 89015

N. A. Norman
Project Manager
Bechtel National Inc.
Post Office Box 3965
San Francisco, CA 94119

F. Butler
Los Alamos Technical Associates
1650 Trinity Drive
Los Alamos, NM 87544

T. G. Barbour
Science Applications
International Corporation
1626 Cole Boulevard, Suite 270
Golden, CO 80401

Planning Department
Nye County
Post Office Box 153
Tonopah, NV 89049

Economic Development Department
City of Las Vegas
400 East Stewart Avenue
Las Vegas, NV 89101

Director of Community Planning
City of Boulder City
Post Office Box 367
Boulder City, NV 89005

Commission of European Communities
200 Rue de la Loi
B-1049 Brussels
BELGIUM

Technical Information Center
Roy F. Weston, Inc.
2301 Research Boulevard,
Third Floor
Rockville, MD 20850

R. Harig
Parsons, Brinkerhoff, Quade, &
Douglass, Inc.
1625 Van Ness Avenue
San Francisco, CA 94109-3678

Dr. M. M. Singh, President
Engineers International, Inc.
98 East Naperville Road
Westmont, IL 60559-1595

Dr. N. L. Carter, Director
Center for Tectonophysics
Texas A& M University
College Station, TX 77843

RE/SPEC, Inc. (2)
Post Office Box 725
Rapid City, SD 57701
Attention:
P. F. Gnirk
P. E. Senseny

RE/SPEC, Inc. (2)
Post Office Box 14984
Albuquerque, NM 87191
Attention:
S. W. Key
D. K. Parrish

R. Coppage, Senior Mining Engineer
Fenix & Scisson, Inc.
Post Office Box 498
Mercury, NV 89023

Christopher Barton
U. S. Geological Survey
Post Office Box 327
Mercury, NV 89023

Eugene P. Binnall
Field Systems Group
Building 50B/4235
Lawrence Berkeley Laboratory
University of California
Berkeley, CA 94720

J. D. Blacic
Los Alamos National Laboratory
Post Office Box 1663
Mail Stop J-980
Los Alamos, NM 87545

R. Newmark
Lawrence Livermore National Laboratory
Post Office Box 808
Mail Stop L-221
Livermore, CA 94550

T. H. Isaacs (RW-22)
Office of Geologic Repositories
U. S. Department of Energy
Forrestal Building
Washington, D. C. 20585

D. H. Alexander (RW-24)
Office of Geologic Repositories
U. S. Department of Energy
Forrestal Building
Washington, D. C. 20585

J. P. Knight (RW-23)
Office of Geologic Repositories
U. S. Department of Energy
Forrestal Building
Washington, D. C. 20585

A. Jelacic (RW-24)
Office of Geologic Repositories
U. S. Department of Energy
Forrestal Building
Washington, D. C. 20585

G. Parker (RW-25)
Office of Geologic Repositories
U. S. Department of Energy
Forrestal Building
Washington, D. C. 20585

J. R. Rollo
Deputy Assistant Director
for Engineering Geology
U. S. Geological Survey
106 National Center
12201 Sunrise Valley Drive
Reston, VA 22092

B. J. King, Librarian
Basalt Waste Isolation Project Library
Rockwell Hanford Operations
Post Office Box 800
Richland, WA 99352

C. M. St. John
J. F. T. Agapito Associates, Inc.
27520 Hawthorne Blvd., Suite 137
Rolling Hills Estates, CA 90274

Roger Hart
Itasca Consulting Group, Inc.
Post Office Box 14806
Minneapolis, MN 55414

D. Fenster
Roy F. Weston, Inc.
955 L'Enfant Plaza SW
Washington, DC 20024

C. Voss
Batelle
2030 M St. NW, Suite 800
Washington, DC 20036

E. Hardin
Science Applications International, Corp.
101 Convention Center Drive, Suite 409
Las Vegas, NV 89109

D. Eppler
Science Applications International, Corp.
101 Convention Center Drive, Suite 409
Las Vegas, NV 89109

J. D. Weeks
Box 1846
Geology Department
Brown University
Providence, RI 02912

T. E. Tullis
Box 1846
Geology Department
Brown University
Providence, RI 02912

A. L. Ruina
TAM
Thurston Hall
Cornell University
Ithaca, NY 14853

J. R. Rice
Division of Applied Science
Harvard University
Cambridge, MA 02138

J. D. Byerlee
MS 77
NCER
U. S. Geological Survey
345 Middlefield Rd.
Menlo Park, CA 94025

D. Lockner
MS 77
U. S. Geological Survey
345 Middlefield Rd.
Menlo Park, CA 94025

J. H. Dieterich
U. S. Geological Survey
345 Middlefield Rd.
Menlo Park, CA 94025

J. M. Logan
Center for Tectonophysics
Texas A & M University
College Station, TX 77843

E. C. Drumm
Department of Civil Engineering
110C Perkins Hall
The University of Tennessee
Knoxville, TN 37996-2010

1510	J. W. Nunziato	7417	F. L. McFarling
1520	D. J. McCloskey	8024	P. W. Dean
1521	R. D. Krieg		
1523	E. P. Chen		
1524	A. K. Miller		
1524	K. W. Schuler		
1530	L. W. Davison		
1534	J. R. Asay		
1540	W. C. Luth		
1541	H. C. Hardee		
1542	S. R. Brown		
1542	D. J. Holcomb		
1542	W. A. Olsson (20)		
1542	L. W. Teufel		
1542	W. R. Wawersik		
1542	D. H. Zeuch		
1543	T. M. Gerlach		
1550	R. C. Maydew		
3141	S. A. Landenberger (5)		
3151	W. L. Garner (3)		
3154-1	C. H. Dalin, for DOE/OSTI (28)		
6300	R. W. Lynch		
6310	T. O. Hunter		
6311	C. Mora (2)		
6311	T. O. Hunter (Acting)		
6311	V. Hinkel (2)		
6312	F. W. Bingham		
6312	B. S. Langkopf		
6313	T. E. Blejwas		
6313	R. E. Finley		
6313	F. B. Nimick (4)		
6313	R. H. Price		
6313	B. M. Schwartz for DRMS files 51/L02A1.A-02/24/84 and 51/L02A1.A-06/26/85 (2)		
6313	A. Stevens		
6313	R. M. Zimmerman		
6314	S. J. Bauer		
6314	L. S. Costin		
6314	B. L. Ehgartner		
6314	A. J. Mansure		
6314	J. R. Tillerson		
6315	S. Sinnock		
6332	WMT Library (20)		
6410	N. R. Ortiz		

